Advances in Optics and Photonics

Navigating optical skyrmions—from historical origins to applications: tutorial

Cheng Cheng,[1,5†] Lixi Rao,[1,5†] Junyi Ye,[1,5†] Xingqi Zhao,[1,5] Zhiyuan Che,[1,5,6] Wenzhe Liu,[1,2,4,5,7] Jiajun Wang,[1,4,5,8] and Lei Shi[1,2,3,4,5,*]

[1]State Key Laboratory of Surface Physics, Key Laboratory of Micro- and Nano-Photonic Structures (Ministry of Education) and Department of Physics, Fudan University, Shanghai 200433, China
[2]Institute for Nanoelectronic Devices and Quantum Computing, Fudan University, Shanghai 200438, China
[3]Collaborative Innovation Center of Advanced Microstructures, Nanjing University, Nanjing 210093, China
[4]Shanghai Research Center for Quantum Sciences, Shanghai 201315, China
[5]Shanghai Key Laboratory of Metasurfaces for Light Manipulation, Fudan University, Shanghai 200433, China
[6]chezy@fudan.edu.cn
[7]wzliu@fudan.edu.cn
[8]jiajunwang@fudan.edu.cn
[†]These authors contributed equally to this work.
*lshi@fudan.edu.cn

Received May 29, 2025; revised December 8, 2025; accepted December 23, 2025; published December 23, 2025

Optical skyrmions are topological structures formed by the distribution of light's vectorial properties, including polarization, spin, and electromagnetic fields. This tutorial provides a comprehensive overview of the theoretical foundations, configurations, generation mechanisms, and applications of optical skyrmions. Beginning with the historical development from Kelvin's vortex theory to Skyrme's soliton model, the article establishes the topological framework using homotopy groups to classify vortices, skyrmions, hopfions, and other related topological structures. The distinct types of optical skyrmions—such as Néel-type, Bloch-type, and high-order variants—are characterized using topological invariants like vorticity, polarity, and helicity. Connections between optical skyrmions and other topological entities are explored, showing how structures like hopfions and knots arise from field mappings between compactified manifolds. Experimental realizations through interference of evanescent fields, metasurfaces, spatial light modulators, and spatiotemporal modulation are described, along with methods for dynamic control and topological transitions. Applications in optical information processing, sensing, and quantum technologies are discussed, highlighting the robustness and subwavelength precision enabled by topological protection. Although prior reviews and tutorials exist, this tutorial is necessary because at this pivotal transition from fundamental research to applications, a comprehensive tutorial is significant for navigating new understanding and applications. This tutorial aims to equip readers with both foundational and practical knowledge, positioning optical skyrmions as versatile tools for advancing topological photonics and next-generation photonic technologies.

https://doi.org/10.1364/AOP.569106

Navigating optical skyrmions—from historical origins to applications: tutorial

Cheng Cheng, Lixi Rao, Junyi Ye, Xingqi Zhao, Zhiyuan Che, Wenzhe Liu, Jiajun Wang, and Lei Shi

1. INTRODUCTION

Optical skyrmions represent one of the most fascinating developments in topological photonics, offering a uniquely rich platform where quasiparticles, topology, and advanced electromagnetic field manipulation converge [1]. Their topological field configurations—initially conceived in high-energy physics as 3-dimensional (3D) structures and later realized as 2-dimensional (2D) counterparts also called "baby skyrmions" in condensed matter systems [2]—have now emerged as a vibrant frontier in optics and other wave systems.

The fundamental concept of a skyrmion dates back to Tony Skyrme's work in the 1960s [3,4], where he proposed a nonlinear field theory describing particles as topological solitons. Earlier conceptual roots can be found in Lord Kelvin's 1867 "vortex atom" hypothesis [5], which envisioned atoms as stable, knotted vortices in the ether—planting early seeds of topological thinking in physics. Skyrme's work gained recognition through Witten's investigations in quantum chromodynamics during the 1980s [6], establishing connections between topology and particle physics. The first experimental realizations came in 2009 when researchers observed skyrmion textures in magnetic materials [7], with the optical domain soon emerging as an ideal platform for exploring these topological structures [8,9].

Optical skyrmions are characterized by their topological charge, which quantifies how a normalized vector field wraps around a sphere in parameter space [10]. This topological foundation gives rise to multiple types of configurations—Néel-type, Bloch-type, anti-skyrmions, merons, and higher-order arrangements—each with distinct structural signatures. Unlike their magnetic counterparts, where the vector field represents spin textures in material systems, optical skyrmions can utilize various vectors as their building blocks. The vector field can be chosen to represent electromagnetic field vectors, polarization states, or spin angular momentum (SAM) [1], leading to diverse classes of optical skyrmions: field skyrmions [9,11,12], spin skyrmions [13,14], and Stokes skyrmions [15–17]. The significance of these structures extends well beyond fundamental physics—their topological protection provides inherent stability against perturbations, making them exceptionally robust information carriers [18], while their vectorial nature enables deep-subwavelength features that potentially overcome diffraction limits [11,13,19]. The rich variety in both configuration types and skyrmion classes offers extraordinary degrees of freedom for unprecedented opportunities for photonic technologies.

Recent years have witnessed remarkable advances in the generation [9], transport [15], manipulation [20], and application of optical skyrmions [21–24]. Sophisticated spatiotemporal modulation techniques now enable the creation of custom-designed skyrmion textures through interference, metasurfaces, spatial light modulators (SLMs), and integrated photonic structures [25,26]. The propagation of these topological entities through various optical media reveals unique transport behaviors that preserve

Table 1. Consolidated Text Box of Topological Structures and Configurations[a]

Terminology	Description
Vortex	A topological field where physical quantities wind around a central singularity in a 2D domain
Skyrmion	A topological field where normalized vectors sweep all possible orientations in a domain
3D skyrmion	A skyrmion configuration with 4D vectors distributed in a 3D domain
Baby skyrmion	A skyrmion configuration with 3D vectors distributed in a 2D domain (Throughout this tutorial, "skyrmion" refers to "baby skyrmion," unless specified otherwise)
Meron	A half-skyrmion configuration
Bimeron	A structure consisting of two coupled merons
Skyrmionium	A structure comprising a skyrmion surrounded by an anti-skyrmion
Bimeronium	A composite structure formed by two coupled bimerons with opposite topological charges
Skyrmion tube	A 3D extension of a 2D skyrmion along the third spatial dimension
Skyrmion bundle	A clustered arrangement of multiple skyrmion tubes
Skyrmion lattice	A periodic arrangement of skyrmions in 2D plane
Knot	A closed topological loop of field lines in 3D space
Link	A structure comprising multiple intertwined closed field lines
Hopfion	A linked structure with 3D vectors distributed in a 3D domain
Hopfion crystal	A periodic 3D lattice arrangement of hopfions
Monopole	A point-like topological defect
Toron	A 3D topological structure consisting of a point defect and an antidefect connected by a double-twist cylinder
Heliknoton	A hopfion-like structure combining helical background
Skyrmionic hopfion	A type of 3D skyrmion with vector configuration similar to hopfions

[a]Detailed description and physical pictures can be found in Section 3: Math and Topology.

their essential features. Dynamic control methods allow real-time manipulation of skyrmion properties in response to external stimuli [20]. These developments have opened pathways toward applications ranging from high-resolution sensing [21,22] and robust information transmission from classical to quantum [23,27].

Although prior reviews and tutorials exist that cover the systematic taxonomy and theoretical frameworks of optical skyrmions [1,28–33], the present tutorial is required because at this pivotal transition from fundamental research to practical applications, a comprehensive tutorial addressing unexplored historical, mathematical, and physical details is necessary for deepening the fundamental understanding and navigating new interdisciplinary applications. This tutorial uniquely addresses previously unexplored aspects across origins, generation mechanisms, propagation dynamics, manipulation strategies, and practical applications, providing the detailed guidance needed to propel optical skyrmions into their next phase of development. Aimed at a broad scientific audience, this tutorial serves as a navigational chart for the rapidly evolving landscape of optical skyrmions.

This tutorial provides a comprehensive introduction to optical skyrmions, covering their mathematical foundations, physical properties, experimental realization, and emerging applications. We begin by the rich historical development of skyrmions—from Lord Kelvin's vortex theory through Skyrme's groundbreaking work to the recent experimental advances in magnetic systems and various wave platforms. A dedicated section establishes the topological framework underlying skyrmions, emphasizing the connections between homotopy theory and optical field configurations. We then explore the various types of skyrmions and their classification based on vorticity, polarity, and helicity. Table 1 summarizes the terminology of topologies used in this tutorial. The tutorial proceeds to present mathematical derivations and physical techniques for generating optical skyrmions, highlighting the roles of spatiotemporal modulation, plasmonic structures, SLMs, and metasurfaces. We examine the propagation properties of optical skyrmions in free space and complex media, emphasizing their topological stability and nondiffracting characteristics. We discuss dynamic manipulation techniques that allow researchers to tailor skyrmions. Finally, we survey current and potential applications, from optical sensing and communication to quantum information processing.

Figure 1

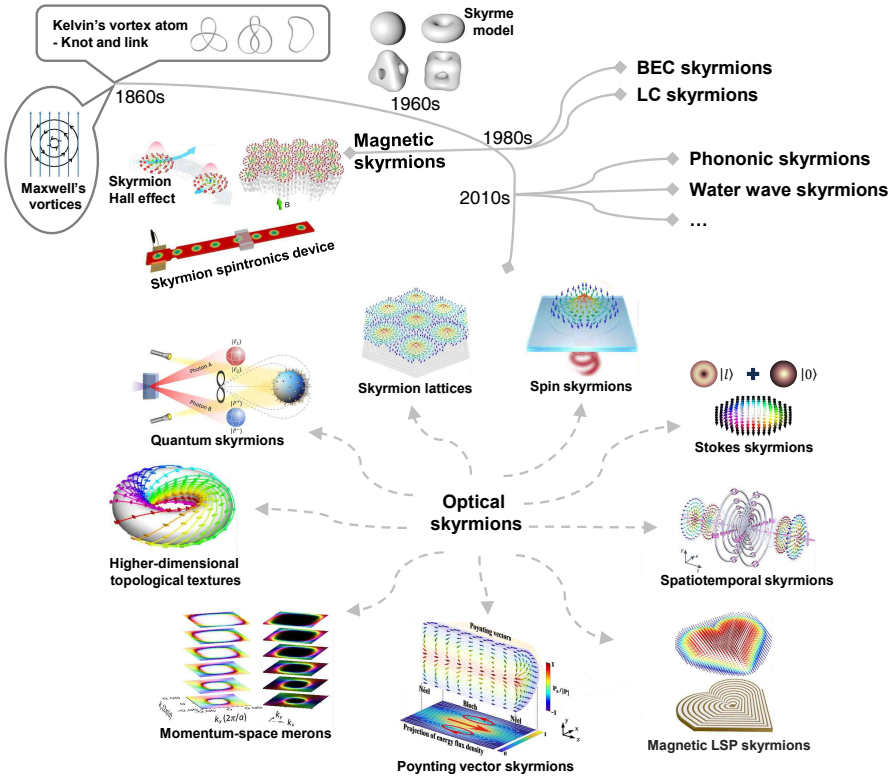

Navigating the skyrmion odyssey. Tracing the key milestones from the inception of Maxwell's and Kelvin's theoretical concepts, through the progress in nuclear and condensed matter physics, to the recent emergence of optical skyrmions, including field skyrmion lattices [9,11], spin skyrmions [13,34], Stokes skyrmions [15], spatiotemporal skyrmions [12], magnetic LSP skyrmions [35], Poynting vector skyrmions [36], momentum-space skyrmions [37], quantum skyrmions [23,27], and higher-dimensional topological textures [38]. Adapted from [12,35] under a Creative Commons license. Adapted from [27] under a Creative Commons license. Adapted from Shi *et al.* "Embarking on a skyrmion odyssey," Photon. Insights **3**, C02 (2024), Ref. [39], under a Creative Commons license. Adapted with permission from Wang *et al.*, Phys. Rev. Lett. **133**, 073802 (2024), Ref. [36]. Copyright 2024 by the American Physical Society. Adapted with permission from Rao *et al.*, Phys. Rev. Lett. **135**, 026203 (2025), Ref. [37]. Copyright 2025 by the American Physical Society.

Our goal is to equip readers with both the theoretical understanding and practical knowledge needed to engage with this rapidly evolving field. By bridging concepts from topological structures, wave-particle entities, and advanced light field engineering, this tutorial serves not only as an introduction for newcomers but also as a resource for researchers seeking to harness the unique properties of optical skyrmions for fundamental discoveries, technological innovations, and interdisciplinary applications.

2. HISTORY OF SKYRMIONS

The concept of skyrmions has evolved significantly since its theoretical inception in the 19th century [39]. As shown in Fig. 1, early contributions by James Clerk Maxwell and Lord Kelvin laid the foundation for the idea of topologies and the role of rotational fields in physical systems. This concept was later formalized by Tony Skyrme, who proposed topological solitons in meson fields to describe nucleons. Over the years, skyrmions have

transcended their original context in nuclear physics and have become a key subject of study in various areas of physics, such as magnetic systems, Bose–Einstein condensates (BECs), and liquid crystals (LCs). More recently, the study of skyrmions has expanded into diverse wave systems, including optics, acoustics, phononics, and hydrodynamic systems. This section delves into the history of skyrmions, from their early theoretical roots to their experimental realization in a wide range of systems, and discusses their diverse applications and future prospects in next-generation technologies.

2.1. Origin of Skyrmions

The conceptual seeds of skyrmions were sown long before Tony Skyrme's work, in the 19th-century debates over the fundamental nature of matter and electromagnetism. At the heart of these discussions were two towering figures: James Clerk Maxwell and Lord Kelvin (William Thomson). Their explorations of rotational fields and topological stability laid the groundwork for what would later become the skyrmion.

In his 1861 paper "On Physical Lines of Force" [40], Maxwell sought to explain electromagnetism through a mechanical model of the luminiferous ether—a hypothetical medium thought to permeate space. He envisioned magnetic fields as arrays of microscopic vortices, with their rotational motion representing magnetic flux, and introduced layers of spherical "idle wheels" between neighboring vortices to maintain compatibility of motion. These idle wheels played the role of charge carriers, transmitting stresses and giving rise to what we now call the displacement current. Maxwell's construction allowed induced currents and electromotive forces to be visualized as mechanical reactions between vortices and interposed particles, analogous to the pressures in a system of rotating gears. In his own words, the lines of force could be regarded as "lines of tension" sustained by the vortices, with conservation laws akin to those of fluid circulation. Although later freed from its ether background, this mechanical analogy captured two profound insights: first, that field phenomena could be represented by continuous structures endowed with rotational or topological stability; and second, that stability could emerge from conserved circulation in a medium, much as Helmholtz had shown for vortices in hydrodynamics. Maxwell's intuition that twisted or knotted configurations could persist against decay was prescient, resonating directly with the later understanding of skyrmions as stable, particle-like topological solitons in nonlinear field theories [41].

Inspired by Maxwell's work on rotational fields, Lord Kelvin significantly advanced the concept in his groundbreaking 1867 "Vortex Atom" hypothesis [5], which proposed that atoms were nothing but stable, knotted vortices swirling in the luminiferous ether. In this elegant model, different chemical elements corresponded to distinct knot topologies—the simplest unknot representing hydrogen, while more complex knots like trefoils or figure-eights might form heavier atoms. This revolutionary idea introduced two fundamental principles that would profoundly influence later physics: first, the notion of topological stability, where the mathematical properties of these knotted structures made them inherently resistant to unraveling; and second, the elegant explanation for the discreteness of matter, as the diversity of elements naturally emerged from the variety of possible knot configurations. Though ultimately superseded by quantum theory, Kelvin's visionary model planted the crucial seeds of topological thinking in physics, demonstrating how stable, particle-like entities could emerge purely from the twisted geometry of continuous fields—a conceptual breakthrough that would resurface a century later in Skyrme's work and modern skyrmion physics.

When Skyrme revisited the idea in the 1960s [41], he replaced Kelvin's ether with a quantum field theory framework, where nucleons emerged as topological twists in the pion field. Tony Skyrme proposed a nonlinear meson field theory [3,4], describing

Figure 2

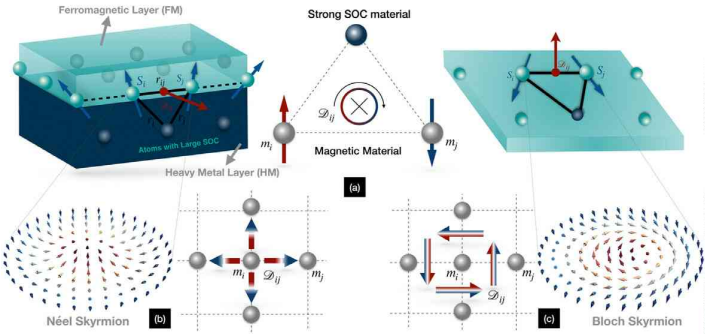

Mechanisms of DMI and resulting skyrmion spin textures [49]. (a) Origin of the DMI from broken inversion symmetry. (b) Interfacial DMI at a magnetic/heavy-metal interface. This interaction stabilizes a Néel skyrmion where spins point radially. (c) Bulk DMI in a noncentrosymmetric material. This interaction stabilizes a Bloch skyrmion where spins rotate in a helical fashion. Reprinted with permission from Mishra *et al.*, Appl. Phys. Rev. **12**, 011315 (2025) [49]. Copyright 2025, AIP Publishing LLC.

particles as field solutions of topological solitons and applying the topological properties of the meson field to interpret the baryon number as a field topological number. Unlike Kelvin's speculative vortices, the nonlinear field of Skyrme' s model ensures stability through both topology and physical interactions. Although Skyrme's theory did not receive widespread attention at the time, it paved the way for the later discovery of skyrmions in condensed matter systems and wave systems.

In the 1980s, the theory of Skyrme was re-examined, especially in the researches of Edward Witten [6] on quantum chromodynamics. He demonstrated that the Skyrme model can be applied as an effective theory to describe baryons and to relate their topological properties to real particle physics. This theory has significant implications in high-energy physics and has provided a methodological basis for the study of topological solitons in condensed matter physics.

2.2. History of Magnetic Skyrmions and Skyrmions in Other Condensed Matter Systems

Magnetic skyrmions appear as rotational arrangements of spins in magnetic materials [42,43]. In 1975, Belavin and Polyakov theoretically demonstrated the existence of magnetic skyrmions in a 2D classical Heisenberg ferromagnet [44]. Theoretical investigations into topological magnetic structures gained momentum in the late 1980s, 1990s, and early 2000s, with a significant advancement made by Bogdanov and colleagues [45,46]. They demonstrated that chiral magnets with broken inversion symmetry could support stable, localized topological spin configurations (skyrmions), characterized by an integer winding number that ensures stability under continuous transformations. The stability of magnetic skyrmions stems from the nonlinear field theory solution of skyrmions, typically relying on the Dzyaloshinskii–Moriya interaction (DMI) [47–51], which arises from spin–orbit coupling in systems without spatial inversion symmetry and introduces a tendency for spiral spin arrangements by combining with ferromagnetic exchange coupling, as shown in Fig. 2. In 1993, Sondhi *et al.* theoretically predicted the existence of skyrmions in the quantum Hall state of a 2D electron gas [52]. In 2006, Roessler *et al.* theoretically demonstrated for the first time that in magnetic metals (such as MnSi) lacking spatial inversion symmetry, stable skyrmion ground states can form spontaneously without relying on external magnetic fields or defects [46].

The experimental realization of magnetic skyrmions began in 2009 when neutron scattering studies on MnSi revealed spin textures in its "A-phase" [7,53], later confirmed in 2010 via direct imaging of skyrmion lattices in FeGe [54]. Subsequent research expanded skyrmion-host materials beyond bulk B20 compounds to ultra-thin films (e.g., Pt/Co/Ir trilayers), achieving room-temperature stability by 2016 through interfacial DMIs [55]. The topological Hall effect [56], a hallmark of skyrmion systems, arises from the real-space Berry phase acquired by electrons traversing the non-trivial spin texture, providing a direct electrical probe for skyrmion detection and dynamics. Skyrmions were found to be driven by ultralow current densities ($10^6 \mathrm{A/m}^2$) [57,58], making them promising for energy-efficient spintronics. The discovery of Néel-type skyrmions and anti-skyrmions in materials like Mn-Pt-Sn [59] further revealed the influence of crystal symmetry on skyrmion morphology, broadening opportunities for engineered spin textures [60].

Recent years have witnessed explorations of 3D skyrmion tubes [61], biskyrmions [62,63], and hybrid structures [64,65], as well as skyrmions in van der Waals materials [66–68] and synthetic antiferromagnets [69–73]. Advances in imaging techniques, such as spin-polarized scanning tunneling microscopy [74], have enabled atomic-scale characterization. Meanwhile, concepts like skyrmion-based neuromorphic computing [75] and probabilistic computing [76] underscore their versatility beyond conventional electronics.

Fascinating manifestations of skyrmions have been discovered not only in magnetic systems but also in other condensed matter systems, including BECs and LCs. In BECs, particularly in spinor condensates, skyrmions emerge as stable, topologically protected excitations, offering a unique platform for investigating spin textures and quantum coherence [77]. Researchers have explored the creation and manipulation of skyrmions in BECs, including their realization in spin-2 and spin-1 condensates, as well as the emergence of quantum skyrmion liquids in low-dimensional systems [78]. These discoveries have opened up new avenues in the study of topological phases and quantum dynamics [79]. Similarly, in LC systems, skyrmions exhibit intriguing behavior, such as the formation of chiral textures and the possibility of their controlled manipulation using external fields [80]. The study of skyrmions in these soft matter systems has led to insights into their potential applications in information storage, as well as their role in understanding the topological properties of LC phases [81].

All previously discussed are Abelian skyrmions that obey commutative symmetry groups, and their interactions do not depend on the order in which they are manipulated. In contrast, non-Abelian skyrmions arise in systems governed by non-commutative Lie groups such as $SU(2)$ or $SO(3)$, where their interactions depend on the sequence of operations, leading to non-trivial braiding and complex dynamical behavior [82]. Owing to their non-commutative nature, these skyrmions possess topologically protected states capable of encoding quantum information in a manner robust against local perturbations. Theoretical studies further connect non-Abelian skyrmions to Chern band models, where quasiparticles exhibit exotic braiding statistics and topological protection, offering a promising framework for applications [60,75,82–84].

Together, these systems highlight the versatility of skyrmions and their broad relevance to both fundamental and applied physics in condensed matter research.

2.3. Skyrmions in Optics and Other Wave Systems

While magnetic skyrmions have been extensively studied in condensed matter physics, their counterparts in optics, acoustics, and hydrodynamics have recently gained attention

Figure 3

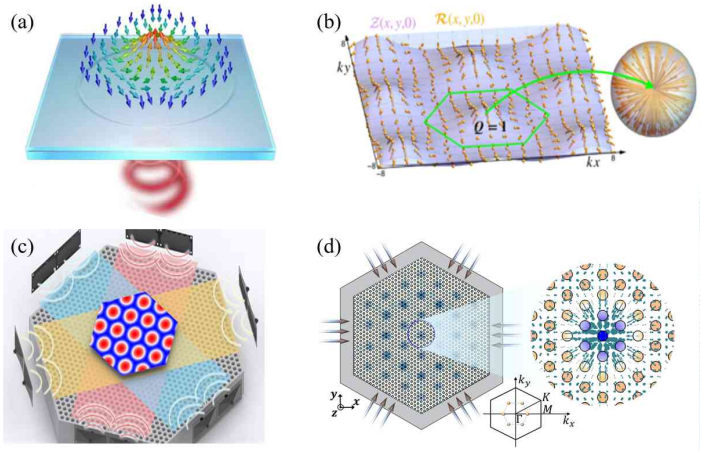

Skyrmion lattices generated from the interference of waves in different wave systems. (a) Optical skyrmion [9,11,39]. (b) Surface Water Wave Skyrmion [85]. (c) Acoustic Skyrmion [86]. (d) Phononic skyrmion (elastic wave skyrmion) [87]. (a) Reprinted from Shi *et al.* "Embarking on a skyrmion odyssey," Photon. Insights **3**, C02 (2024), Ref. [39], under a Creative Commons license. (b) Reprinted with permission from Smirnova *et al.*, Phys. Rev. Lett. **132**, 054003 (2024), Ref. [85]. Copyright 2024 by the American Physical Society. (c) Reprinted with permission from Ge *et al.*, Phys. Rev. Lett. **127**, 144502 (2021), Ref. [86]. Copyright 2021 by the American Physical Society. (d) Reprinted from [87] under a Creative Commons license.

as unique topological wave structures [9,85–87]. From optical skyrmions in laser fields to stable acoustic vortices in phononic crystals and even hydrodynamic skyrmions on water surfaces, these structures share a common thread: topological protection enabling wave manipulation. This section explores the historical evolution and key discoveries of non-magnetic skyrmions, highlighting their emergence as transformative tools in wave engineering and applied physics.

The story of optical skyrmions is a significant chapter in the history of skyrmions, beginning with their theoretical conception and culminating in groundbreaking experimental realizations. Optical skyrmions are topological structures formed from light's vectorial properties—such as polarization, spin, and phase—rather than electron spins. The journey to their discovery accelerated in the 2010s, as advances in structured light [88] and nanophotonics provided the tools to engineer complex wavefronts with precise topological characteristics. In 2010, the concept of the full Poincaré beam was proposed [8], but its connection to skyrmions remained unrecognized. It was not until 2018, with the experimental demonstration of optical skyrmion lattices using evanescent electromagnetic fields in plasmonic systems [9] [Fig. 3(a)], that the link between structured light and skyrmionic topology began to emerge. This breakthrough revealed that these exotic structures could be realized through interferences, relying instead on carefully designed wave interference and global topological constraints.

Further progress quickly expanded the family of optical skyrmions, introducing 2D baby skyrmions, merons, and even 3D hopfions—particle-like topological states created by superimposing vectorial Laguerre–Gaussian (LG) beams. These structures exhibit deep-subwavelength features or femtosecond-scale dynamics, enabling new ways to manipulate light at scales beyond the diffraction limit. A key distinction emerged between optical skyrmions and singular vortices: while vortices require phase singularities, skyrmions could be nonsingular, making them more robust for applications in

imaging, sensing, and optical communications. Recent studies have also explored their topological robustness, linking it to spin–orbit coupling and the non-separability of spatial and polarization degrees of freedom.

Today, optical skyrmions represent a vibrant research frontier [39], with open questions about their stability under perturbations, their behavior in nonlinear regimes, and their potential for high-dimensional generalizations, such as hopfion links. Their ability to encode information in topologically protected states makes them promising candidates for next-generation photonic devices, from ultra-compact optical processors to fault-tolerant data transmission systems. As experimental techniques grow more sophisticated, the future of optical skyrmions promises not only deeper fundamental insights but also transformative technological applications, solidifying their place at the cutting edge of photonics.

Wave structures with topological properties, including vortices, skyrmions, and polarized Möbius strips, were generated on the water surface [85] [Fig. 3(b)]. Skyrmions in water wave are topological wave structures that exhibit remarkable dynamic properties in water waves and can manipulate floating tiny particles [89], providing new perspectives and applications for the topological properties of water waves and particle manipulation, especially in the fields of hydrodynamics and microfluidics.

In the field of acoustics, significant emphasis is placed on the wave propagation of acoustic skyrmions in medium, which are capable of forming self-maintaining structures in acoustic waveguides due to their topological stability [86,90] [Fig. 3(c)]. These skyrmions exhibit strong applicational potential across a wide range of fields, including phononic elements, signal processing, and remote sensing technology. Phononic crystal systems, in particular, offer powerful capabilities for manipulating the propagation of acoustic waves and phonons [87] [Fig. 3(d)]. Within such systems, the topological stability of skyrmions can facilitate waveguide design, energy transfer, and innovative applications in phononic quantum computation. Leveraging these properties enables the development of devices with high energy transmission efficiency and ultralow loss.

The exploration of skyrmions beyond condensed matter systems has unveiled a rich landscape of topological wave phenomena, reshaping our understanding of energy and information transport across multiple domains. From early theoretical predictions to experimental realizations in acoustic, optical, and fluid systems, these discoveries underscore the universality of skyrmion physics. As research advances, the interplay between theory and applications promises breakthroughs in quantum phononics, optical computing, and microfluidics, cementing non-magnetic skyrmions as pivotal elements in next-generation wave technologies. Their history, though shorter than that of magnetic skyrmions, is a testament to the enduring relevance of topological concepts in modern science.

3. MATH AND TOPOLOGY

Having journeyed through the historical development of skyrmions in the previous section, we have witnessed how the visionary topological ideas of pioneers such as James Clerk Maxwell and Lord Kelvin (William Thomson) planted the intellectual seeds that would later flourish under the ingenious insights of Tony Skyrme. These conceptual beginnings eventually burgeoned into a vibrant and rapidly evolving domain within modern physics. Although the existing tutorial and other reviews have offered excellent and intuitive physical explanations of skyrmions and related topological textures and explained the basic properties of homotopy groups [1,28–33], these papers omit many of the mathematical details due to their differing focus and scope. In this section, we turn our attention to the detailed role that mathematical concepts and

topology plays in structuring the entire theoretical framework of skyrmionic systems. We will explore how mathematical concepts not only provide the foundational language but also orchestrate the rich connections between these exotic structures. Although only a small part of the vast mathematical toolbox, this framework has rapidly ascended to the forefront of physical research. We believe that this structured, concept-driven section will not only benefit beginners but also inspire further research into the mathematical foundations of topological phenomena, promoting cross-disciplinary collaboration between mathematics and physics. Now, let us embark on this exciting narrative, starting from fundamental mathematical notions and gradually unfolding the grand performance of skyrmionic topology.

3.1. General Skyrmionic Topology

In this subsection, skyrmionic topology, the fundamental topological theory underlying skyrmion-like quasiparticles, is systematically constructed, which transforms physical fields into a rich landscape of topological structures. We begin by introducing basic mathematical notions and then illustrate the core tool of this framework: the homotopy groups of spheres. With this elegant mathematical tool, we proceed to carve intricate topological structures into physical field configurations. Finally, we follow the path pioneered by Tony Skyrme and trace how physicists have masterfully incorporated these exquisite mathematical formations into tangible physical systems. Here, let the dance of topology, guiding us through the labyrinth where mathematics and physics intertwine, commence.

3.1.1. Basic Concepts of Skyrmionic Topology

Topology describes the properties of an object that remain unchanged under continuous deformations [91,92]. To discuss skyrmionic topology [10], several basic mathematical concepts have to be clarified, including manifolds, compactness, topological structures, and topological invariants.

Manifolds represent continuous geometric structures with flexibility, generalizing geometric structures such as curves and surfaces in mathematics [93]. Manifolds are characterized by their local Euclidean properties while potentially exhibiting global curvature. For example, a Euclidean space constitutes the simplest flat manifold without curvature. More complex examples of manifolds including spheres, tori, and Möbius strips are geometric structures possessing curvature. Besides, a crucial property of manifolds is their flexibility. Unlike rigid structures, manifolds can undergo continuous deformations while preserving their topological characteristics. This property makes them ideal models for studying physical systems under local perturbations. In this review, we focus primarily on the manifold of trivial spheres S^i, such as the 1-dimensional (1D) circle S^1, the 2D sphere S^2, and the 3D hypersphere S^3.

In physical systems, the manifold cannot be simply understood as the space we actually live in. A manifold can be a parameter space. For a physical system, the physical quantities are distributed in a space. Two manifolds of sphere can be distilled from topological physics systems [10]. First, the manifold of physical quantities. The physical quantities can be scalars or vectors. The scalars in skyrmionic topology usually exhibit periodic nature. For example, phase of electric fields is periodic, whose values can be expressed from 0 to 2π, where 0 and 2π are equivalent. This intrinsic characteristic can be represented naturally through angles spanning from 0 to 2π, which corresponds to every point on a circle in polar coordinates, thereby forming a circle. For vectors, we only care about the direction of the vectors. The vectors we mentioned in this review are normalized vectors, disregarding the length of vectors. In polar coordinates, these normalized $(j+1)$-dimensional physical vectors are determined by j angular degrees

Figure 4

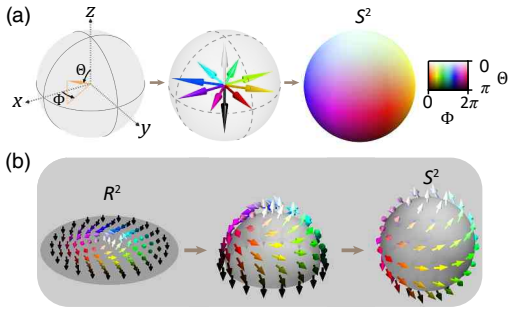

Schematic of two manifolds in a normalized-3D-vector field. (a) The manifolds of physical quantities. Normalized 3D vectors of physical quantities possess two angular degrees of freedom, the azimuthal angle Φ and the polar angle Θ, correspond one-to-one with the two angular coordinates of a sphere S^2. Thus, normalized 3D vectors with all orientations can form a S^2. The spheres in the middle and right panels rotate 90° counterclockwise around the z-axis compared to the left panel. (b) The manifolds of the spatial distributions. The spatial distributions R^2 of these vectors can also be compactified into another S^2. From left to right is the process of compactification. Here, the color bars in (a) and (b) are consistent, where the brightness represents polar angle of the vectors, and the hue represents the azimuthal angle.

of freedom. These j angular degrees of freedom correspond one-to-one with the j angular coordinates of a sphere S^j. Therefore, these normalized $(j+1)$-dimensional vectors can be mapped onto spherical manifolds S^j, as exemplified by the Poincaré sphere for normalized Stokes vectors, the Bloch sphere for quantum states, and circles for normalized 2D vectors. Figure 4(a) illustrates an example in which normalized 3D vectors with all directions form a S^2. Second, the manifold of spatial distributions. Physical quantities distributed in i-dimensional Euclidean space R^i can be compactified into i-spheres S^i under specific conditions. Then, the physical quantities are distributed in S^i. Figure 4(b) illustrates the compactification process for a 2D baby skyrmion, in which the spatial distribution of normalized 3D vectors in R^2 is compactified to S^2, analogous to curling a flat disk of clay inward and gradually shrinking its boundary to a point. For instance, the spatial distribution can be a polarization field, where the normalized Stokes vectors describing the polarization states form a manifold S^2 (the Poincaré sphere) in an abstract Stokes parameter space, and the spatial distribution of these Stokes vectors is another manifold S^2. In this case, the first S^2 in Fig. 4(a) represents the Poincaré sphere, and the second S^2 in Fig. 4(b) denotes sphere of the Stokes vector distribution.

Note that, compactification from R^2 to S^2 in Fig. 4(b) is conditional, and this condition is compactness [94,95]. The mathematical definition of compactness is rigorous and involves specific topological criteria. Here, we do not explain compactness in detail, as in this review we are only concerned with the compactness of the spheres and related spatial distributions. Spheres are naturally compact. Let us try to understand what compactness of the spheres means in graphic terms: no matter how we move on the surface of S^i, we cannot find its boundary. The compactness of the spatial distributions demands strict boundary conditions, typically realized in physical systems through periodic boundaries or bounded, closed domains [9]. The boundary here are composed of identical scalars or vectors. Conversely, if the boundary of physical systems cannot be well-defined, the compactness of spatial distribution is poor [95]. The compactification typically involves stereographic projection and its continuous deformations, as depicted in Fig. 4(b).

After compacting the distribution space, we can describe the topological properties of two manifolds of spheres in the physical system. These two manifolds are usually different. For the sphere of physical quantities, we can see from its formation process that the coordinates of the sphere and the physical quantity are equivalent. For example, the value of phase is equal to the angle of circle, and the vector from the center of the sphere to the surface of the sphere is the same as the physical vector. For the sphere of spatial distribution, the coordinates of the sphere and the physical quantities are correspondingly related instead of equivalent. While the two manifolds are different, a mapping can be harnessed to describe the relationship between these two manifolds. This mapping can be understood as a wrapping process. In detail, the manifold of spatial distribution typically encompasses some continuously varying physical quantities. For every physical quantity in the spatial distribution, we can map it onto a corresponding point of the sphere of physical quantities. These points can form a certain area of the manifold of physical quantities as if they wrap this area.

Non-trivial mappings can be constructed where the manifold of spatial distributions wraps around the full manifold of physical quantities with an integer of times [10]. Topological structures emerge in these non-trivial mappings, where the integer is the topological charge. The topological structures with robust topological charges, preserved under continuous deformations, constitute a topological invariant. The manifold of topological structures is not limited to S^2. Low-dimensional circles and high-dimensional hyperspheres can also form more non-trivial topological structures [10]. The mathematical framework for analyzing the topological invariants of skyrmions and related topological structures is provided by the homotopy groups of spheres, which we will explore in subsequent sections.

3.1.2. Homotopy Groups of Spheres

The homotopy groups of spheres $\pi_i(S^j)$ describe the mapping between the two spheres, mathematically expressed as [96–99]:

$$f : S^i \to S^j.$$

These groups are fundamental in studying singularities and topological structures, such as vortices, skyrmions, and hopfions. Through the study of homotopy groups of spheres, we can classify different topological structures that are robust under continuous transformations.

A fundamental example is the first homotopy group $\pi_1(S^1) = \mathbb{Z}$. It characterizes how a circle winds another, as illustrated in Fig. 5(a). Here, wound circle appears in gray. The winding circles are visualized as colored spiral loops with n chromatic cycles, revealing distinct mapping relationships through varied color distributions. The integer $n \in \mathbb{Z}$ represents the winding number, indicating the number of times the winding circle winds around the wound circle, where the sign indicates the direction. This integer is used to classify the equivalence classes of $\pi_1(S^1) = \mathbb{Z}$. In detail, while different mappings may exist, mappings with the same winding number n belong to the same equivalence class $\pi_1(S^1) = n$ within $\pi_1(S^1) = \mathbb{Z}$. The group operation of $\pi_1(S^1)$ is analogous to the addition, as shown in the bottom panel of Fig. 5(a): concatenating circles with winding numbers m and n produces a circle with winding number $m + n$, which establishes the Abelian nature of these homotopy groups. This group is fundamental for understanding vortices, where different winding numbers correspond to different topological configurations. The group $\pi_1(S^1) = \mathbb{Z}$ generalizes to finite dimensional analogs $\pi_i(S^i) = \mathbb{Z}$, where the homotopy group $\pi_i(S^i)$ classifies maps from an i-sphere S^i to another i-sphere S^i. For example, $\pi_2(S^2)$ classifies mappings of 2-spheres S^2, as presented in Fig. 5(b), indicating how many times the sphere S^2

Figure 5

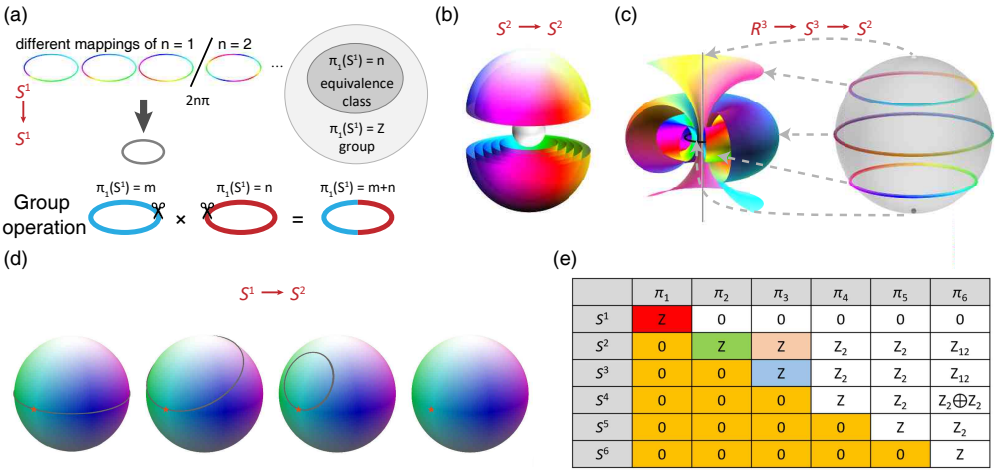

	π_1	π_2	π_3	π_4	π_5	π_6
S^1	Z	0	0	0	0	0
S^2	0	Z	Z	Z_2	Z_2	Z_{12}
S^3	0	0	Z	Z_2	Z_2	Z_{12}
S^4	0	0	0	Z	Z_2	$Z_2 \oplus Z_2$
S^5	0	0	0	0	Z	Z_2
S^6	0	0	0	0	0	Z

Homotopy groups of spheres and their geometrical representations. (a) Visualization of $\pi_1(S^1) = \mathbb{Z}$ and its group operation. Distinct mappings $\pi_i(S^i) = n$ correspond to different elements in the equivalence class of the homotopy group, with group operations analogous to addition. (b) Schematic of $\pi_2(S^2) = \mathbb{Z}$, demonstrating integer-valued wrapping of one sphere around another. (c) Schematic of $\pi_3(S^2) = \mathbb{Z}$. The projection of a single latitude of the S^2 into 3D space R^3 (here R^3 can be compactified into S^3), resulting in a toroidal twisted structure. The north pole manifests as a central axial line, while the south pole corresponds to an internal circle within the 3D configuration. (d) Schematic of $\pi_1(S^2) = 0$. A circle on S^2 can be continuously deformed to a point without wrapping, yielding a trivial mapping and establishing the general case $\pi_i(S^j) = 0$ for $i < j$. (e) Tabulation of $\pi_i(S^j)$ relationships $(i, j = 1, 2, 3, 4, 5, 6)$.

wraps around another sphere S^2. This can be analogized in the same way to higher dimensions. The group operation of these groups is similar to the first homotopy group $\pi_1(S^1) = \mathbb{Z}$, analogous to addition. In the context of skyrmions, the homotopy group $\pi_3(S^3)$ was initially employed in high-energy physics to classify 3D skyrmion configurations according to their wrapping numbers. This approach was later extended to $\pi_2(S^2)$ to describe baby skyrmions in other physical systems.

For the cases where $i \neq j$ in $\pi_i(S^j)$, they can present intriguing mathematical structures. When $i > j$, seemingly counterintuitive mappings from higher to lower dimensions become possible. In particular, $\pi_3(S^2)$ exhibits non-trivial structure through the Hopf fibration [100–102], where S^3 decomposes into S^1 fibers over S^2. In other words, every point on S^2 is a fiber circle in S^3, so S^3 is reduced in dimension to S^2. Thus, it ultimately manifests as a mapping between two 2-spheres. This fibration represents a form of dimensional reduction, projecting circles on spheres to nested tori in a 3D real space (R^3), as depicted in Fig. 5(c). Here S^3 is difficult to be illustrated comprehensively, so we use R^3 in Fig. 5(c) which can be compactified into S^3. This group $\pi_3(S^2)$ describes hopfion. In the next subsection, we will discuss this group $\pi_3(S^2)$ through a more specific generation process of hopfion. Conversely, when $i < j$, these groups are trivial, as lower-dimensional spheres can be continuously contracted to a point on higher-dimensional spheres through null-homotopic maps [see Fig. 5(d) as an example]. The classification of some homotopy groups of spheres is summarized in Fig. 5(e). The cases of other homotopy groups are therefore not discussed in detail. Nevertheless, it should not be interpreted as a lack of their significance. On the contrary, such groups may offer pathways for realizing higher-dimensional topological structures, potentially

enabling novel vector field or advanced topological structures in future studies [103]. Some significant studies have begun to unveil the veil on higher-dimensional topology through quantum methods and other advanced techniques [104,105].

These homotopy groups form the mathematical foundation for understanding various topological phenomena in field theories, condensed matter physics, and optics, providing a rigorous framework for analyzing topological defects and textures. The classification of stable topological structures through homotopy groups enables systematic study of vortices, skyrmions, hopfions, and related topological structure in physical systems.

3.1.3. Weaving the Topological Texture with Homotopy Groups

Skyrmions, vortices, hopfions, and related topological structure in physical field are classified as topological texture [28]. Topological textures refer to topological structures within a physical field characterized by a specific spatial arrangement of physical quantities. Based on the homotopy groups of spheres $\pi_i(S^j)$, various skyrmionic textures including skyrmions, vortices, hopfions, and skyrmionic hopfions can be weaved from a topological perspective, when physical quantities [j-dimensional scalars (for scalars, $j = 1$) or normalized (j+1)-dimensional vectors] are defined in a i-dimensional distribution space [2,10]. Then, we can observe that these skyrmionic textures exhibit profound connections to a part of the topological vision of Lord Kelvin, knots and links. It echoes the early conceptualizations of fields and elementary particles by these pioneers, which laid the imaginative groundwork for what would later emerge as the skyrmion in physical theory. It is significant to emphasize, however, that the homotopy groups describing knots and links such as $\pi_1(S^3/K)$, are fundamentally distinct from those classifying skyrmions.

The first homotopy groups $\pi_1(S^1) = \mathbb{Z}$ correspond to vortex configurations. Vortices are topological textures emerging as normalized-2D-vector field or a scalar field. Figure 6(a) illustrates examples of both scalar vortex and vector vortex. Although the vortices are distributed in a 2D plane, their topological properties are always determined by a closed circle around the center and are therefore considered to be 1D topology.

For a normalized-2D-vector field, each vector at a given point can be mapped to a specific position on the circle S^1. As one travels a closed circle in the distribution space, the corresponding mapped points on S^1 form a curve. The number of times this curve wraps around S^1 is the winding number of the field configuration. This winding number is a topological invariant that characterizes the vortex structure. Mathematically, it is expressed as [106]:

$$w = \frac{1}{2\pi} \oint \nabla\theta \cdot \mathrm{d}\boldsymbol{l}, \tag{1}$$

where the integral is taken along the closed circle in the distribution space, and θ is the angle parameterizing the position on S^1, which is the only parameter to describe the normalized 2D vector. Most of the winding numbers are integers, reflecting the discrete nature of the mapping, as the circle must wrap around S^1 an integer number of times. This topological invariance implies that the winding number cannot change under continuous deformations of the field, provided the singularity remains. This makes $\pi_1(S^1) = \mathbb{Z}$ a natural framework for classifying vortex configurations.

For scalar fields, such as the phase of a wavefunction or a light field, the phase angle $\theta(r)$ at each point also directly maps to a position on the circle S^1. Around a singularity, where the phase becomes undefined, the mapping from the physical distribution space to S^1 forms a closed circle. This circle wraps around the singularity in a manner analogous to the vector field case. The number of times it wraps around S^1 defines the winding number of the phase vortex. The winding number of this mapping defines the phase

Figure 6

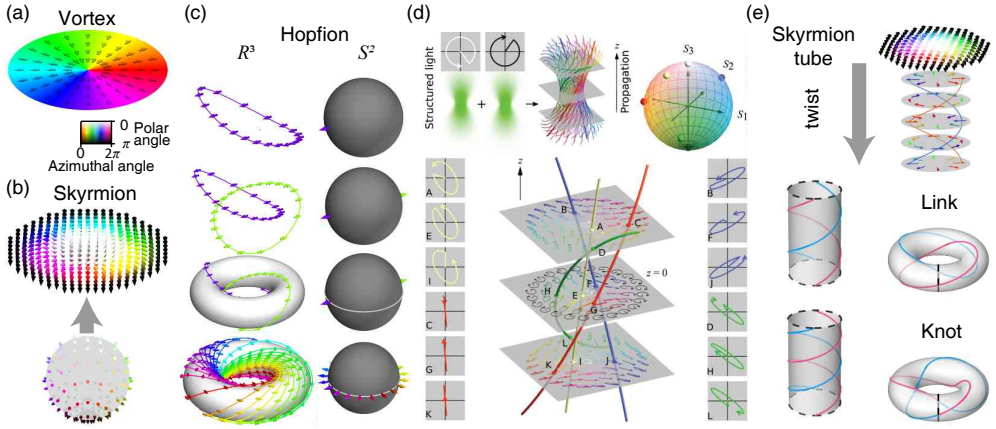

Schematic of several topological textures in physical systems. Schematic of (a) vortices, (b) skyrmions, (c) hopfions, (d) skyrmionic hopfion [38], and (e) knot and link. Conceptualizing an $(n+1)$-dimensional unit vector as a point on an n-dimensional sphere, vortices, skyrmions, and hopfions can be constructed to describe mappings between normalized vector fields and m-dimensional domains. These mappings, characterized by equivalence classes within homotopy groups of spheres $\pi_i(S^j) = Q$, inherently carry a topological charge Q that quantifies their fundamental geometric and topological properties. Link structures exist in hopfions. These link structures and related knot structures (the figure of knot formed by two lines with different colors is just a schematic diagram of the formation. The actual knot should be formed by the same vectors or singularities) can be formed by twisting skyrmion tubes composed of continuous multiple layers of skyrmions. (d) Reprinted from [38] under a Creative Commons license.

vortex, which is topologically equivalent to the vortex structures in normalized 2D-vector fields. This unified perspective, grounded in the topology of $\pi_1(S^1)$, provides a powerful framework for understanding and classifying vortex phenomena across diverse physical systems. Although both types of vortex fields are topologically described by the same homotopy group, they exhibit fundamentally distinct behaviors under symmetry operations. Vector vortices, being vector fields, undergo a change in the direction of their constituent vectors when subjected to symmetry transformations such as mirror reflection. In contrast, scalar remain invariant under symmetry operations in a scalar vortex. A well-known example in optics is the comparison between optical vortex beams and cylindrical vector beams, which we will explore in detail in later sections.

Higher-dimensional topological textures can also be characterized by homotopy groups. For example, both $\pi_3(S^3) = \mathbb{Z}$ and $\pi_2(S^2) = \mathbb{Z}$ characterize skyrmions. In fact, the earliest skyrmion was constructed based on $\pi_3(S^3) = \mathbb{Z}$ [3,4]. Here, we focus on introducing 2D baby skyrmions due to their prominent role in optical research and their particular suitability for visual interpretation. As shown in Fig. 6(b), skyrmions manifest as normalized-3D-vector fields distributed within 2D domains. All normalized 3D vectors form a manifold of S^2, which is wrapped by another manifold of S^2 formed by normalized-3D-vector distributions. This framework also encompasses other 2D skyrmion-like topological textures, including skyrmioniums, merons, bimerons, and bimeroniums. Their wrapping number, skyrmion number, is mathematically expressed as [107]:

$$N_{sk} = \frac{1}{4\pi} \iint \hat{\mathbf{n}} \cdot \left(\frac{\partial \hat{\mathbf{n}}}{\partial x} \times \frac{\partial \hat{\mathbf{n}}}{\partial y} \right) \mathrm{d}x\mathrm{d}y, \tag{2}$$

where $\hat{\mathbf{n}}$ represents the normalized 3D vector, and x and y represent space coordinates. Compared with the normalized 2D vector, the normalized 3D vector $\hat{\mathbf{n}}$ points to the 4π solid angle of the sphere S^2 instead of the 2π plane angle of the circle S^1. Significantly, skyrmion-like topological textures preserve their skyrmion number under continuous deformation, ensuring their stability across various physical systems.

The case of normalized-3D-vector fields distributed in 3D domains exhibits particularly intriguing features. When such a field occupies Euclidean space R^3, the corresponding mappings classified by the homotopy group $\pi_3(S^2) = \mathbb{Z}$ give rise to hopfions [108]. Here, we introduce the mathematical framework of hopfions in detail. Analogous to compactification of baby skyrmions from R^2 to S^2, we compact R^3 to S^3 via techniques such as stereographic projection at first. Then, the mathematical structure becomes maps from S^3 to S^2. This mathematical map can be formulated via the Hopf map: $\hat{\mathbf{n}} = \langle\zeta|\sigma|\zeta\rangle$, where $\hat{\mathbf{n}} = (n_1, n_2, n_3)$ is a normalized 3D vector $(n_1^2 + n_2^2 + n_3^2 = 1)$, σ represents Pauli matrices, and $|\zeta\rangle$ denotes 4D vectors $(X_4 + \mathrm{i}X_3, X_1 + \mathrm{i}X_2)^T$ of a hypersphere $S^3 (X_1^2 + X_2^2 + X_3^2 + X_4^2 = 1)$. The Hopf map fundamentally describes a mapping from the domain, hypersphere S^3 of spatial distribution manifolds, to the codomain, sphere S^2 of physical quantity manifolds, establishing a topological wrapping in which the spatial hypersphere S^3 wraps the physical quantity sphere S^2 [109]. In other words, the Hopf map from S^3 to S^2 serves as the foundational mechanism, determining the basic configuration of hopfions and their topological numbers in R^3.

Figure 6(c) demonstrates a fundamental hopfion configuration and its formation process. The point in S^2 corresponds to a vector, forming a fiber circle in R^3. Then, fiber circles corresponding to two different points at the same latitude are entangled with each other to form a link structure. All the points on this latitude of S^2 eventually form a toroidal surface. In other words, this toroidal surface is formed by vectors $\hat{n}$ with identical n_3 in 3D space R^3. Figure 6(c) only shows the toroidal surface corresponding to one latitude, i.e., one n_3. The toroidal surfaces exhibit a relationship with n_3. The relationship is that smaller toroidal surfaces correspond to $n_3 n_3$ approaching -1 (the closer the point on S^2 is to the south pole), and larger toroidal surfaces emerge when n_3 approaches 1 (the closer the point on S^2 is to the north pole). Finally, the constructed hopfions are nested toroidal surfaces with all different n_3.

It is worth noting that another type of topological texture, the skyrmionic hopfion, can be constructed using $\pi_3(S^3) = \mathbb{Z}$. In terms of the basic vector configuration, it appear similar to a conventional hopfion. However, in a skyrmionic hopfion, an additional phase factor can be introduced to each unit vector, along with a dimensional variable of 2π, thereby elevating the 2D spherical manifold of unit vectors to a 3D hypersphere. This elevates the classifying homotopy group from $\pi_3(S^2) = \mathbb{Z}$ to $\pi_3(S^3) = \mathbb{Z}$. As illustrated in Fig. 6(d) [38], which shows a Stokes-type skyrmionic hopfion, polarization vectors of the same orientation are represented by lines of the same color, forming a hopfion-like structure. Here, the phase of the polarization varies along each line despite the uniform orientation. This method of augmenting vectors with a phase dimension to construct higher-dimensional physical quantity manifold not only enables the realization of skyrmionic hopfions but also offers a feasible strategy for constructing 3D skyrmions in 3D space.

During the hopfion construction process, we can identify other intriguing topological textures. In Fig. 6(c), a simple link structure is formed in R^3 considering only two points on S^2. Links and knots, as basic topological textures, were initially developed in mathematics before their discovery in physics, representing ubiquitous topological phenomena. In fundamental topology, links and knots serve as foundational elements or intermediate configurations for complex high-dimensional topological textures,

including skyrmions and hopfions. In Fig. 6(e), we can see the profound connection between non-trivial topologies formed by links and knots and these higher-dimensional structures [110–115]. As shown in Fig. 6(e), skyrmions can form a skyrmion tube through layer-by-layer stacking with twist in configurations [116]. These skyrmion tubes can be connected head to tail to form links and knots [117]. A fundamental link configuration emerges when the skyrmion tube undergoes a 2π twist knots formed by vector circles, similar topological textures can arise from lines connecting singularities. Understanding these fundamental topologies and their interconnections facilitates the construction of diverse topological textures across physical systems. Knots and links are the model used by Maxwell and Lord Kelvin, which we introduced in the historical section. Not only are they topologically related to skyrmions, but they also historically inspired Skyrme's original thinking. Their topological properties are fundamentally different from those characterized by the homotopy groups of spheres. A detailed description lies beyond the scope of this tutorial and will not be further elaborated here.

Here, we have focused on the construction of several fundamental topological textures, including vortices, baby skyrmions, hopfions, knots, and links. Yet, the tapestry that topology can weave extends far beyond these examples. Through the framework of homotopy groups, a rich variety of higher-dimensional and hierarchically organized structures become attainable, such as 3D skyrmions, skyrmionic hopfions, skyrmion tubes, torons, hopfion crystals, heliknotons, and monopoles, among others [4,38,118–120], which will be discussed in Section 3.2.2. Many of these have already been realized experimentally in various condensed matter and optical systems. Looking forward, we anticipate even broader realizations and applications of such sophisticated topological architectures, particularly within photonics and emerging optical technologies. Moreover, we envision continued convergence between abstract mathematical concepts, especially from topology and geometry, and physical phenomena, inspiring future explorations along the visionary paths laid by great pioneers such as James Clerk Maxwell, Lord Kelvin, and Tony Skyrme.

3.1.4. Pioneering the Physics Parameter Space of Topological Textures

Throughout human history, the establishment of a kingdom has invariably been followed by expansion and exploration. Similarly, since entering the vision of physicists, topological textures have rapidly advanced into one physical system after another, embedding themselves across different parameter spaces. In this subsection, we retrace the path pioneered by Tony Skyrme, examining the path of pioneering physical parameter space of topological textures. Initially predicted within specific theoretical models, these topological textures have since been experimentally realized across a diverse range of physical platforms. It is important to note that such textures are not limited to these systems alone; in principle, any physical vector field can support such textures. Although a comprehensive overview of all developments in this vibrant field would be highly valuable, the scope of this review, with its particular emphasis on optical skyrmions, allows us to present only a selection and place the focus on the field of optics.

Skyrmions emerged from the Skyrme model in particle physics, where Tony Skyrme observed with a genius-like foresight that the normalized Skyrme field U corresponds to homotopy groups of spheres $\pi_3(S^3) = \mathbb{Z}$ [3,4]. These skyrmions represent unit 4-vector solitons. Then, this model is generalized to the Skyrme–Faddeev model, enabling the construction of hopfion and link structures [121]. As noted in the section of history, Skyrme's model eventually found extensive exploration in magnetism and evolved into a broader investigation of topological textures. In magnetism, the primary physical quantity initially used to construct baby skyrmions and such textures was

the magnetization vector [2,54,122–124]. Later, this framework was extended to other vectorial quantities such as spin vectors [125–127], significantly advancing the fields of magnetism and spintronics. During their development, spin–orbit coupling also played a significant role in generating and manipulating these magnetic skyrmions and other topological textures [128–130]. The dance of spin–orbital coupling within particles governs the rotation and dynamics of topological textures.

LCs and BECs serve as exceptionally rich platforms for the emergence and study of diverse topological textures, with the physical parameters being scalar or vectorial such as LC orientations, uniaxial LCs of rod-like molecular mesogens, ferromagnetic LC with magnetic physical quantities, and spin states of BECs [131–141]. Both systems support a variety of physical quantity to construct topological textures including vortices [138–140], skyrmions [133–138], and hopfions [138]. These structures arise as stable, topological configurations within LCs and BEC systems, whether in the director field of LCs or the macroscopic field properties of BECs. Their existence and behavior not only illustrate profound connections between topology and phase transitions but also offer avenues for exploring collective dynamics and potential applications in fields such as condensed matter physics and optical materials.

In optics, phase and polarization serve as the initial physical parameters in the construction of topological textures. Their precise manipulation enables the engineering of a wide range of structured light fields with non-trivial topologies, laying the foundation for realizing complex optical topological textures. Among these topological textures, optical vortices and singularities have been focal points of research since the 1989 discovery of phase vortices in laser cavities [142,143]. As scalar vortex structures that we discussed in Section 3.1.3, phase vortices, manifesting as optical scalar fields with helical phase fronts, carry orbital angular momentum (OAM) [144] and exhibit robust topological charges at their singularities. Usual phase optical vortices are distributed in spatial domain. In some other work, optical vortices are found to exist in spatiotemporal domain [145–147]. These spatiotemporal optical vortices provide a novel pathway to construct topological textures. Recent advances have enabled the realization of high-dimensional topological textures in spatiotemporal domain, leading to the generation of scalar hopfions constructed by phase [148]. Moreover, the singularities of phase vortex can generate links and knots [149]. The generation of vortex beams, scalar hopfions, links, and knots via phase offers an ideal platform to construct topological textures.

Beyond scalar fields, vector vortices emerge from polarization distributions. Projection of normalized Stokes vectors on a 2D plane or major axis of the polarization ellipse, forming normalized-2D-vector fields, can construct polarization vortices with polarization singularities. These polarization vortices manifest in various forms, including bound states in the continuum (BICs) in momentum space [150–152] and cylindrical vector beams in real space [153,154]. BICs in 2D photonic structures are vector vortices formed by eigen-polarization, exhibiting distinct topological properties and demonstrating capability for topological transformations, establishing connections between polarization vortex of BICs, phase vortex beams, and vector beams [155–159]. Cylindrical vector beams are vector vortices whose polarization state is spatially distributed in a cylindrical symmetry, typically exhibiting radial or azimuthal polarization patterns. Cylindrical vector beams, characterized by their topological stability and classical entanglement, serve as robust information carriers [160]. It is important to note that cylindrical vector beams differ fundamentally from optical vortex beams: the former are vectorial fields, whereas the latter are scalar in nature. As a result, their propagation properties and other physical behaviors exhibit distinct characteristics. For instance, cylindrical vector beams maintain their topological charge under mirror symmetry, whereas vortex beams experience a reversal of topological charge. Nevertheless, both

types of beams possess a central singularity and are topologically characterized by $\pi_1(S^1) = \mathbb{Z}$. Cylindrical vector beams can be regarded as an intermediate, bridging 1D scalar vortices and 2D vectorial textures such as Stokes skyrmions.

The vector vortices only utilize the in-plane vectors of the polarization to form circle manifolds in the plane, which are 1D topologies. In comparison, the polarization can be represented as Stokes vector that are normalized 3D vectors that can point to a solid angle of 4π with capability to form diverse topological textures. Among these topological textures, Stokes skyrmions are one of the focal points of this review. The Stokes skyrmions have emerged in diverse optical systems, usually generated by interference and superposition of light, exhibiting topological stability in propagation and showing potential for photonic applications. These Stokes skyrmions and their properties will be comprehensively introduced in the following sections. Besides, optical hopfions, links and knots are also observed in normalized Stokes vector fields [38,112,114,161].

The exploration of normalized Stokes vectors represents just one aspect of the rich landscape of topological textures in optical systems. Various physical quantities, including normalized spin vectors [14], field vectors [9], pseudospin vectors [162], and energy flux vectors [36], provide fertile ground for investigating skyrmions and related topological textures. In optics, the relevant physical quantities can be broadly categorized into those related to the field and those associated with spin. In the following sections, we will provide a detailed discussion on generation of optical skyrmions of these distinct types of parameters. Furthermore, the exploration of different wave systems has enabled the realization of a wide variety of topological textures, much as demonstrated in the historical overview of skyrmions presented earlier in this review. It should be emphasized again, however, that the exploration by physicists extends far beyond these established concepts. The field of topological physics continues to expand with the discovery of new physical vectors and the associated topological textures they support. These developments drive us to explore topological textures through an interdisciplinary pursuit.

After reviewing the general properties of topological textures classified by homotopy groups of spheres, we will focus specifically on skyrmions. In Section 3.2, we will present various topological configurations of skyrmions and analyze their related topological properties.

3.2. Topological Configurations and Connections of Optical Skyrmions

3.2.1. Different Types and Configurations of Optical Skyrmions

In this subsection, different types and configurations of optical skyrmions will be introduced (Fig. 7) [1,163]. Prior reviews of skyrmions have described the decomposition of the skyrmion number and its configurations using the example of symmetric skyrmions [1]. Here, we provide a generalizable measure applicable to a wider range of skyrmionic textures. The types and configurations of optical skyrmions rely on the distribution of physical vectors $\hat{\mathbf{n}}(r, \varphi)$, i.e., the spatial distribution manifolds. From a topological perspective, when the spatial distribution of vectors $\hat{\mathbf{n}}(r, \varphi)$ is mapped on the S^2 sphere of normalized 3D vectors in different ways, different types and configurations of optical skyrmions are constructed. In brief, the relation between spatial distribution $\hat{\mathbf{n}}(r, \varphi)$ and the S^2 sphere of normalized 3D vectors determines the types and configurations of optical skyrmions. Here, we can expand this relation as [1,163]:

$$\hat{\mathbf{n}}(r, \varphi) = (\cos \Theta(r, \varphi) \sin \Phi(r, \varphi), \sin \Theta(r, \varphi) \sin \Phi(r, \varphi), \cos \Phi(r, \varphi)), \quad \textbf{(3)}$$

Figure 7

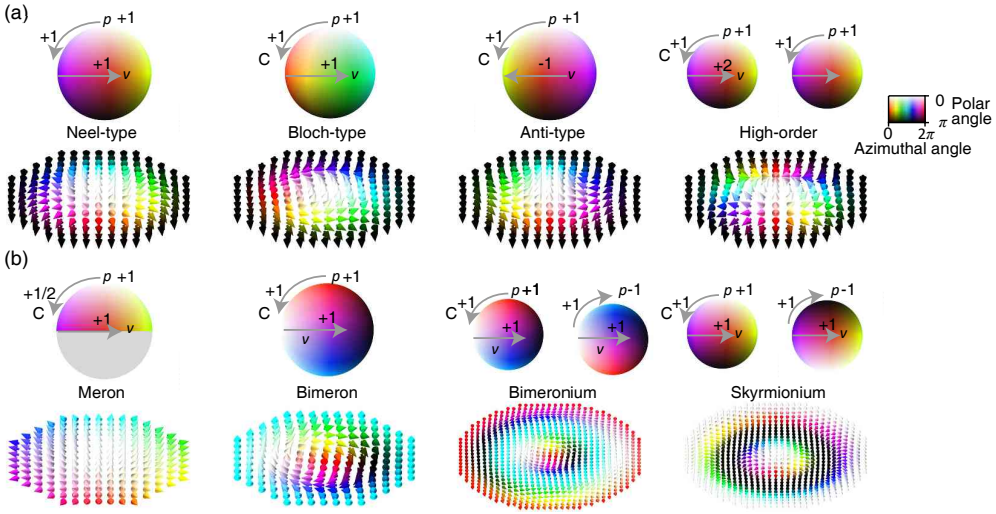

Classifications of skyrmions and other skyrmion-like topological configurations. (a) Different types of skyrmions, whose topological numbers are: Néel-type, $p = 1, v = 1$, and $\Phi_0 = 0$; Bloch-type, $p = 1, v = 1$, and $\Phi_0 = \frac{\pi}{2}$; anti-type, $p = 1, v = -1$, and $\Phi_0 = \pi$; high-order skyrmion, $p = 1, v = 2$, and $\Phi_0 = 0$. (b) Other topological configurations similar to skyrmion, including merons, bimerons, bimeroniums, and skyrmioniums. The wrapping structures of physical vector manifolds are shown in the top panel of (a) and (b).

where $\Theta(r, \varphi)$ and $\Phi(r, \varphi)$ are the polar and azimuthal angles of the S^2 sphere of normalized 3D vectors, with r and φ are the radial and azimuthal coordinates in the distribution-space manifolds R^2.

Equation (3) fundamentally describes the configuration of the skyrmion, but is obviously not intuitive enough. We can use some topological numbers to simplify this equation into intuitive physical pictures and corresponding degrees of freedom. In Section 3.1.3, a topological number of skyrmions, the skyrmion number, is quantified as an integer or half-integer number of times the vector field $\hat{\mathbf{n}}$ wraps the S^2 parameter sphere [Eq. (2)]. However, only a skyrmion number cannot describe complete configurations of optical skyrmions. Different types and configurations of optical skyrmions could have identical skyrmion numbers. Here, we divide the skyrmion number into more detailed topological numbers to comprehensively discuss the types of optical skyrmions, including polarity p, vorticity v, and helicity Φ_0 [1,163]. Just as polarity indicates directional properties in various physical systems, it is also used to define the orientation of vectors in skyrmions. In detail, polarity p classifies the direction of the unit vector $\hat{\mathbf{n}}(0, 0)$ at the skyrmion center: $p = +1$ corresponds to an upward orientation, and $p = -1$ for down direction. Vorticity v defines the in-plane rotation behavior of the vector field $\hat{\mathbf{n}}(r, \varphi)$ along a counterclockwise loop around the center of skyrmions, being positive for counterclockwise and negative for clockwise, and the value of vorticity v describes the winding number of in-plane rotation. If the skyrmion is symmetric with azimuthal angle $\Phi(r, \varphi)$ satisfying $\Phi(r, \varphi) = v\varphi + \Phi_0$, we can define helicity Φ_0. Helicity Φ_0 is an initial phase that determines the specific orientation of the vectors $\hat{\mathbf{n}}(r, \varphi)$. The skyrmion number N_{sk} of skyrmions can be expressed as:

$$N_{sk} = p \cdot v. \tag{4}$$

Beyond skyrmions, there are other skyrmion-like configurations with similar characteristics, such as merons, bimerons, bimeroniums, and skyrmioniums. Notably, there have

been primarily two widely used formulations regarding the definition of skyrmion number of these configurations: one is $N_{sk} = p' \cdot \nu$, where the polarity $p' = Cp$ incorporates the out-of-plane component variation [1,107]; the other is $N_{sk} = Cp \cdot \nu$, where p takes binary values as we defined before, commonly used in both magnetic vortex studies (which are actually magnetic merons) [122,164–167] and recent meron researches [163,168,169]. Here, C characterizes the change in the out-of-plane component n_z of the vector field $\hat{\mathbf{n}}$ from center to boundary $\boldsymbol{r_c}$: $C = |n_z(\boldsymbol{r} = 0) - n_z(\boldsymbol{r} = \boldsymbol{r_c})|/2$. Both of the definitions can describe these configurations well. The difference lies only in whether the change of the out-of-plane components is incorporated into the polarity or the skyrmion number. In this tutorial, we adopt the latter definition. For example, the vectors of merons change from out of plane to in-plane, corresponding to $C = \frac{1}{2}$, and the skyrmion number equals half the product of polarity and vorticity.

We can understand different types and configurations of optical skyrmions in the spatial distribution manifolds, as shown in the bottom panel of Fig. 7. These configurations can also be understood in physical vector manifolds S^2 (top panel of Fig. 7). In the S^2 manifolds, p determines polar angle coverage direction, C determines polar angle coverage rate, and ν determines both azimuthal angle coverage direction and the total number of physical vector manifolds S^2.

Figure 7(a) shows a series of representative types of skyrmions with $C = 1$, such as Néel-type, Bloch type, anti-type, and a high-order skyrmion, which is controlled by these topological numbers. The Néel-type skyrmion is characterized by the case of $p = 1$, $\nu = 1$, and the initial phase $\Phi_0 = 0$ or π. While the Bloch-type, which has the same polarity and vorticity as the Néel-type, differs in phase $\Phi_0 = \pm\pi/2$. The anti-type skyrmion has $p = 1$, but its vorticity is reversed with $\nu = -1$. High-order skyrmions, which have $|s| > 1$, represent more complex configurations where the vector field wraps the sphere multiple times. For instance, the high-order skyrmion in Fig. 7(a) with $N_{sk} = 2$ can be described by $p = 1$, $\nu = 2$, and $\Phi_0 = 0$, indicating that the vector field completes two full rotations as it wraps S^2.

Figure 7(b) illustrates a series of configurations of skyrmion-like textures, including a meron, a bimeron, a bimeronium, and a skyrmionium [170]. A meron is a fractional topological texture with a skyrmion number of $N_{sk} = \pm\frac{1}{2}$. Unlike a full skyrmion, which wraps the entire S^2 parameter sphere, a meron with $C = \frac{1}{2}$ only covers half of it, resulting in a fractional charge. When two merons with identical charges and opposite polarity $(N_{sk} = +\frac{1}{2}, p = 1, \nu = 1$ and $N_{sk} = +\frac{1}{2}, p = -1, \nu = -1)$ combine, they form a bimeron, which is a topological texture with $N_{sk} = 1$. The bimeron is like a special case of skyrmions, with orthogonal in-plane vector $\hat{\mathbf{n}}(r, \varphi) = (\cos\Theta(r, \varphi), \sin\Theta(r, \varphi), 0)$ at center and at the boundaries instead of orthogonal perpendicular vectors $\hat{\mathbf{n}}(r, \varphi) = (0, 0, \pm 1)$. Notably, a bimeronium is an extended version of a bimeron, composed of multiple bimerons arranged in a configuration with $C = 0$ and a topological charge of $Q = 0$. Similarly, a skyrmionium is a topologically neutral texture $(N_{sk} = 0)$. Bimeronium and skyrmionium with $C = 0$ wrap the sphere twice in opposite directions, leading to cancellation of the topological charge. Structurally, a bimeronium (a skyrmionium) can be viewed as a bimeron (skyrmion) wrapped by another bimeron (skyrmion) of opposite charge, forming a toroidal-like configuration [e.g., $N_{sk} = +1, C = 1, p = 1, \nu = 1, \Phi_0 = 0$ and $N_{sk} = -1, C = 1, p = -1, \nu = 1, \Phi_0 = 0$ in Fig. 7(b)].

3.2.2. Connections between Optical Skyrmions and Other Related Topological Textures

Optical skyrmions share profound and intricate relationships with various other topological structures. This section examines these connections to illustrate how skyrmions not only bridge different dimensions of topology but also serve as building blocks for

Figure 8

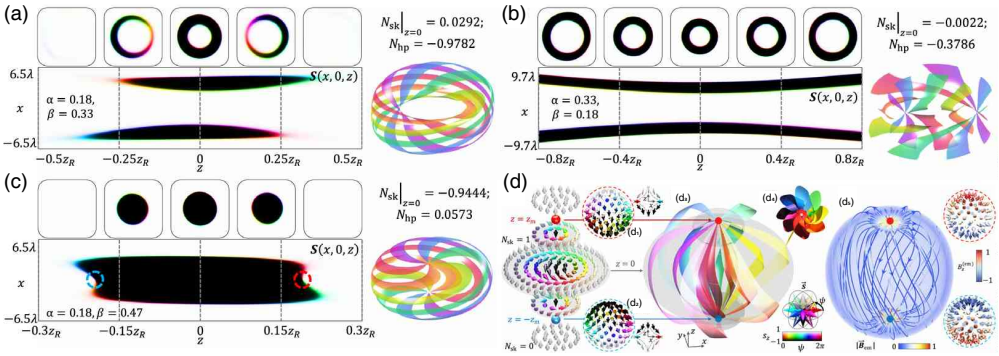

3D topological textures. The cross-sections (left) and the schematic diagram (right) of topological textures, including (a) a hopfion, (b) skyrmionium tube, (c) toron. (d) Concept of torons and monopoles, resembling a topological "pinwheel" [124]. Reprinted with permission from Wu *et al.*, Phys. Rev. Lett. **135**, 063802 (2025), Ref. [124]. Copyright 2025 by the American Physical Society.

increasingly complex configurations. Understanding these relationships enriches our insight into topological photonics and facilitates the development of novel approaches for light field manipulations.

The connection between vortices and skyrmions forms a foundational relationship. Vortices exist naturally within skyrmionic textures: ignoring the out-of-plane component of a skyrmion, the in-plane vector field reveals a vortex-like singularity. This structural similarity has inspired practical methods for skyrmion generation, where vortices act as templates. By interferometric control of phase and polarization in vortex beams, researchers can construct skyrmions, effectively "folding" scalar phase singularities into vectorial topological entities [13,23,36,37].

This low-to-high dimensional interplay motivates the search for deeper topological connections. Just as vortices underlie 2D skyrmions, skyrmions are embedded within higher-dimensional textures, guiding the exploration of 3D topological structures [38,124,171]. This perspective not only aids in generating and characterizing new skyrmion variants but also enhances our ability to harness higher-dimensional topology. The cross-sections of hopfions along the axial direction reveal embedded skyrmionic textures, as shown in Fig. 8(a) [124], affirming the structural continuity between the two. Another simple 3D extension of a skyrmion is the skyrmion tube, in which the 2D skyrmion profile is extruded along the propagation axis. As illustrated in Fig. 8(b), a skyrmionium tube is one such tubular structure. Here, hopfions can be viewed as twisted and closed skyrmion tubes. Imagine grasping both ends of a skyrmion tube, twisting one end by 360°, and connecting them to form a toroidal structure. This process generates a hopfion, the same as the formation of link structures depicted in Fig. 6(e). Interestingly, when multiple skyrmion tubes are closely packed together in space, they can form a stable cluster known as a skyrmion bundle [172].

Further exploration leads to richer constructs. Fig. 8(c) illustrates a toron, which can be conceptualized as a skyrmion tube whose ends are pinched into point defects known as monopoles. The monopoles act as a high-dimensional vortex-like counterparts, where vectors rotate around monopoles in different directions. Fig. 8(d) illustrates the configurations of toron and monopole. Here, the toron resembles a topological "pinwheel," with monopoles at its poles and skyrmion-like textures in cross-section. Recent studies have demonstrated continuous topological phase transition, from toron, hopfion, skyrmionium to monopole pairs [124]. This dynamic reconfiguration,

Figure 9

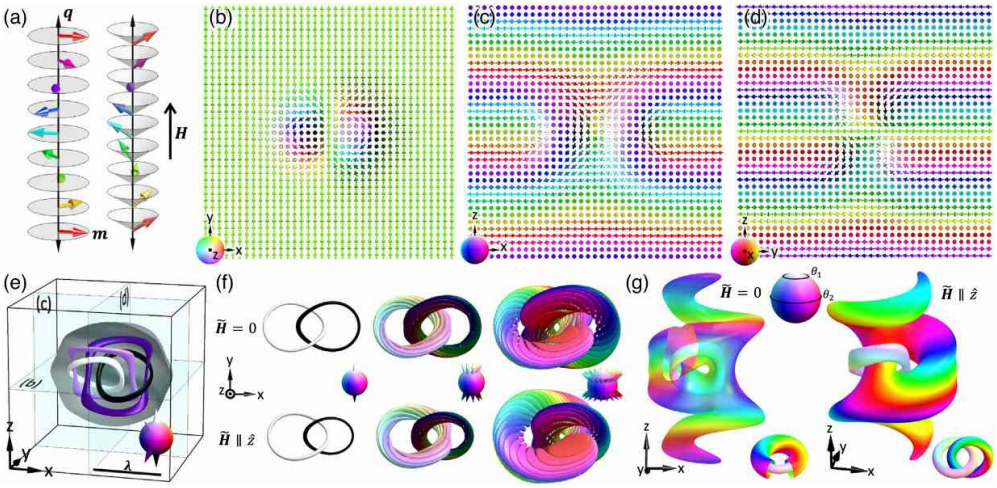

Heliknotons and the inherent link structures. (a) Helical (left) and conical vectors (right). (b)–(d) Cross-sections of a heliknoton. (e) and (f) The inherent link structures of the heliknoton. (g) Manipulation of the magnetic heliknoton via the helical field [173]. Reprinted with permission from Voinescu *et al.*, Phys. Rev. Lett. **125**, 057201 (2020), Ref. [173]. Copyright 2020 by the American Physical Society.

analogous to "blowing a topological pinwheel," not merely offers an intuitive visualization but also underscores the profound structural and topological kinship among these textures. Moreover, applying helical modulation to hopfions leads to the emergence of heliknotons—spirally twisted topological structures that preserve the fundamental Hopf fibration but exhibit distinct configurations [118,173–175]. As shown in Fig. 9, these entities retain linked-loop configurations reminiscent of hopfions. Even in these sophisticated constructs, skyrmionic textures remain perceptible, reaffirming significance of connections between topological textures.

In higher-dimensional topologies such as skyrmionic hopfions and 3D skyrmions, skyrmionic textures will also be present. Just as collapsing a dimension in a skyrmion reveals a vortex, projecting certain dimensions of a skyrmionic hopfion or a 3D skyrmion exposes underlying skyrmionic substructures [38]. These cases suggest that high-dimensional topological textures inherently contain lower-dimensional ones, providing a unified perspective for designing and analyzing complex topological textures. These researches into higher-dimensional configurations also represent a pivotal step toward translating skyrmion studies from fundamental physics into practical applications, addressing key challenges such as the efficient and reliable large-scale integration and manipulation of these topological structures.

Besides connections between textures in different dimensions, the spatial distribution of these topological structures can also give rise to interesting phenomena. Multiple skyrmions inside a definite boundary can form a skyrmion bag. If arranged in periodic patterns, these topological textures can form new structures such as skyrmion lattice [9,11,176] or hopfion crystals [177], which extends both individual topological characteristics and collective behavior of original topological textures. These highly dense and stable periodic structures in space are the key to realize the application of topological textures in robust high-density information storage and transmission.

The deep and varied relationships between optical skyrmions and other topological textures significantly advance our understanding of topological light. These connections provide not only a theoretical foundation for complex topological designs but also

practical pathways toward innovative applications in optical sensing, communication, and manipulation. Future research may utilize these connections to unveil new topological textures and their unique properties in photonic systems.

4. GENERATION OF OPTICAL SKYRMIONS

In this section, we present a comprehensive, derivation-focused tutorial on optical skyrmion generations, building from fundamental principles to advanced implementations. Starting with basic wave interference, we systematically demonstrate how skyrmionic fields emerge analytically, progressing from simple configurations to higher-order structures. Then, we generalize the underlying physical mechanisms and finally present current implementation methods. This step-by-step, pedagogical approach is designed to offer an intuitive and comprehensive understanding of how skyrmions are generated. It serves as a necessary complement to existing reviews and tutorials [1,28–33] by emphasizing conceptual derivation and mechanistic insight, for which detailed and accessible theoretical models are still urgently needed.

4.1. Field-Related Skyrmions

Optical field skyrmions are topological structures that emerge in electromagnetic fields, typically characterized through the electric field components of light. These skyrmionic configurations are commonly generated via the interference of surface evanescent waves—electromagnetic modes that decay exponentially away from an interface. Such interference can produce periodic lattice or quasicrystalline arrangements of field skyrmions. A prominent example involves surface plasmon polaritons (SPPs), which are surface-bound waves coupled to electron density oscillations in metals, as demonstrated in [9,11].

We now present a general derivation of field skyrmion formation through the interference of SPP waves propagating along different directions. Starting from Eq. (2), we define the normalized vector $\hat{\mathbf{n}}$. For an electric-field skyrmion, this vector is expressed as:

$$\hat{\mathbf{n}} = \frac{\left(\mathrm{Re}\{E_x\}, \mathrm{Re}\{E_y\}, \mathrm{Re}\{E_z\}\right)}{\sqrt{\mathrm{Re}\{E_x\}^2 + \mathrm{Re}\{E_y\}^2 + \mathrm{Re}\{E_z\}^2}}, \tag{5}$$

where the real parts of the electric field components are used to capture the instantaneous, measurable field orientation at a given time.

A single SPP wave with wavevector $\mathbf{k} = (k_\parallel \cos\alpha, k_\parallel \sin\alpha, -\mathrm{i}\kappa_z)^T$ is described by the electric field:

$$\mathbf{E} = E_0 \begin{pmatrix} \frac{\mathrm{i}\kappa_z \cos\alpha}{k_\parallel} \\ \frac{\mathrm{i}\kappa_z \sin\alpha}{k_\parallel} \\ 1 \end{pmatrix} \mathrm{e}^{\mathrm{i}\omega t - \mathrm{i}[k_\parallel (x\cos\alpha + y\sin\alpha) - \mathrm{i}\kappa_z z]}. \tag{6}$$

For the interference of N such waves, the total electric field becomes:

$$\mathbf{E} = \sum_{m=1}^{N} \mathbf{E}_m = \sum_{m=1}^{N} E_m \begin{pmatrix} \frac{\mathrm{i}\kappa_z \cos\alpha_m}{k_\parallel} \\ \frac{\mathrm{i}\kappa_z \sin\alpha_m}{k_\parallel} \\ 1 \end{pmatrix} \mathrm{e}^{\mathrm{i}\omega t - \mathrm{i}[k_\parallel (x\cos\alpha_m + y\sin\alpha_m) - \mathrm{i}\kappa_z z]}. \tag{7}$$

In the following analysis, we assume equal amplitudes E_m for all waves and restrict our discussion to the plane $z = 0$.

We begin by analyzing the simplest case involving two SPP waves, which will later be extended to general N-wave configurations. Without loss of generality, we assume $\alpha_2 = -\alpha_1$ and $E_1 = E_2 = E_0 \in \mathbb{R}^+$. The total interference field is given by:

$$\begin{aligned}\mathbf{E} &= E_0 \mathrm{e}^{\mathrm{i}\omega t - \mathrm{i}k_\parallel(x\cos\alpha_1 + y\sin\alpha_1) - \kappa_z z}\begin{pmatrix}\frac{\mathrm{i}\kappa_z\cos\alpha_1}{k_\parallel}\\ \frac{\mathrm{i}\kappa_z\sin\alpha_1}{k_\parallel}\\ 1\end{pmatrix}\\ &\quad + E_0 \mathrm{e}^{\mathrm{i}\omega t - \mathrm{i}k_\parallel(x\cos\alpha_1 - y\sin\alpha_1) - \kappa_z z}\begin{pmatrix}\frac{\mathrm{i}\kappa_z\cos\alpha_1}{k_\parallel}\\ -\frac{\mathrm{i}\kappa_z\sin\alpha_1}{k_\parallel}\\ 1\end{pmatrix}\\ &= 2E_0 \mathrm{e}^{\mathrm{i}\omega t - \mathrm{i}k_\parallel x\cos\alpha_1 - \kappa_z z}\begin{pmatrix}\frac{\mathrm{i}\kappa_z\cos\alpha_1}{k_\parallel}\cos(k_\parallel y\sin\alpha_1)\\ \frac{\kappa_z\sin\alpha_1}{k_\parallel}\sin(k_\parallel y\sin\alpha_1)\\ \cos(k_\parallel y\sin\alpha_1)\end{pmatrix}.\end{aligned} \tag{8}$$

Let $\theta = 2\alpha_1$ denote the angle between the two wavevectors. The real part of the electric field, which determines the measurable instantaneous field distribution, is:

$$\mathrm{Re}\,\mathbf{E} = 2E_0 \mathrm{e}^{-\kappa_z z}\begin{pmatrix}-\frac{\kappa_z}{k_\parallel}\cos\frac{\theta}{2}\cos(k_\parallel y\sin\frac{\theta}{2})\sin(\omega t - k_\parallel x\cos\frac{\theta}{2})\\ \frac{\kappa_z}{k_\parallel}\sin\frac{\theta}{2}\sin(k_\parallel y\sin\frac{\theta}{2})\cos(\omega t - k_\parallel x\cos\frac{\theta}{2})\\ \cos(k_\parallel y\sin\frac{\theta}{2})\cos(\omega t - k_\parallel x\cos\frac{\theta}{2})\end{pmatrix}. \tag{9}$$

Based on Eq. (9), the time evolution of the normalized electric field distribution in the xy-plane can be analyzed for the interference of two SPP waves with an inter-wave angle θ between their propagation directions. As illustrated in Fig. 10, the resulting structure forms a rectangular meron lattice with a unit cell size of $\frac{2\pi}{k_\parallel}\csc\frac{\theta}{2} \times \frac{2\pi}{k_\parallel}\sec\frac{\theta}{2}$. The electric field intensity remains invariant every half-period, $\frac{\pi}{\omega}$, while the field direction undergoes a complete reversal, i.e., $\hat{\mathbf{n}} \to -\hat{\mathbf{n}}$ as $t \to t + \frac{\pi}{\omega}$, leading to a sign change in the skyrmion number according to Eq. (2). It is also noteworthy that the lattice propagates along the x-axis, as evidenced by the propagating phase term $(\omega t - k_\parallel x\cos\frac{\theta}{2})$ in each electric field component in Eq. (9). The propagation speed along x-axis is given by $\frac{\omega}{k_\parallel}\sec\frac{\theta}{2}$.

Having discussed meron lattice formation via two-wave interference, we now turn to the case of three SPP waves. The total electric field can be expressed as:

$$\begin{aligned}\mathbf{E} &= 2E_0 \mathrm{e}^{\mathrm{i}(\omega t - k_\parallel x\cos\alpha_1) - \kappa_z z}\begin{pmatrix}\frac{\mathrm{i}\kappa_z\cos\alpha_1}{k_\parallel}\cos(k_\parallel y\sin\alpha_1)\\ \frac{\kappa_z\sin\alpha_1}{k_\parallel}\sin(k_\parallel y\sin\alpha_1)\\ \cos(k_\parallel y\sin\alpha_1)\end{pmatrix}\\ &\quad + E_0 \mathrm{e}^{\mathrm{i}[\omega t - k_\parallel(x\cos\alpha_3 + y\sin\alpha_3)] - \kappa_z z}\begin{pmatrix}\frac{\mathrm{i}\kappa_z\cos\alpha_3}{k_\parallel}\\ \frac{\mathrm{i}\kappa_z\sin\alpha_3}{k_\parallel}\\ 1\end{pmatrix},\end{aligned} \tag{10}$$

where $\alpha_3 \neq \pm\alpha_1$. To study a symmetric configuration conducive to periodic lattice formation, we set $\alpha_3 = 0$:

Figure 10

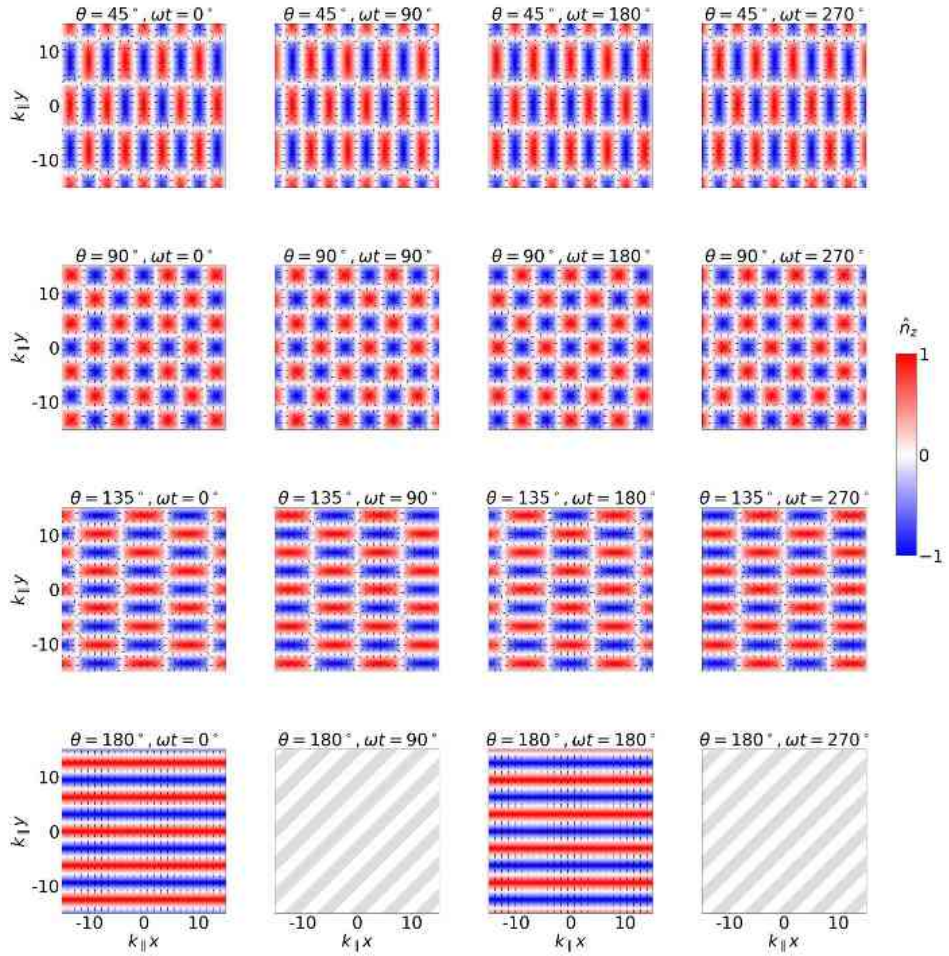

Meron distributions for different lattice configurations formed by propagation of 2 SPP waves with different included angle θ. The unit vector $\hat{\mathbf{n}}$ is represented by colors (vertical component $\hat{n}_z$) and black arrows (horizontal component $(\hat{n}_x, \hat{n}_y)$). Notice that for $\theta = 180°$, the real electric field undergo complete destructive interference at $\omega t = 90°, 270°$, corresponding to a uniform $\hat{\mathbf{n}} = 0$ state over the entire plane, visually indicated by blank areas featuring parallel oblique gray stripes.

$$\mathbf{E} = 2E_0 \mathrm{e}^{\mathrm{i}(\omega t - k_\parallel x \cos\alpha_1) - \kappa_z z} \begin{pmatrix} \frac{\mathrm{i}\kappa_z \cos\alpha_1}{k_\parallel} \cos(k_\parallel y \sin\alpha_1) \\ \frac{\kappa_z \sin\alpha_1}{k_\parallel} \sin(k_\parallel y \sin\alpha_1) \\ \cos(k_\parallel y \sin\alpha_1) \end{pmatrix} + E_0 \begin{pmatrix} \frac{\mathrm{i}\kappa_z}{k_\parallel} \\ 0 \\ 1 \end{pmatrix} \mathrm{e}^{\mathrm{i}(\omega t - k_\parallel x) - \kappa_z z}. \tag{11}$$

On the y-direction, the spatial period is determined by $k_\parallel \sin\alpha_1$, while in the x-direction, two spatial period components are present: $k_\parallel \cos\alpha_1$ and $k_\parallel$. To achieve a periodic texture, the ratio $\frac{k_\parallel}{k_\parallel \cos\alpha_1}$ must be an integer. Here, we take $\alpha_1 = 120°$, giving $\cos\alpha_1 = -\frac{1}{2}$. Thus, we obtain a distribution with at least a 3-fold symmetry:

$$\mathrm{Re}\,\mathbf{E} = \frac{E_0 \mathrm{e}^{-\kappa_z z}}{2} \begin{pmatrix} \frac{\kappa_z}{k_\parallel}\left[\sin\left(\frac{1}{2}k_\parallel x + \frac{\sqrt{3}}{2}k_\parallel y + \omega t\right) + \sin\left(\frac{1}{2}k_\parallel x - \frac{\sqrt{3}}{2}k_\parallel y + \omega t\right) - 2\sin\left(-k_\parallel x + \omega t\right)\right] \\ \frac{\sqrt{3}\kappa_z}{k_\parallel}\left[\sin\left(\frac{1}{2}k_\parallel x + \frac{\sqrt{3}}{2}k_\parallel y + \omega t\right) + \sin\left(-\frac{1}{2}k_\parallel x + \frac{\sqrt{3}}{2}k_\parallel y - \omega t\right)\right] \\ \cos\left(\frac{1}{2}k_\parallel x + \frac{\sqrt{3}}{2}k_\parallel y + \omega t\right) + \cos\left(-\frac{1}{2}k_\parallel x + \frac{\sqrt{3}}{2}k_\parallel y - \omega t\right) + \cos\left(k_\parallel x - \omega t\right) \end{pmatrix}. \tag{12}$$

Figure 11

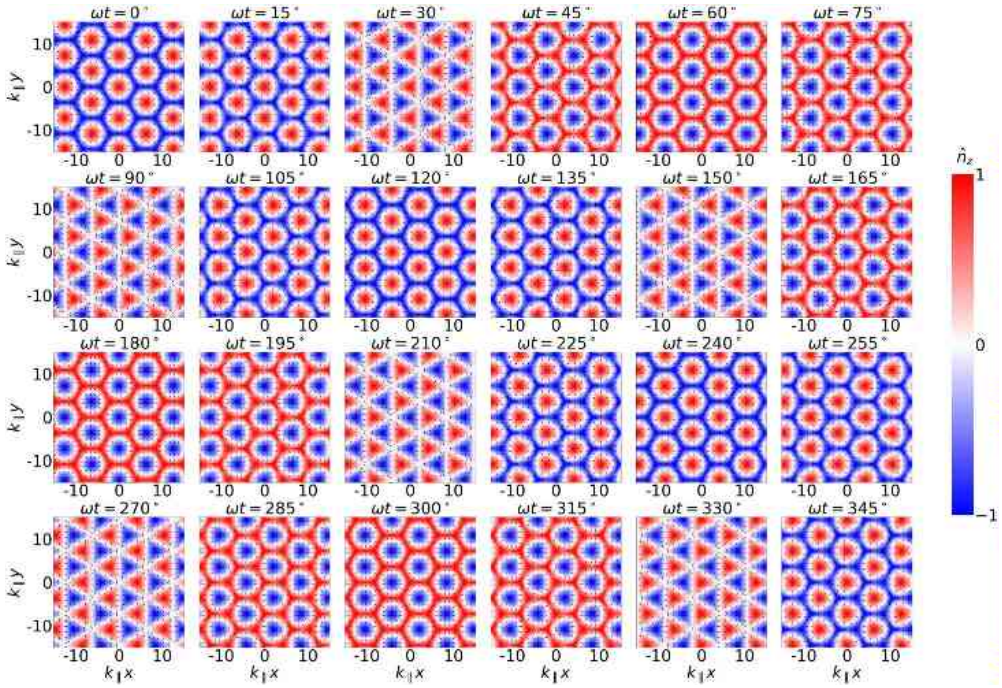

Skyrmion and meron distributions in various lattice configurations formed by the propagation of three SPP waves, with 120° included angle between adjacent propagating waves, during one period of time evolution. The unit vector $\hat{\mathbf{n}}$ is represented by colors (vertical component $\hat{n}_z$) and black arrows (horizontal component $(\hat{n}_x, \hat{n}_y)$).

From Eq. (12), when three SPP waves interfere in an equilateral triangular configuration with 120° between propagation directions, the time evolution of the normalized electric field in the xy-plane is shown in Fig. 11. The interference produces a hexagonal skyrmion lattice for $\omega t \neq (n+\frac{1}{2})60°$, with the skyrmion number reversing sign (from ± 1 to ∓ 1) every $\frac{1}{6}$-period. At instants where $\omega t = (n+\frac{1}{2})60°$, a triangular meron lattice appears, and integrating over the hexagonal unit cell yields a skyrmion number of zero.

We can explain this behavior quantitatively: according to Eq. (12), when $\omega t \to \omega t + 60°$, the electric field satisfies $\mathbf{E} \to -\mathbf{E}$. At $\omega t = (n+\frac{1}{2})60°$, certain vertices exhibit $\mathrm{Re}\,\mathbf{E} = 0$, leading to $\hat{\mathbf{n}} = 0$ at those points, which form the vertices of the triangular unit cell. Furthermore, every $\frac{1}{6}$ of a period, the skyrmion configuration undergoes a sign reversal and is displaced by $-\frac{4\pi}{3k_\parallel}$ along the x-axis.

In a more general case of N-wave interference with the same complex amplitude and equal included angle, we still define the inter-beam angle as θ. The wavevectors form a regular N-gon, satisfying C_N symmetry, and can give rise to mixed topological quasicrystals of skyrmions and merons [178]. Setting the propagation angle of the m-th wave as $\alpha_m = (m-1)\theta = \frac{2\pi(m-1)}{N}$, the resulting field configurations are illustrated in Fig. 12. Here, we analyze the evolution of optical field skyrmions over one period $t = 0$ to $t = \frac{2\pi}{\omega}$ for different N and summarize the distinctive behaviors for even and odd N.

- Firstly, we discuss the field evolution for even N over one period. When $(n-\frac{1}{2})\pi < \omega t < (n+\frac{1}{2})\pi$, the configuration of (normalized) electric field remain unchanged. At $\omega t = (n+\frac{1}{2})\pi$, the real part of the electric field vanishes, resulting in no

Figure 12

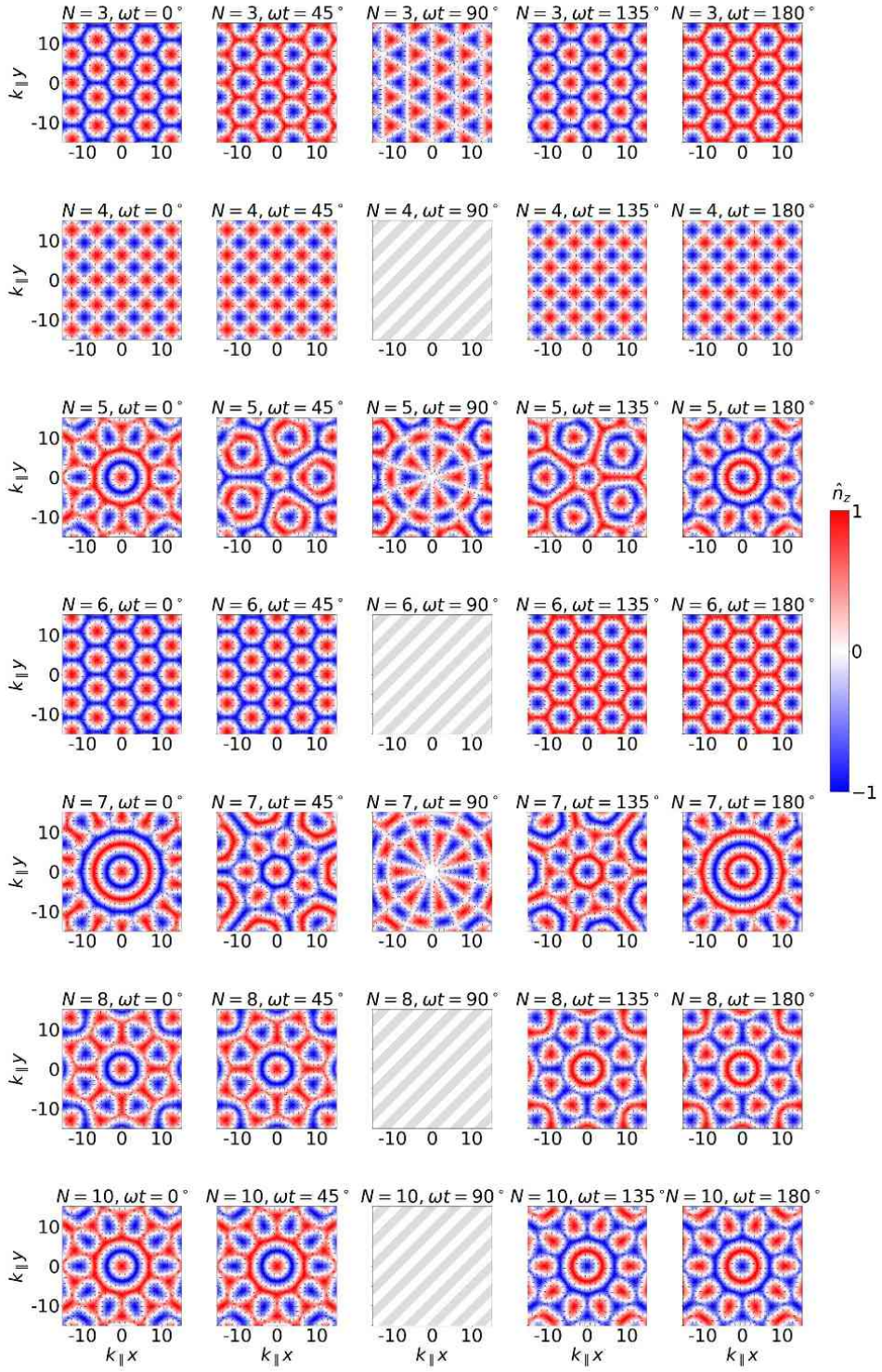

Skyrmion and meron distributions formed by propagation of N SPP waves with spacing of propagating direction of $\frac{2\pi}{N}$ during time evolution. The unit vector $\hat{\mathbf{n}}$ is represented by colors (vertical component $\hat{n}_z$) and black arrows (horizontal component $(\hat{n}_x, \hat{n}_y)$). Notice that for $N = 4, 6, 8, 10$, the real electric field undergo complete destructive interference $\omega t = 90^\circ$, corresponding to a uniform $\hat{\mathbf{n}} = 0$ state over the entire plane, visually indicated by blank areas featuring parallel oblique gray stripes.

definable configuration. For $(n+\frac{1}{2})\pi < \omega t < (n+\frac{3}{2})\pi$, the field configuration reappears identical to that in the previous half-period, but with all field directions reversed. This invariance of the configuration arises because each propagating wave has a counterpart traveling in the opposite direction, forming a standing wave. We illustrate this by considering the standing wave formed by $\mathbf{E}_m$ and $\mathbf{E}_{m+\frac{N}{2}}$ (with $m \le \frac{N}{2}$):

$$\begin{aligned}\mathbf{E}_m + \mathbf{E}_{m+\frac{N}{2}} &= E_0 \begin{pmatrix} \frac{\mathrm{i}\kappa_z \cos\alpha_m}{k_\parallel} \\ \frac{\mathrm{i}\kappa_z \sin\alpha_m}{k_\parallel} \\ 1 \end{pmatrix} \mathrm{e}^{\mathrm{i}\omega t - \mathrm{i}[k_\parallel(x\cos\alpha_m + y\sin\alpha_m) - \mathrm{i}\kappa_z z]} \\ &\quad + E_0 \begin{pmatrix} -\frac{\mathrm{i}\kappa_z \cos\alpha_m}{k_\parallel} \\ -\frac{\mathrm{i}\kappa_z \sin\alpha_m}{k_\parallel} \\ 1 \end{pmatrix} \mathrm{e}^{\mathrm{i}\omega t - \mathrm{i}[-k_\parallel(x\cos\alpha_m + y\sin\alpha_m) - \mathrm{i}\kappa_z z]} \\ &= 2E_0 \mathrm{e}^{\mathrm{i}\omega t - \kappa_z z} \begin{pmatrix} \frac{\kappa_z}{k_\parallel}\cos\alpha_m \sin(k_\parallel(x\cos\alpha_m + y\sin\alpha_m)) \\ \frac{\kappa_z}{k_\parallel}\sin\alpha_m \sin(k_\parallel(x\cos\alpha_m + y\sin\alpha_m)) \\ \cos(k_\parallel(x\cos\alpha_m + y\sin\alpha_m)) \end{pmatrix}. \end{aligned} \tag{13}$$

Summing over all such standing-wave pairs and taking the real part gives:

$$\begin{aligned}(\mathrm{Re}\,\mathbf{E})_N &= \mathrm{Re} \sum_{m=1}^{\frac{N}{2}} (\mathbf{E}_m + \mathbf{E}_{m+\frac{N}{2}}) \\ &= \mathrm{Re} \sum_{m=1}^{\frac{N}{2}} 2E_0 \mathrm{e}^{\mathrm{i}\omega t - \kappa_z z} \begin{pmatrix} \frac{\kappa_z}{k_\parallel}\cos\alpha_m \sin(k_\parallel(x\cos\alpha_m + y\sin\alpha_m)) \\ \frac{\kappa_z}{k_\parallel}\sin\alpha_m \sin(k_\parallel(x\cos\alpha_m + y\sin\alpha_m)) \\ \cos(k_\parallel(x\cos\alpha_m + y\sin\alpha_m)) \end{pmatrix} \\ &= 2E_0 \cos\omega t \mathrm{e}^{-\kappa_z z} \sum_{m=1}^{\frac{N}{2}} \begin{pmatrix} \frac{\kappa_z}{k_\parallel}\cos\alpha_m \sin(k_\parallel(x\cos\alpha_m + y\sin\alpha_m)) \\ \frac{\kappa_z}{k_\parallel}\sin\alpha_m \sin(k_\parallel(x\cos\alpha_m + y\sin\alpha_m)) \\ \cos(k_\parallel(x\cos\alpha_m + y\sin\alpha_m)) \end{pmatrix}. \end{aligned} \tag{14}$$

This expression shows that the spatial pattern remains unchanged when $\cos\omega t \neq 0$ and vanishes when $\cos\omega t = 0$. For every half period $\frac{\pi}{\omega}$, the normalized electric field distribution changes sign, leading to a reversal in the skyrmion number N_{sk}. As seen in Fig. 12, a Néel-type skyrmion is located at the center when $\omega t = n\pi$.

- Next, we consider the case of odd N. Here, no wave has a direct counterpart propagating in the exact opposite direction to form a standing wave. Thus, the field configuration evolves continuously in time, as illustrated in Fig. 12. In particular, at phases satisfying $\omega t = (n+1/2)\pi$, the configuration transitions from a skyrmion texture to a meron texture exhibiting C_N symmetry.

In summary, when N SPP waves interfere in a normalized field configuration forming a regular polygon under C_N symmetry, the optical field skyrmion evolves periodically in time, accompanied by periodic sign reversals of the skyrmion number. Under specific symmetric arrangements such as C_3, C_4, or C_6, different skyrmion or meron textures in periodic lattice emerge. For C_3 symmetry, a hexagonal skyrmion lattice emerges at $\omega t = \frac{n\pi}{3}$ and equilateral triangular lattice of meron will emerge at $\omega t = (\frac{n}{3} + \frac{1}{6})\pi$. For C_4 symmetry, a square skyrmion lattice emerges at $\omega t = n\pi$. For C_6 symmetry, a

Table 2. Skyrmion and Meron Configuration of SPP Wave Interference with C_N Symmetry ($N > 2$) at $\omega t = \frac{m}{2}\pi,\ m \in \mathbb{Z}$[a]

N	$\omega t = n\pi,\ n \in \mathbb{Z}$	$\omega t = \left(n + \frac{1}{2}\right)\pi,\ n \in \mathbb{Z}$
3	Néel-type skyrmions distributed in a hexagonal lattice	Néel-type merons distributed in a equilateral triangular lattice
4	Néel-type merons in a square lattice distribution	/
6	Néel-type skyrmions distributed in a hexagonal lattice	/
Other odd N	A Néel-type skyrmion located in the center	Néel-type merons distributed around the center with C_N symmetry
Other even N	A Néel-type skyrmion located in the center	/

[a]Here we define at $t = 0$ each SPP wave has pure real z-component.

hexagonal skyrmion lattice emerges at $\omega t = n\pi$. For other regular polygon configurations, quasicrystalline tilings are obtained. A summary of these general conclusions is provided in Table 2.

The construction of optical skyrmions often relies on such multi-wave interferences with C_N symmetry. In one pioneering approach, a hexagonal array of coupling slits fabricated on a metallic surface excites field skyrmions via SPPs propagating along six defined directions [9], as illustrated in Fig. 13(a). The interference of these SPP waves produces a periodic lattice, imaged via scattering-type near-field optical microscopy with sub-diffraction resolution, revealing a Néel-type skyrmion lattice. The axial field component in this configuration is approximately five times stronger than the transverse components, yielding a distinct bubble-like texture. Skyrmions have also been generated through multi-wave interferences and probed through two-photon photoemission excited by femtosecond laser pulses [11], with time-dependent dynamics, including electric field reversals, captured using photoemission electron microscopy.

While early studies centered on electric-field skyrmions in evanescent wave systems [9,13], recent work demonstrates that magnetic-field components can also support topologically non-trivial textures. For instance, magnetic-field skyrmions and merons have been realized in Bloch surface wave lattices [179], where the evanescent magnetic fields of surface modes form skyrmionic lattices with high uniformity and low propagation loss, offering a robust platform for nanoparticle manipulation and spin-momentum-locked light–matter interactions. The core of these methods is the same. Through the design of a special structure, it guides the multi-wave interference, thereby forming the skyrmion lattice. These advances highlight that both electric and magnetic field components of structured evanescent waves can serve as carriers of skyrmionic order, enriching the landscape of topological photonics.

Of course, the methods and mechanisms for generating skyrmions are by no means limited to high-symmetry multi-wave interference. Researchers continue to inject new vitality into this field, developing novel approaches to create various forms of field skyrmions. On one hand, starting from lattice-based designs, concepts such as moiré patterns have been introduced into skyrmion lattice structures [178,180–183]. In trilayer plasmonic systems, for example, SPP interference among layers stacked at controlled twist angles produces a super-moiré skyrmion lattice. Varying the interlayer twist angles enables tuning of the resulting skyrmion bags—multi-skyrmion clusters bounded by a single topological contour—offering a highly adjustable platform for designing Skyrmion lattices with tailored topological charges.

On the other hand, the mechanisms and methods for skyrmion generation are also being continuously renewed. Metasurfaces and meta-structures provide another versatile route for skyrmion generation. One method employs ultra-thin space-coiling meta-structures supporting magnetic localized spoof plasmons (LSP) to create arbitrarily

Figure 13

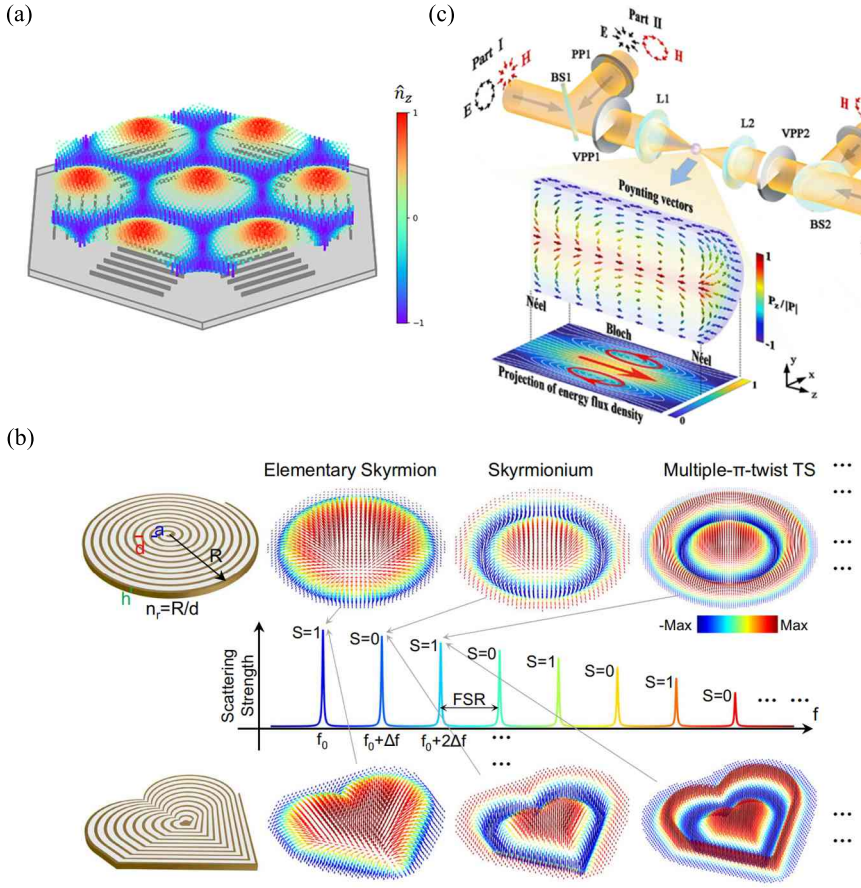

Generation of optical field skyrmions. (a) Generation of optical field skyrmion from excitement of SPPs propagating on a hexagonal array of coupling slits [9]. (b) Generation of arbitrarily shaped skyrmions based on magnetic localized spoof plasmons (LSP). (c) Generation of optical field skyrmions and Poynting vector skyrmions using a 4π focusing system [36]. (b) Reprinted from [35] under a Creative Commons license. (c) Reprinted with permission from Wang *et al.*, Phys. Rev. Lett. **133**, 073802 (2024), Ref. [36]. Copyright 2024 by the American Physical Society.

shaped skyrmions [35] [Fig. 13(b)]. These skyrmions were measured using a 3D scanning platform connected to a vector network analyzer. Their configurations adapt to geometric deformations while preserving their topology. The excitation conditions were flexible, allowing for the use of various electromagnetic sources such as point sources or plane wave sources. In a related approach, C_4-symmetric spiral meta-structures were used to integrate BICs with plasmonic skyrmions, enabling simultaneous electric and magnetic skyrmion formation with high quality factors and polarization-dependent tunability [184], opening avenues for highly sensitive sensing and multifunctional meta-devices.

The coiled topology of optical skyrmions led to the idea of creating them by bending the vector field using tightly focused beams, as shown in Fig. 13(c). A 4π focusing configuration using counter-propagating beams with specific polarization states (e.g., radial/azimuthal polarization pairs) was theoretically proposed to realize both Bloch- and Néel-type optical skyrmions [185]. To realize a Néel-type skyrmion, a pair of counter-propagating incident beams with specific polarization states are required. One pair should be radially polarized, while the other pair should have a phase difference

of π. To realize a Bloch-type skyrmion, the polarization states of the incident beams need to be adjusted such that one pair is azimuthally polarized while the other pair is radially polarized. This approach was further extended to create Poynting vector skyrmions through interference of cylindrical vector vortex beams, enabling dynamic transitions between Néel and Bloch textures and offering control over topological invariants via amplitude modulation [36].

These diverse methods, spanning multi-wave interference phenomena, twistronics, metasurfaces, and beam focusing, collectively provide a rich toolkit for field skyrmion generation, each offering unique advantages for fundamental studies and applications in topological photonics.

4.2. Polarization-Related Skyrmions

4.2.1. Spin Skyrmions

An optical spin skyrmion represents a topological texture constructed from the spin vector distribution of light [186–188]. In optics, spin describes the local circular polarization state—an intrinsic property of the electromagnetic field originating from the rotational motion of the field vectors in a plane perpendicular to the direction of propagation. It should be emphasized that this optical spin is distinct from the electronic spin in magnetic materials: the latter refers to the intrinsic angular momentum of electrons as a quantum-mechanical property, while the former characterizes the polarization state of classical electromagnetic waves.

Mathematically, the optical spin vector is expressed as:

$$\mathbf{s} = \mathbf{s}_E + \mathbf{s}_H = \frac{\epsilon_0}{4\omega}\mathrm{Im}\{\mathbf{E}^* \times \mathbf{E}\} + \frac{\mu_0}{4\omega}\mathrm{Im}\{\mathbf{H}^* \times \mathbf{H}\}, \tag{15}$$

reflecting contributions from both the electric and magnetic field components, denoted as $\mathbf{s}_E$ and $\mathbf{s}_H$ respectively. The electric and magnetic spin components represent rotational behaviors of the electric and magnetic field vector, respectively, which can be discussed separately in spin skyrmion generation [189]. The time-varying electric and magnetic fields are interdependent, as governed by Maxwell's equations, collectively giving rise to the overall SAM of light. Throughout this tutorial, optical "spin" or "SAM" refers to the overall SAM, unless specified otherwise.

Similar to optical field skyrmions, optical spin skyrmions are generated through the interference of surface evanescent waves, primarily using SPPs. Now we discuss the single SPP wave mentioned in Eq. (6), and the magnetic field can be derived as:

$$\begin{aligned}\mathbf{H} &= -\frac{\mathrm{i}}{\omega\mu_0}\nabla\times\mathbf{E} = -\frac{\mathrm{i}}{\omega\mu_0}(\mathrm{i}\mathbf{k}\times\mathbf{E}) \\ &= \frac{1}{\omega\mu_0}\begin{pmatrix} k_\parallel\cos\alpha \\ k_\parallel\sin\alpha \\ -\mathrm{i}\kappa_z\end{pmatrix}\times\begin{pmatrix} \frac{\mathrm{i}\kappa_z\cos\alpha}{k_\parallel} \\ \frac{\mathrm{i}\kappa_z\sin\alpha}{k_\parallel} \\ 1\end{pmatrix} E_0\,\mathrm{e}^{\mathrm{i}\omega t-\mathrm{i}k_\parallel(x\cos\alpha+y\sin\alpha)-\kappa_z z} \\ &= \frac{E_0 k_0^2}{\omega\mu_0 k_\parallel}\begin{pmatrix}\sin\alpha \\ -\cos\alpha \\ 0\end{pmatrix}\mathrm{e}^{\mathrm{i}\omega t-\mathrm{i}k_\parallel(x\cos\alpha+y\sin\alpha)-\kappa_z z}.\end{aligned} \tag{16}$$

Notice that the wavenumber in free space $k_0 = \sqrt{k_\parallel^2 - \kappa_z^2}$.

We begin our analysis with simple two-wave interference [see Eq. (8)], which lays the foundation for understanding more complex interference patterns. Since the magnetic field $\vec{H}$ of each SPP wave has a z-component of 0 from Eq. (16), the magnetic field vector from 2-wave interference only lies in xy-plane, and subsequently the polarization

of magnetic field in yz-plane is fixed on the y-axis. Moreover, from Eq. (8) we can see that because the y-component and the z-component of the electric field from 2-wave interference do not exhibit a phase difference, the direction of electric field in the yz-plane remains fixed. The direction in yz-plane of electric field and magnetic field are both fixed, which indicates that there is no x-component of SAM vector. Consequently, SAM vector only lies in yz-plane, which indicates that its directions cannot be mapped to cover a 2-sphere, and leads to the conclusion there is no optical spin skyrmion texture in the case of 2-wave interference.

Next, we consider the 3-wave interference case of an equilateral triangular texture, and the electric field distribution has already been presented in Eq. (11). For brevity, we set $H_0 = \frac{E_0}{\omega\mu_0}$, $I_0 = \epsilon_0|E_0|^2$, and from Eq. (16), we can compute the corresponding magnetic field:

$$\mathbf{H} = H_0 \mathrm{e}^{\mathrm{i}\omega t - \kappa_z z} \begin{pmatrix} \sqrt{3}\mathrm{i}\sin(\frac{\sqrt{3}}{2}k_\parallel y) \\ \cos(\frac{\sqrt{3}}{2}k_\parallel y) - \mathrm{e}^{-\mathrm{i}\frac{3}{2}k_\parallel x} \\ 0 \end{pmatrix}. \tag{17}$$

From Eq. (15), we can obtain the SAM vector:

$$\mathbf{s} = \frac{I_0 \mathrm{e}^{-2\kappa_z z}}{2\omega} \begin{pmatrix} -\sqrt{3}\frac{\kappa_z}{k_\parallel}\sin(\frac{\sqrt{3}}{2}k_\parallel y)\sin(\frac{3}{2}k_\parallel x) \\ \frac{\kappa_z}{k_\parallel}\left[-2\cos^2(\frac{\sqrt{3}}{2}k_\parallel y) + \cos(\frac{3}{2}k_\parallel x)\cos(\frac{\sqrt{3}}{2}k_\parallel y) + 1\right] \\ \sqrt{3}\left[-\cos(\frac{\sqrt{3}}{2}k_\parallel y) + \cos(\frac{3}{2}k_\parallel x)\right]\sin(\frac{\sqrt{3}}{2}k_\parallel y) \end{pmatrix}. \tag{18}$$

We can obtain the distribution of SAM vector on xy-plane as demonstrated in Eq. (18), with its direction not merely limited in yz-plane, which indicates the possible emergence of topological structure. From the $N = 3$ case in Fig. 14, we can obtain that for 3-wave interference, time-invariant meron distribution of equilateral triangular lattice can be formed.

We study the case of 4 wave interference, as the case mentioned in Section 4.1 with $E_m = E_0$, and we can deduce the electric field distribution:

$$\mathbf{E} = 2E_0 \mathrm{e}^{\mathrm{i}\omega t - \kappa_z z} \begin{pmatrix} \frac{\kappa_z}{k_\parallel}\sin k_\parallel x \\ \frac{\kappa_z}{k_\parallel}\sin k_\parallel y \\ \cos k_\parallel x + \cos k_\parallel y \end{pmatrix}. \tag{19}$$

We can see that there are no spin textures since the electric field at all (x, y, z) has no difference in phase of different directions. The same holds for the magnetic field. Hence, the SAM vector will be 0, which indicates there is no spin texture.

By introducing a topological charge l, we set the complex amplitude in Eq. (6) as $E_m = E_0 \mathrm{e}^{-\mathrm{i}l\alpha_m}$. From above discussion and Eq. (19) we can conclude that there is no optical spin skyrmion emerging for the $l = 0$ case in 4-wave interference. For the 4-wave case with $l = 1$, the corresponding SAM vector distribution is given by:

$$\mathbf{s} = -8\epsilon_0 I_0 \mathrm{e}^{-2\kappa_z z} \begin{pmatrix} \frac{\kappa_z}{k_\parallel}\cos k_\parallel y \sin k_\parallel x \\ \frac{\kappa_z}{k_\parallel}\cos k_\parallel x \sin k_\parallel y \\ \cos k_\parallel y \cos k_\parallel x \end{pmatrix}. \tag{20}$$

From $N = 4$ case in Fig. 14 we can see that a square lattice of merons emerge.

Let us now extend the discussion to the interference of multiple waves with their propagation direction forming a C_N symmetry. When considering N waves, we can define

Figure 14

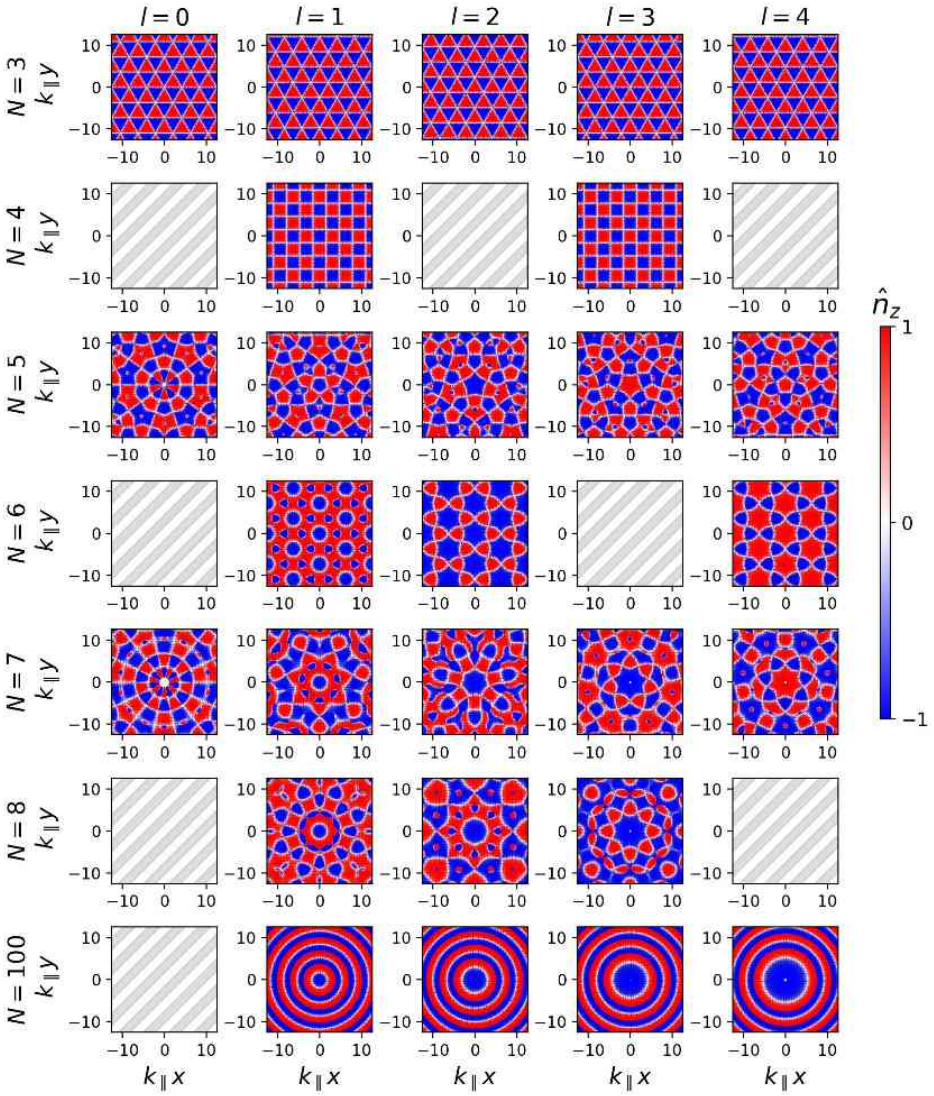

Distribution of normalized SAM vector generated from the interference of N SPP waves of C_N symmetry when $l = 0, 1, 2, 3, 4$. The unit vector $\hat{\mathbf{n}}$ is represented by colors (vertical component $\hat{n}_z$) and black arrows (horizontal component $(\hat{n}_x, \hat{n}_y)$). Notice that, for a uniform $\hat{\mathbf{n}} = 0$ state in which the spin texture vanishes over the entire plane, this uniformity is depicted as blank areas featuring parallel oblique gray stripes.

their propagation angles as $\alpha_m = \frac{2\pi(m-1)}{N}$ and obtain the configurations of skyrmions that follow a well-defined geometrical arrangement. Expressing the coordinates in polar form, $x = \rho\cos\phi$, $y = \rho\sin\phi$, the interfered electric field becomes:

$$\mathbf{E} = \sum_{m=1}^{N} \begin{pmatrix} \frac{\mathrm{i}\kappa_z \cos\alpha_m}{k_\parallel} \\ \frac{\mathrm{i}\kappa_z \sin\alpha_m}{k_\parallel} \\ 1 \end{pmatrix} E_0\, \mathrm{e}^{\mathrm{i}\omega t - \mathrm{i}k_\parallel \rho\cos(\alpha_m - \phi) - \mathrm{i}l\alpha_m - \kappa_z z}. \tag{21}$$

From Fig. 14, we can further conclude that by setting $l = 1$, we can obtain a hexagonal lattice of skyrmions when $N = 6$. And when N is not 3, 4, or 6 which enables periodic lattice texture, quasicrystalline tilings appear with a skyrmion carrying a skyrmion number $N_{sk} \approx 1$ in the center. A detailed conclusion is listed in Table 3.

Table 3. Summary of Optical Spin Skyrmion and Meron Distributions of C_N Symmetry with Different N, and $l = 1$

N	Skyrmion Texture
3	Néel-type merons distributed in an equilateral triangular lattice
4	Néel-type merons distributed in a square lattice
6	Néel-type skyrmions distributed in a hexagonal lattice
Other N	Néel-type skyrmions occupying the center and carrying a skyrmion number $N_{sk} \approx 1$

From Fig. 14, it can be observed that when N is even and $l = n\frac{N}{2}$, no spin texture is present. We now proceed to explain this phenomenon. Without losing generality, only the electric field is discussed for brevity.

When N is even, the electric field is given by:

$$\begin{aligned}
\mathbf{E} &= \sum_{m=1}^{N} \begin{pmatrix} \frac{\mathrm{i}\kappa_z \cos\alpha_m}{k_\parallel} \\ \frac{\mathrm{i}\kappa_z \sin\alpha_m}{k_\parallel} \\ 1 \end{pmatrix} E_0\, \mathrm{e}^{\mathrm{i}\omega t - \mathrm{i}k_\parallel \rho\cos(\alpha_m-\phi) - \mathrm{i}l\alpha_m - \kappa_z z} \\
&= \sum_{m=1}^{\frac{N}{2}} \begin{pmatrix} \frac{\mathrm{i}\kappa_z \cos\alpha_m}{k_\parallel} \\ \frac{\mathrm{i}\kappa_z \sin\alpha_m}{k_\parallel} \\ 1 \end{pmatrix} E_0\, \mathrm{e}^{\mathrm{i}\omega t - \mathrm{i}k_\parallel \rho\cos(\alpha_m-\phi) - \mathrm{i}l\alpha_m - \kappa_z z} \\
&\quad + \sum_{m=1}^{\frac{N}{2}} \begin{pmatrix} \frac{\mathrm{i}\kappa_z \cos\alpha_{m+\frac{N}{2}}}{k_\parallel} \\ \frac{\mathrm{i}\kappa_z \sin\alpha_{m+\frac{N}{2}}}{k_\parallel} \\ 1 \end{pmatrix} E_0\, \mathrm{e}^{\mathrm{i}\omega t - \mathrm{i}k_\parallel \rho\cos\left(\alpha_{m+\frac{N}{2}}-\phi\right) - \mathrm{i}l\alpha_{m+\frac{N}{2}} - \kappa_z z} \\
&= \sum_{m=1}^{\frac{N}{2}} \begin{pmatrix} \frac{\mathrm{i}\kappa_z \cos\alpha_m}{k_\parallel}\left(\mathrm{e}^{-\mathrm{i}k_\parallel \rho\cos(\alpha_m-\phi)} - \mathrm{e}^{\mathrm{i}k_\parallel \rho\cos(\alpha_m-\phi) - \mathrm{i}l\pi}\right) \\ \frac{\mathrm{i}\kappa_z \sin\alpha_m}{k_\parallel}\left(\mathrm{e}^{-\mathrm{i}k_\parallel \rho\cos(\alpha_m-\phi)} - \mathrm{e}^{\mathrm{i}k_\parallel \rho\cos(\alpha_m-\phi) - \mathrm{i}l\pi}\right) \\ \mathrm{e}^{-\mathrm{i}k_\parallel \rho\cos(\alpha_m-\phi)} + \mathrm{e}^{\mathrm{i}k_\parallel \rho\cos(\alpha_m-\phi) - \mathrm{i}l\pi} \end{pmatrix} E_0 \mathrm{e}^{\mathrm{i}\omega t - \kappa_z z - \mathrm{i}l\alpha_m}.
\end{aligned} \tag{22}$$

Note that $l\alpha_m = n\frac{N}{2}\frac{2\pi(m-1)}{N} = n\pi(m-1)$, which implies that $\mathrm{e}^{-\mathrm{i}l\alpha_m} = (-1)^{n(m-1)}$.

Here, we let $l = n\frac{N}{2}$, where $n \in \mathbb{Z}$. When l is even, the electric field becomes:

$$\mathbf{E} = 2E_0 \mathrm{e}^{\mathrm{i}\omega t - \kappa_z z} \sum_{m=1}^{\frac{N}{2}} (-1)^{n(m-1)} \begin{pmatrix} \frac{\kappa_z \cos\alpha_m}{k_\parallel} \sin\left[k_\parallel \rho\cos(\alpha_m - \phi)\right] \\ \frac{\kappa_z \sin\alpha_m}{k_\parallel} \sin\left[k_\parallel \rho\cos(\alpha_m - \phi)\right] \\ \cos\left[k_\parallel \rho\cos(\alpha_m - \phi)\right] \end{pmatrix}. \tag{23}$$

When l is odd, the expression becomes:

$$\mathbf{E} = 2\mathrm{i}E_0 \mathrm{e}^{\mathrm{i}\omega t - \kappa_z z} \sum_{m=1}^{\frac{N}{2}} (-1)^{n(m-1)} \begin{pmatrix} \frac{\kappa_z \cos\alpha_m}{k_\parallel} \cos\left[k_\parallel \rho\cos(\alpha_m - \phi)\right] \\ \frac{\kappa_z \sin\alpha_m}{k_\parallel} \cos\left[k_\parallel \rho\cos(\alpha_m - \phi)\right] \\ -\sin\left[k_\parallel \rho\cos(\alpha_m - \phi)\right] \end{pmatrix}. \tag{24}$$

It can be observed that in both cases, the x-, y-, and z-components of the electric field do not exhibit phase differences. The same applies to the magnetic field. This implies that $\mathbf{E}^* \times \mathbf{E} = 0$ and $\mathbf{H}^* \times \mathbf{H} = 0$. Consequently, we can obtain that $\mathbf{s} = 0$ from Eq. (15).

Then we consider the case $N \to \infty$, which corresponds to the Bessel-type SPP wave.

In the limiting case $N \to \infty$, the summation converts into an integral:

$$\begin{aligned}\mathbf{E} &= \int_0^{2\pi} \begin{pmatrix} \mathrm{i}\frac{\kappa_z}{k_\parallel}\cos\alpha\, \mathrm{e}^{-\mathrm{i}k_\parallel\rho\cos(\alpha-\phi)-\mathrm{i}l\alpha} \\ \mathrm{i}\frac{\kappa_z}{k_\parallel}\sin\alpha\, \mathrm{e}^{-\mathrm{i}k_\parallel\rho\cos(\alpha-\phi)-\mathrm{i}l\alpha} \\ \mathrm{e}^{-\mathrm{i}k_\parallel\rho\cos(\alpha-\phi)-\mathrm{i}l\alpha} \end{pmatrix} E_0\, \mathrm{e}^{\mathrm{i}\omega t-\kappa_z z}\,\mathrm{d}\alpha, \\ \mathbf{H} &= \int_0^{2\pi} \begin{pmatrix} \sin\alpha\, \mathrm{e}^{-\mathrm{i}k_\parallel\rho\cos(\alpha-\phi)-\mathrm{i}l\alpha} \\ -\cos\alpha\, \mathrm{e}^{-\mathrm{i}k_\parallel\rho\cos(\alpha-\phi)-\mathrm{i}l\alpha} \\ 0 \end{pmatrix} H_0\, \mathrm{e}^{\mathrm{i}\omega t-\kappa_z z}\,\mathrm{d}\alpha. \end{aligned} \tag{25}$$

Recalling the definition of the Bessel function:

$$\int_0^{2\pi} \mathrm{e}^{-\mathrm{i}k_\parallel\rho\cos(\alpha-\phi)-\mathrm{i}l\alpha}\,\mathrm{d}\alpha = 2\pi(-\mathrm{i})^l\,\mathrm{e}^{-\mathrm{i}l\phi}J_l(k_\parallel\rho),$$

we obtain:

$$\mathbf{E} = \pi(-\mathrm{i})^l\mathrm{e}^{-\mathrm{i}l\phi}E_0\mathrm{e}^{\mathrm{i}\omega t-\kappa_z z}\begin{pmatrix} \frac{\kappa_z}{k_\parallel}[\mathrm{e}^{-\mathrm{i}\phi}J_{l+1}(k_\parallel\rho)-\mathrm{e}^{\mathrm{i}\phi}J_{l-1}(k_\parallel\rho)] \\ \mathrm{i}\frac{\kappa_z}{k_\parallel}[\mathrm{e}^{-\mathrm{i}\phi}J_{l+1}(k_\parallel\rho)+\mathrm{e}^{\mathrm{i}\phi}J_{l-1}(k_\parallel\rho)] \\ 2J_l(k_\parallel\rho) \end{pmatrix}, \tag{26}$$

and similarly,

$$\mathbf{H} = \pi(-\mathrm{i})^l\mathrm{e}^{-\mathrm{i}l\phi}H_0\mathrm{e}^{\mathrm{i}\omega t-\kappa_z z}\begin{pmatrix} \mathrm{e}^{\mathrm{i}\phi}J_{l-1}(k_\parallel\rho)+\mathrm{e}^{-\mathrm{i}\phi}J_{l+1}(k_\parallel\rho) \\ \mathrm{i}\mathrm{e}^{\mathrm{i}\phi}J_{l-1}(k_\parallel\rho)-\mathrm{i}\mathrm{e}^{-\mathrm{i}\phi}J_{l+1}(k_\parallel\rho) \\ 0 \end{pmatrix}. \tag{27}$$

The corresponding SAM vector is then given by:

$$\mathbf{s} = \frac{1}{4\omega}\mathrm{Im}\left\{\epsilon_0\mathbf{E}^*\times\mathbf{E}+\mu_0\mathbf{H}^*\times\mathbf{H}\right\} = \frac{2l\pi^2\epsilon_0|E_0|^2\mathrm{e}^{-2\kappa_z z}\kappa_z J_l(k_\parallel r)}{\omega k_\parallel^2 r}\begin{pmatrix} J_l(k_\parallel r)\cos\phi \\ -J_l(k_\parallel r)\sin\phi \\ -\frac{2k_0^2}{\kappa_z k_\parallel}J_l'(k_\parallel r) \end{pmatrix}, \tag{28}$$

where $J_l'(x) = \frac{\mathrm{d}J(x)}{\mathrm{d}x}$. This result explicitly indicates that the sign and direction of $\mathbf{s}$ vary radially. We then obtain:

$$\hat{\mathbf{n}} = \frac{J_l(k_\parallel\rho)}{\sqrt{J_l(k_\parallel\rho)^4+4J_l(k_\parallel\rho)^2J_l'(k_\parallel\rho)^2}}\begin{pmatrix} J_l(k_\parallel\rho)\cos\phi \\ -J_l(k_\parallel\rho)\sin\phi \\ -\frac{2k_0^2}{\kappa_z k_\parallel}J_l'(k_\parallel\rho) \end{pmatrix}. \tag{29}$$

Notice the singularity on $x^2+y^2=\rho^2$ that when $J_l(k_\parallel\rho)=0$, we have $\mathbf{s}=0$, and consequently, $\hat{\mathbf{n}} = \frac{\mathbf{s}}{|\mathbf{s}|}$.

Compute the skyrmion number:

$$\begin{aligned} N_{sk} &= \frac{1}{4\pi}\iint\hat{\mathbf{n}}\cdot\left(\frac{\partial\hat{\mathbf{n}}}{\partial x}\times\frac{\partial\hat{\mathbf{n}}}{\partial y}\right)\mathrm{d}x\mathrm{d}y = \frac{1}{4\pi}\iint\hat{\mathbf{n}}\cdot\frac{1}{\rho}\left(\frac{\partial\hat{\mathbf{n}}}{\partial\rho}\times\frac{\partial\hat{\mathbf{n}}}{\partial\phi}\right)\mathrm{d}\rho\mathrm{d}\phi \\ &= \frac{1}{4\pi}\int_0^{2\pi}\mathrm{d}\phi\int\frac{1}{\rho}\begin{vmatrix} \hat{n}_x & \hat{n}_y & \hat{n}_z \\ \frac{\partial\hat{n}_x}{\partial\rho} & \frac{\partial\hat{n}_y}{\partial\rho} & \frac{\partial\hat{n}_z}{\partial\rho} \\ \frac{\partial\hat{n}_x}{\partial\phi} & \frac{\partial\hat{n}_y}{\partial\phi} & \frac{\partial\hat{n}_z}{\partial\phi} \end{vmatrix}\mathrm{d}\rho = \frac{1}{2}\int\frac{\partial\hat{n}_z}{\partial\rho}\mathrm{d}\rho. \end{aligned} \tag{30}$$

When $J_l(k_\parallel \rho) \neq 0$,

$$\hat{n}_z = \frac{-\frac{2k_0^2}{\kappa_z k_\parallel} J_l(k_\parallel \rho) J_l'(k_\parallel \rho)}{\sqrt{J_l(k_\parallel \rho)^4 + \frac{4k_0^4}{\kappa_z^2 k_\parallel^2} J_l(k_\parallel \rho)^2 J_l'(k_\parallel \rho)^2}} = \frac{-\frac{2k_0^2}{\kappa_z k_\parallel} \mathrm{sgn}\{J_l(k_\parallel \rho)\} J_l'(k_\parallel \rho)}{\sqrt{J_l(k_\parallel \rho)^2 + \frac{4k_0^4}{\kappa_z^2 k_\parallel^2} J_l'(k_\parallel \rho)^2}}. \tag{31}$$

Let the non-negative zeros of $J_l(k_\parallel \rho)$ be ρ_m ($m \in \mathbb{Z}_{\geq 0}$), and $l \neq 0$, from Eq. (30) we can obtain:

$$\begin{aligned} N_{sk,m} &= \frac{1}{2} \int_{\rho_m}^{\rho_{m+1}} \frac{\partial \hat{n}_z}{\partial \rho} \mathrm{d}\rho = \lim_{\epsilon \to 0^+} \frac{\hat{n}_z|_{\rho_{m+1}-\epsilon} - \hat{n}_z|_{\rho_m+\epsilon}}{2} \\ &= -\frac{1}{2} \mathrm{sgn}\{J_l(k_\parallel \rho_m + k_\parallel \epsilon)\} \cdot \left[\mathrm{sgn}\{J_l'(k_\parallel \rho_{m+1})\} - \mathrm{sgn}\{J_l'(k_\parallel \rho_m)\}\right] \\ &= \mathrm{sgn}\{J_l(k_\parallel \rho_m + k_\parallel \epsilon)\} \cdot \mathrm{sgn}\{J_l'(k_\parallel \rho_m)\} = 1. \end{aligned} \tag{32}$$

Then we discuss when $l = 0$, the fields take the simpler form:

$$\begin{aligned} \mathbf{E} &= 2\pi E_0 \begin{pmatrix} \frac{\kappa_z}{k_\parallel} \cos\phi J_1(k_\parallel \rho) \\ -\frac{\kappa_z}{k_\parallel} \sin\phi J_1(k_\parallel \rho) \\ J_0(k_\parallel \rho) \end{pmatrix} \mathrm{e}^{\mathrm{i}\omega t - \kappa_z z}, \\ \mathbf{H} &= 2\pi H_0 \, \mathrm{i} J_1(k_\parallel \rho) \begin{pmatrix} \sin\phi \\ -\cos\phi \\ 0 \end{pmatrix} \mathrm{e}^{\mathrm{i}\omega t - \kappa_z z}. \end{aligned} \tag{33}$$

Because the electric and magnetic field components in each direction do not exhibit a relative phase difference, no spin texture is produced in this case.

Hence, it can be concluded that for a Bessel-type SPP wave, as formulated in Eq. (25) with $l \in \mathbb{Z}_{\neq 0}$, an optical spin skyrmion texture with a topological charge of $N_{sk} = 1$ is confined to an annular region bounded by two adjacent non-negative zeros of the governing Bessel function. Conversely, when $l = 0$, no spin texture is present. In Fig. 14, this conclusion is verified by numerical results for $N = 100$, which represents a sufficiently large value of N to approximate the continuum limit.

In the above discussion of the case $N \to \infty$, we can derive a strictly quantitative solution that allows us to explain the underlying physical mechanisms that lead to the formation of the skyrmion texture. The introduction of the term $\mathrm{e}^{-\mathrm{i}l\alpha_m}$ modifies the phase distribution of the optical field, which in turn influences the distribution of SAM and the topological properties of the system. This solution not only provides a clear and rigorous explanation for the formation of the optical spin skyrmion texture but also serves as a reference for understanding the system's behavior when N is a finite integer, as the quantitative solution for $N \to \infty$ offers valuable insights that can be applied to the study of skyrmion textures in finite systems. From the simulated results shown in Fig. 14, it is evident that for finite values of N, the system displays similar qualitative behavior.

In summary, by engineering the interference of N SPP waves with controlled phase differences and propagating direction arranged in accordance to C_N symmetry, Néel-type spin textures can be realized based on optical SAM vector distribution. Adjusting parameters such as wave number, relative phase, and the number of contributing waves allowed for tailored distributions of skyrmions and merons, thereby opening new avenues in the manipulation of optical spin topologies. We can see some conclusions of the case when $l = 1$ for different N in Fig. 14 and Table 3.

The generation of spin skyrmions has been explored through various techniques that involve controlling light–matter interactions [13,189–202], with one approach using

focused vector beams exhibiting spin–orbit coupling to create photonic spin structures that resemble magnetic skyrmions [13,34,190], as shown in Fig. 15(a). Optical spin skyrmion is constructed by introducing spin–orbit coupling in an evanescent optical vortex field [190], described by a Hertz vector potential with a helical phase factor $e^{il\phi}$, where l denotes the topological charge. The transverse and longitudinal components of the resulting electric field generate a spatially varying SAM distribution, forming a topologically non-trivial spin texture. The coupling between the spin and orbital angular momenta causes the spin vectors to rotate continuously from the center to the edge, yielding a Néel-type photonic skyrmion structure. When magneto-optical effects are introduced, the coupling between the electric and magnetic Hertz potentials further modifies the SAM components, resulting in twisted photonic skyrmions whose spatial characteristics are determined by the magnetization orientation of the medium. Optical spin skyrmions carrying OAM can also be generated by exciting SPPs through other distinct methods, as illustrated in Figs. 15(b) and 15(c). One method uses circularly polarized light passing through a sharp slit on a metal surface [191] as shown in Fig. 15(b), where the excited SPPs form twisted plasmonic spin textures predicted by an analytical model to exhibit co-gyrating electric and magnetic fields that induce magnetoelectric effects, with their dynamics captured via ultrafast interferometric time-resolved photoemission electron microscopy providing nanometer spatial and femtosecond temporal resolution. Alternatively, plasmonic metasurfaces that manipulate polarization and OAM provide another platform [192] as shown in Fig. 15(c), where a hexagonal arrangement on a gold film excites SPPs whose interference creates periodic optical lattices, including spin skyrmion lattices formed by aligning the spin vectors in opposite directions through tuning of the incident beam's vortex phase. This metasurface system utilizes electric and magnetic gradient forces alongside spin density forces—the latter being crucial for chirality-based sorting—to manipulate chiral particles, and with an integrated microflow system, it enables the trapping and effective sorting of chiral particles by exploiting their distinct optical force responses. Additionally, recent work has shown that the interference of multiple plasmonic vortices can generate optical multimerons whose skyrmion number changes in response to the incident polarization, providing an experimentally observed example of polarization-dependent topological variation in optical spin textures [203].

Another method involves using phonon polaritons in hexagonal boron nitride (hBN) to generate optical spin skyrmions [193], as shown in Fig. 15(d). Circularly polarized light is directed at a ring-shaped launcher to excite polariton vortex modes in the hBN microcrystals. These polaritons exhibit a phase singularity at the vortex core, indicative of an optical meron spin texture. The spin–orbit interaction of the light induces a skyrmion number of $\pm\frac{1}{2}$ at the core, corresponding to a meron-like structure. The spin texture is visualized using near-field infrared microscopy, which allows the observation of these deeply sub-diffractional polaritonic vortices and their corresponding spin textures. The skyrmion number of the meron spin texture is confirmed through modeling and experimental imaging, with distinct behavior under right-handed and left-handed circularly polarized light, corresponding to positive and negative skyrmion numbers, respectively.

In the context of optical spin skyrmions, an important development was the exploration of polarization textures in free space, which were shown to exhibit skyrmionic structures by constructing optical beams with robust skyrmionic structures in their polarization fields in free space [189], as shown in Fig. 15(e). Their work demonstrated the formation of both Bloch (spiral) and Néel (hedgehog) skyrmion textures in the electric spin vector of tightly focused, nonparaxial beams. These polarization textures were realized using spin–orbit coupling in higher-order Full-Poincaré beams, leading to stable topological configurations in both circularly- and linearly polarized light. The study revealed that

Figure 15

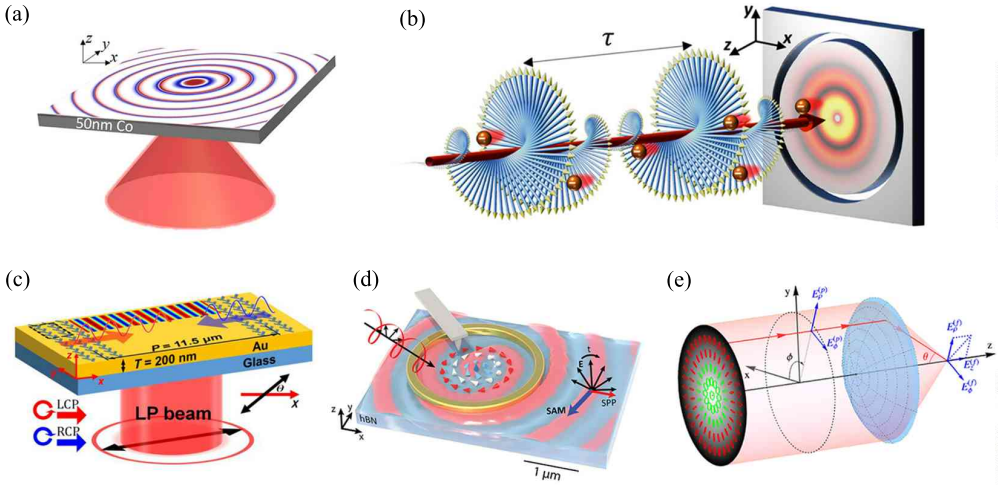

Generation of optical spin skyrmion. (a) Schematic illustration of photonic skyrmion generation in a ferromagnetic medium, demonstrated by the excitation of an SPP on a thin cobalt film using a tightly focused radially polarized beam. (b) Schematic of excitation via plasmonic vortices carrying OAM. (c) Schematic of generation through plasmonic metasurfaces engineered to manipulate polarization and OAM. (d) Generation of optical spin skyrmion by excitation of phonon polaritons in hBN. (e) Schematic illustrating the generation of optical spin skyrmions, where a paraxial beam is focused by an aplanatic system into free space. (a) Reprinted with permission from [190] under a Creative Commons license. (b) Reprinted with permission from Dai *et al.*, Appl. Phys. Rev. **9**, 011420 (2022) [191]. Copyright 2022, AIP Publishing LLC. (c) Reprinted with permission from Tang *et al.*, Phys. Rev. Appl. **19**, 054016 (2023), Ref. [192]. Copyright 2023 by the American Physical Society. (d) Reprinted with permission from Xiong *et al.*, Nano Lett. 2021, **21**, 9256–9261 [193]. Copyright 2021 American Chemical Society. (e) Reprinted with permission from [189]. © 2021 IOP Publishing Ltd.

these structures are topologically protected, even in the absence of nonlinear interactions, making them resilient to perturbations and offering valuable insights for the generation of skyrmions in free space.

4.2.2. Stokes Skyrmions

The polarization state of light is a fundamental property that describes the time-varying pattern of the spatial distribution of electric field. Now we discuss the polarization of electric field in the plane perpendicular to the propagation direction of a paraxial beam of light. This state can be represented in the Poincaré sphere. The distribution of polarization states in space can be mapped onto this sphere, enabling the definition of topological structures such as skyrmions. Although the term "Stokes skyrmions" gained popularity more recently, the foundational ideas were already in place [8,204], enabling applications in structured light and quantum optics [23,27,103]. The concept of Stokes skyrmions in optical fields, defined by Stokes vectors on the Poincaré sphere, traces back over 15 years to the introduction of full Poincaré beams [8,205–210]. Formed by superposing vortex beams with orthogonal polarizations, these beams established spatially variant polarization patterns and inspired the notion of Stokes skyrmions. Their topological stability and robustness were later examined [204].

To analyze the polarization state, we consider two orthogonal spatial modes $u_0(\vec{r})$ and $u_1(\vec{r})$ propagating along the z-axis as left-handed circularly polarized (LCP) and right-handed circularly polarized (RCP) paraxial light beams, respectively. The electric

field on the transverse plane is then given by:

$$|\Psi\rangle = \begin{pmatrix} E_x \\ E_y \end{pmatrix} = u_0(\vec{r})|L\rangle + e^{i\theta_0}u_1(\vec{r})|R\rangle = \frac{1}{\sqrt{2}}\begin{pmatrix} u_0(\vec{r}) + e^{i\theta_0}u_1(\vec{r}) \\ i(u_0(\vec{r}) - e^{i\theta_0}u_1(\vec{r})) \end{pmatrix}, \tag{34}$$

where $|L\rangle = \frac{1}{\sqrt{2}}(1, i)^T$ and $|R\rangle = \frac{1}{\sqrt{2}}(1, -i)^T$ are the circular polarization basis states, and θ_0 denotes a arbitrary difference in phase. Furthermore, we define the linear polarization basis states $|H\rangle = (1, 0)^T$, $|V\rangle = (0, 1)^T$, and the 45°-rotated linear polarization basis states $|A\rangle = \frac{1}{\sqrt{2}}(1, 1)^T$, $|D\rangle = \frac{1}{\sqrt{2}}(1, -1)^T$. The intensity of light with polarization state $|m\rangle$ is denoted as I_m, where $m = H, V, L, R, A, D$.

The Stokes parameters, which fully characterize the polarization state, are defined as:

$$\begin{cases} S_0 = I_L + I_R = |u_0(\vec{r})|^2 + |u_1(\vec{r})|^2, \\ S_1 = I_H - I_V = 2\mathrm{Re}\{e^{-i\theta_0}u_0(\vec{r})u_1^*(\vec{r})\}, \\ S_2 = I_A - I_D = -2\mathrm{Im}\{e^{-i\theta_0}u_0(\vec{r})u_1^*(\vec{r})\}, \\ S_3 = I_R - I_L = |u_1(\vec{r})|^2 - |u_0(\vec{r})|^2. \end{cases} \tag{35}$$

The unit Stokes vector is given by:

$$\mathbf{S} = \frac{1}{S_0}\begin{pmatrix} S_1 \\ S_2 \\ S_3 \end{pmatrix} = \frac{1}{1 + |v(\vec{r})|^2}\begin{pmatrix} 2\,\mathrm{Re}\{v(\vec{r})\} \\ 2\,\mathrm{Im}\{v(\vec{r})\} \\ |v(\vec{r})|^2 - 1 \end{pmatrix}, \tag{36}$$

where $v(\vec{r}) = \frac{e^{i\theta_0}u_1(\vec{r})}{u_0(\vec{r})}$. And here we define the unit vector as $\hat{\mathbf{n}} = \frac{\mathbf{S}}{|\mathbf{S}|} = \mathbf{S}$.

Skyrmionic beams are a class of vector vortex beams that exhibit non-trivial topological properties, characterized by a skyrmion number, which quantifies the spatial variation of polarization (or pseudospin) direction across the beam. A common method for constructing skyrmionic beams is to combine two orthogonal polarization (or pseudospin) states with LG modes of different OAM indices, resulting in a spatially varying polarization pattern that forms a skyrmionic structure [15,211–214].

The general form of an LG mode is given as:

$$\begin{aligned} LG_{p,\ell}(\rho, \phi, z) = &\sqrt{\frac{2p!}{\pi(p + |\ell|)!}}\frac{1}{w(z)}\left(\frac{\rho\sqrt{2}}{w(z)}\right)^{|\ell|}e^{-\frac{\rho^2}{w^2(z)}} \\ &\times L_p^{|\ell|}\left(\frac{2\rho^2}{w^2(z)}\right)e^{i\ell\phi - i\frac{\rho^2}{w^2(z)}\frac{z-z_0}{z_R} - i(2p+|\ell|+1)\arctan\frac{z-z_0}{z_R}}. \end{aligned} \tag{37}$$

We notice that in cylindrical coordinate we have $\vec{r} = (\rho, \phi, z)$ and in Cartesian coordinate we have $\vec{r} = (x, y, z)$, where $x = r\cos\phi, y = r\sin\phi$, and we discuss the case when $u_0(\vec{r}) = LG_{p_0,\ell_0}(\rho, \phi, z)$ and $u_1(\vec{r}) = LG_{p_1,\ell_1}(\rho, \phi, z)$. The beam width $w(z) = w_0\sqrt{1 + \frac{(z-z_0)^2}{z_R^2}}$, as z_0 is the focal position and Rayleigh range $z_R = \frac{\pi w_0^2}{\lambda}$, where λ denotes the wavelength.

On a fixed xy-plane at a specific z, we define:

$$v(\vec{r}) = \frac{e^{i\theta_0}u_1(\vec{r})}{u_0(\vec{r})} = f_z(\rho)e^{i\left[\Delta\ell\phi - (2p_1 + |\ell_1| - 2p_0 - |\ell_0|)\arctan\left(\frac{z-z_0}{z_R}\right)\right]}, \tag{38}$$

where

$$f_z(\rho)=\sqrt{\frac{p_1!(p_0+|\ell_0|)!}{p_0!(p_1+|\ell_1|)!}}\left(\frac{\sqrt{2}\rho}{w(z)}\right)^{|\ell_1|-|\ell_0|}\frac{L_{p_1}^{|\ell_1|}\left(\frac{2\rho^2}{w^2(z)}\right)}{L_{p_0}^{|\ell_0|}\left(\frac{2\rho^2}{w^2(z)}\right)}, \tag{39}$$

is pure real, and $\Delta\ell=\ell_1-\ell_0$. Hence, the Stokes vector can be derived as:

$$\mathbf{S}=\begin{pmatrix}\frac{2f_z(\rho)}{1+f_z^2(\rho)}\cos(\Delta\ell\phi)\\ \frac{2f_z(\rho)}{1+f_z^2(\rho)}\sin(\Delta\ell\phi)\\ \frac{f_z^2(\rho)-1}{1+f_z^2(\rho)}\end{pmatrix}. \tag{40}$$

The skyrmion number is calculated as:

$$\begin{aligned}N_{sk}&=\frac{1}{4\pi}\iint\hat{\mathbf{n}}\cdot\left(\frac{\partial\hat{\mathbf{n}}}{\partial x}\times\frac{\partial\hat{\mathbf{n}}}{\partial y}\right)\mathrm{d}x\mathrm{d}y\\&=\frac{1}{4\pi}\iint\mathbf{S}\cdot\left(\frac{\partial\mathbf{S}}{\partial x}\times\frac{\partial\mathbf{S}}{\partial y}\right)\mathrm{d}x\mathrm{d}y=\frac{1}{4\pi}\iint\mathbf{S}\cdot\left(\frac{\partial\mathbf{S}}{\partial\rho}\times\frac{\partial\mathbf{S}}{\partial\phi}\right)\mathrm{d}\rho\mathrm{d}\phi\\&=\frac{1}{4\pi}\int_0^{2\pi}\int_0^{\infty}\frac{-4\Delta\ell f_z(\rho)f_z'(\rho)}{\rho(1+f_z^2(\rho))^2}\rho\mathrm{d}\rho\mathrm{d}\phi=\lim_{\rho\to\infty}\frac{\Delta\ell}{1+f_z^2(\rho)}-\frac{\Delta\ell}{1+f_z^2(\rho)}\Big|_{\rho=0}.\end{aligned} \tag{41}$$

From Eqs. (37), (38), and (41), we have $N_{sk}=0$ when $(|\ell_1|-|\ell_0|)(2p_1+|\ell_1|-2p_0-|\ell_0|)<0$, and we have $N_{sk}=\mathrm{sgn}\left(|\ell_0|-|\ell_1|\right)\Delta\ell$ when $(|\ell_1|-|\ell_0|)(2p_1+|\ell_1|-2p_0-|\ell_0|)>0$, where sgn is the sign function. When $\rho=0$, we have:

$$\lim_{\rho\to0^+}f_z(\rho)=\lim_{\rho\to0^+}\sqrt{\frac{p_1!(p_0+|\ell_0|)!}{(p_1+|\ell_1|)!p_0!}}\left(\frac{\rho\sqrt{2}}{w(z)}\right)^{|\ell_1|-|\ell_0|}\frac{\binom{p_1+|\ell_1|}{p_1}}{\binom{p_0+|\ell_0|}{p_0}}=\begin{cases}\infty, & |\ell_1|<|\ell_0|\\ 0, & |\ell_1|>|\ell_0|.\end{cases}$$

When $\rho\to\infty$, we have

$$\begin{aligned}\lim_{\rho\to\infty}f_z(\rho)&=\lim_{\rho\to\infty}\sqrt{\frac{p_1!(p_0+|\ell_0|)!}{(p_1+|\ell_1|)!p_0!}}\left(\frac{\rho\sqrt{2}}{w(z)}\right)^{|\ell_1|-|\ell_0|}\frac{(p_1+|\ell_1|)!}{(p_0+|\ell_0|)!}\left(\frac{2\rho^2}{w^2(z)}\right)^{p_1-p_0}\\&=\lim_{\rho\to\infty}\sqrt{\frac{p_1!(p_0+|\ell_0|)!}{(p_1+|\ell_1|)!p_0!}}\left(\frac{\rho\sqrt{2}}{w(z)}\right)^{|\ell_1|-|\ell_0|+2p_1-2p_0}\frac{(p_1+|\ell_1|)!}{(p_0+|\ell_0|)!}\\&=\begin{cases}0, & 2p_1+|\ell_1|<2p_0+|\ell_0|\\ \infty, & 2p_1+|\ell_1|>2p_0+|\ell_0|.\end{cases}\end{aligned}$$

Hence from Eq. (41) we can obtain:

$$N_{sk}=\begin{cases}0, & (|\ell_1|-|\ell_0|)(2p_1+|\ell_1|-2p_0-|\ell_0|)<0\\ \mathrm{sgn}\left(|\ell_0|-|\ell_1|\right)\Delta\ell, & (|\ell_1|-|\ell_0|)(2p_1+|\ell_1|-2p_0-|\ell_0|)>0.\end{cases}$$

In Fig. 16, we set $p_0=1$, $\ell_0=0$, and then modulate p_1 and ℓ_1. For brevity, we discuss cases when $z=0$. As illustrated in Fig. 16, we can discover that when $(|\ell_1|-|\ell_0|)(2p_1+|\ell_1|-2p_0-|\ell_0|)>0$, the orientation of unit vector $\mathbf{S}$ will form a skyrmion of topological charge of $\mathrm{sgn}\left(|\ell_0|-|\ell_1|\right)\Delta\ell_0$. And when $(|\ell_1|-|\ell_0|)(2p_1+|\ell_1|-2p_0-|\ell_0|)<0$, as its orientation on xy-plane is fixed, the topological charge is 0. With the z-coordinate varying, the configuration of $\mathbf{S}_z$ will be proportionally scaled up, and the orientation of every $\mathbf{S}$ on xy-plane will rotate by the same angle as z varies. This phenomena will be discussed later in Section 5.1.1.

Figure 16

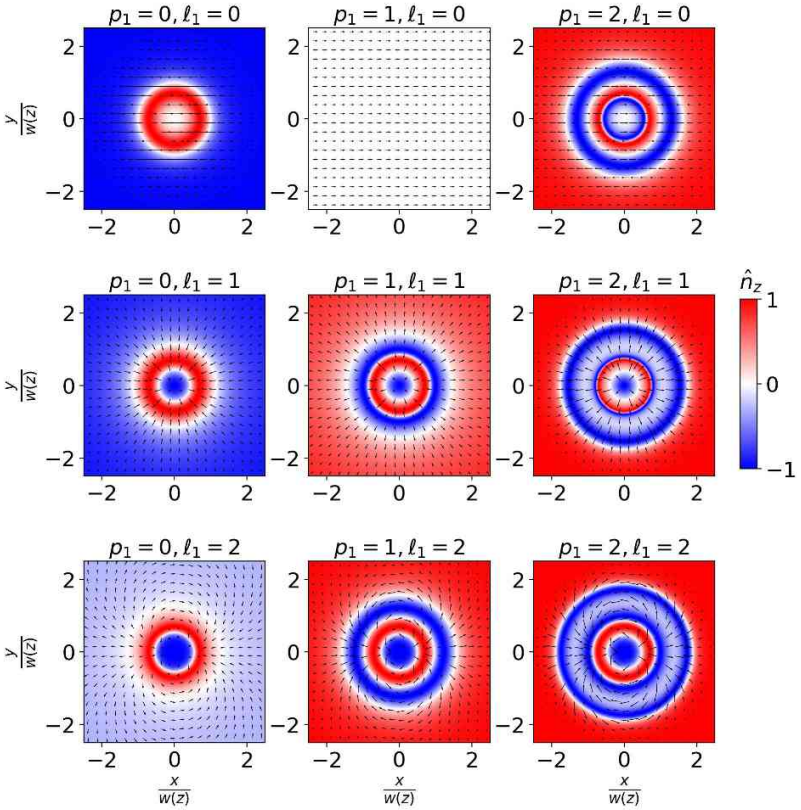

Distribution of normalized Stokes vector on different xy-plane with $p_0 = 1$, $\ell_0 = 0$ for mode $u_1(\vec{r})$. Here we set $z = 0$. The unit vector $\hat{\mathbf{n}}$ is represented by colors (vertical component $\hat{n}_z$) and black arrows (horizontal component $(\hat{n}_x, \hat{n}_y)$). Notice that when $p = 1$ and $\ell = 0$, as shown in the corresponding panel, the Stokes vector is a constant vector on the xy-plane. Therefore, no Stokes skyrmion is present in this case, as discussed in the text.

It is worth emphasizing again that light fields with spatial distributions of polarization states are generally referred to as vector beams. Stokes skyrmions, which arise from specific topological configurations of these polarization states, represent a special class of vector beams with unique topological properties. Moreover, Stokes skyrmions are distinct from Poincaré beams [8], which cover the entire Poincaré sphere but may have a zero skyrmion number. While all integer skyrmion beams are Poincaré beams, not all Poincaré beams exhibit skyrmionic properties—unless they exhibit skyrmionic topology.

The generation of Stokes skyrmions builds on decades of advances in structured light and polarization control. Many researchers have successfully developed various methods for generating optical Stokes skyrmions and have conducted extensive investigations into their unique properties [17,19,170,208,210,215–231]. We now turn to a detailed discussion of these methods.

SLMs provide a highly flexible route to generate reconfigurable Stokes skyrmions and related topological states such as bimerons [170], as illustrated in Fig. 17(a). These structured vector beams are typically created by combining a fundamental Gaussian mode with an orbital-angular-momentum-carrying field, yielding Stokes textures that replicate bimeron configurations—including Néel, Bloch, and anti-types—with topological transitions controlled via helicity and polarization mixing. Higher-order modes

Figure 17

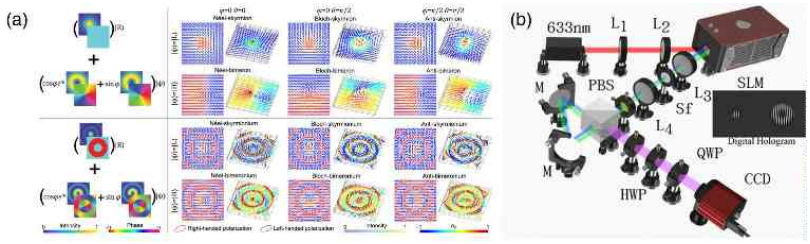

Generation of optical Stokes skyrmions with SLM applied. (a) Generation of optical Stokes skyrmions and bimerons using structured vector beams. (b) Schematic illustration of the experimental setup implemented to generate tunable optical Stokes skyrmions. (a) Reprinted with permission from [170]. © Optica Publishing Group. (b) Reprinted with permission from Shen *et al.*, ACS Photonics 2022, **9**, 296–303 [215]. Copyright 2022 American Chemical Society.

and Bessel beams further allow the formation of complex multi-twist structures. Such skyrmionic beams can also be generated using a digital hologram system implemented on an SLM [215], as shown in Fig. 17(b), where the screen is partitioned to display holograms producing specific spatial modes. The beams are combined in a Sagnac interferometer to form tailored vector profiles, with full Stokes polarimetry used to reconstruct the skyrmionic field and verify its topology.

On-chip platforms and metasurfaces offer subwavelength control and enhanced integration potential for skyrmion generation [19,219,223,227,230]. Silicon photonic chips employing microring resonators with double diffraction gratings [223], illustrated in Figs. 18(a) and 18(b), can synthesize skyrmionic beams via the superposition of orthogonal polarization states carrying different orbital angular momenta. Dielectric metasurfaces combining structural birefringence and geometric phase modulation, for instance, enable optical skyrmions with propagation-invariant topology [230], as shown in Fig. 18(c). By modulating dynamic phase iso-curves, such metasurfaces facilitate arbitrary conversion between co- and cross-polarized components, sustaining stable topological features over long distances. Another study experimentally demonstrated a high-quality photonic skyrmion generator, shown in Fig. 18(d), with subwavelength polarization features by using an elaborately designed metafiber [19]. These compact devices allow control over the skyrmion number through structural design and support scalable on-chip skyrmion generation. In addition, spin–orbit q-plate designs that simultaneously control azimuthal and radial degrees of freedom provide another powerful means of skyrmion generation [228], as shown in Figs. 19(a) and 19(b). Unlike conventional q-plates, such devices incorporate a radial birefringence profile in addition to azimuthal orientation modulation, enabling full Poincaré sphere coverage in the output Stokes vector field. Fabricated via femtosecond laser nanostructuring, these devices transform circularly polarized input into topologically non-trivial polarization textures, with the skyrmion number controlled by both the device parameters and input polarization. Cascading multiple such elements further allows generation of higher-order skyrmions and reconfigurable multiskyrmion lattices. A accompanying theoretical framework based on unitary transformations offers a universal description of such structured birefringent devices [221], linking practical realizations to a rigorous model of polarization topology.

Tightly focused beams constitute another important method for constructing Stokes skyrmions [17], as shown in Fig. 19(c). By tailoring the phase and polarization of an azimuthally polarized vortex beam—comprising two circular polarization components

Figure 18

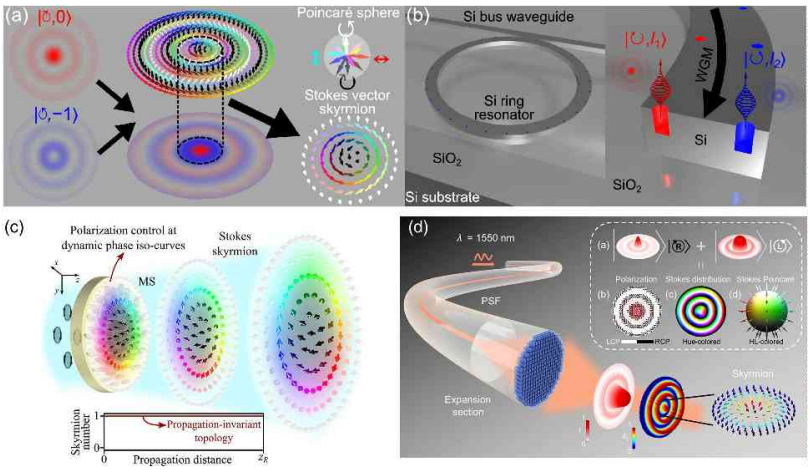

On-chip and metasurface generation of optical skyrmions. (a) Schematic showing the generation mechanism of optical skyrmion beams via the superposition of two modes with orthogonal polarization and different OAMs, creating a spatially varying polarization field [223]. (b) Diagram of an optical skyrmion beam generator based on a silicon ring resonator with double angular diffraction gratings to control polarization and OAM [223]. (c) Conceptual design of a metasurface that generates propagation-invariant Stokes skyrmions [230]. (d) Metafiber-based optical skyrmion generator. The scheme illustrates the formation process of skyrmions through the metafiber, while the inset demonstrates the detailed Skyrmion composition, polarization, and Stokes parameter characteristics [19]. (a) and (b) Reprinted with permission from [223]. © Optica Publishing Group. (c) and (d) Reprinted from [19,230] under a Creative Commons license.

with opposite orbital angular momenta—the symmetry of the field can be broken, allowing radial superposition of polarization states that cover the Poincaré sphere. Introducing a spiral phase to such a beam and adjusting the incident wavevectors enable the formation of customized skyrmion arrays in the focal plane. This approach leverages the natural curvature of the focused vector field to realize skyrmionic textures without complex external interferometry or resonant structures.

All previously discussed skyrmions are generated through superposition of vortex beams, but skyrmions can also be inherent properties of certain optical vortices. The Gauss–Stokes (GS) skyrmion exemplifies this class, emerging intrinsically around the phase singularity of optical vortices without requiring superposition of structured beams or spatial mode engineering [232]. GS skyrmions originate from the axial field governed by Gauss's law. This axial component conceals the vortex phase singularity and creates a polarization singularity with undefined orientation, surrounded by a topologically protected skyrmionic texture spanning the full transverse–axial polarization sphere, as shown in Fig. 19(d). Inherently linked to vortex structure and electromagnetic constraints, GS skyrmions assign a new topological identity to optical phase singularities, bridging the conceptual domains of phase, polarization, and topology—an insight that opens promising avenues for further studies and applications.

4.3. New Insights into Skyrmions

4.3.1. Spatiotemporal Skyrmions

Spatiotemporal skyrmions, also called space-time skyrmions, are skyrmionic textures across both spatial and temporal dimensions [233–235]. Unlike monochromatic optical

Figure 19

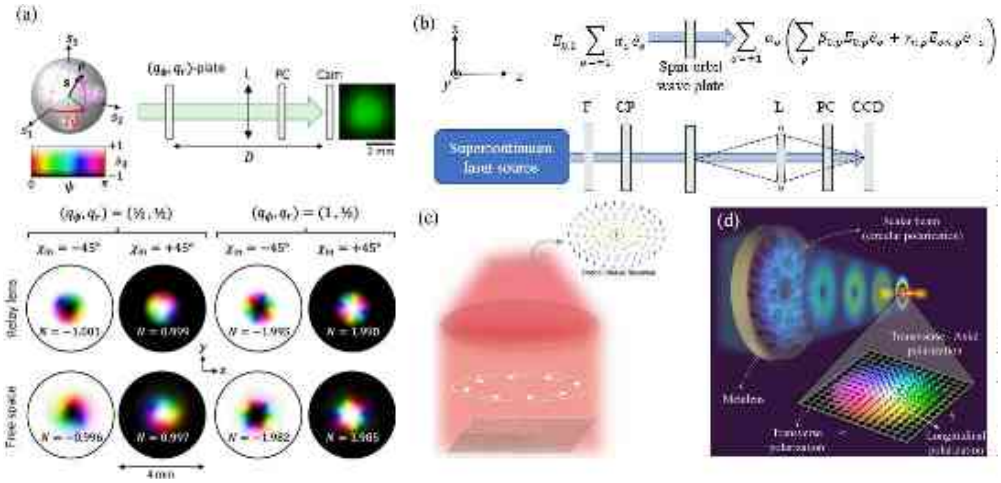

(a) Experimental implementation of Stokes skyrmions using a modified q-plate design [228]. (b) Operating principle of a spin–orbit skyrmionic wave plate of integer order n, which generates superpositions of circularly polarized LG modes. The weighting coefficients α, β, and γ control the superposition, and the corresponding experimental setup is used for full Stokes polarimetric analysis of the resulting modal plates [221]. (c) Generation of Stokes skyrmion through the precise control of the phase and polarization of tightly focused optical beams [17]. (d) An observable GS skyrmion emerges from a vortex singularity when the host scalar beam is focused, structuring its transverse-axial polarization [232]. (a) Reprinted with permission from Hakobyan *et al.*, Phys. Rev. Lett. **134**, 083802 (2025), Ref. [228]. Copyright 2025 by the American Physical Society. (c) Reprinted with permission from Ma *et al.*, Laser Photonics Rev. **19**, 2401113 [17]. Copyright Wiley-VCH Verlag GmbH & Co. KGaA. Reproduced with permission. (d) Reprinted with permission from Mata-Cervera *et al.*, Phys. Rev. Lett. **135**, 033805 (2025), Ref. [232]. Copyright 2025 by the American Physical Society.

skyrmions discussed in Sections 4.1 and 4.2, spatiotemporal skyrmions encompass distributions in frequency domains, manifesting as wave packets that evolve simultaneously in space and time [12,26,234–237]. Their combined spatiotemporal nature makes them particularly significant for advancing optical and photonic systems. Currently, spatiotemporal skyrmions primarily exist as field textures in toroidal light pulses (TLPs).

A toroid has the form of a ring with a central hole, much like a doughnut. There is a notable structural connection between a toroid and a skyrmion: the tangential direction around the toroidal surface corresponds to a Néel-type skyrmion configuration. In physics, the concept of toroidal moments was first introduced in particle physics [238] and has recently garnered significant attention in electromagnetic scattering studies, particularly in the context of anapoles [239]. Anapoles exhibit distinctive near-field patterns with toroidal configurations, characterized by closed vortex-like distributions around a virtual toroid, suggesting promising avenues for exploring skyrmions. For example, a unique anapole probe, which is composed of nanosphere with Ag-core and Si-shell, can function as a pure magnetic dipole without electric response, enabling direct measurement of magnetic-field-driven spin skyrmions and merons [240].

However, the distributions of anapoles exist exclusively within the near-field region at the anapole eigenfrequency. In the near-field, Fourier-transformed evanescent wave

Figure 20

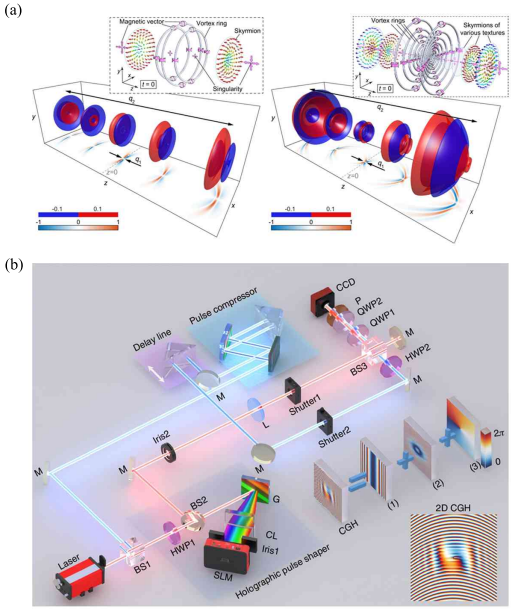

Generation of spatiotemporal skyrmions. (a) Generation of spatiotemporal skyrmion from supertoroidal light pulses. (b) Schematic of experimental setup to construct vectorial spatiotemporal skyrmion wavepackets. (a) Reprinted from [12] under a Creative Commons license. (b) Reprinted from [234] under aCreative Commons license.

components yield momentum vectors $\vec{k}$ with magnitudes exceeding those corresponding to free-space frequencies, preventing far-field propagation. Here, we provide a phenomenological description of toroidal construction in free space. To achieve propagating toroidal modes, we can substitute the evanescent wave modes in the intrinsic field with higher frequencies ω corresponding to increased $\vec{k}$. This substitution results in a toroidal structure comprising multiple frequencies, manifesting as a spatiotemporal wave packet known as a TLP, as illustrated in Fig. 20(a). Furthermore, polarization control enables the transformation between electric and magnetic field skyrmions of TLPs [12].

The experimental generation of TLPs in both the optical and terahertz ranges has been achieved using specially designed nanostructured metasurfaces [26]. In the optical regime, a linear-to-radial polarization converter is employed, followed by a metasurface that scatters conventional laser pulses into few-cycle optical TLPs. These TLPs are generated from femtosecond (<10 fs) linearly polarized laser pulses. The metasurface comprises concentric gold rings with radially varying widths, effectively forming a grating with a continuously varying period when viewed radially. This design enables stronger deflection of higher-frequency components, resulting in larger k values and establishing the desired spatiotemporal coupling characteristic of TLPs. For terahertz TLP generation, the approach utilizes optical rectification of femtosecond near-infrared pulses (50 fs) on a cylindrically symmetric Pancharatnam–Berry phase plasmonic metasurface. This metasurface features three-fold rotationally symmetric gold meta-atoms which can induce spatiotemporal coupling of TLPs [241]. Arranged with their principal axes rotating 120° around the center, this geometric configuration also enables polarization conversion, which eventually allows for the generation of single-cycle terahertz TLPs. The unique metasurfaces enable efficient conversion of the pump pulses into TLPs by leveraging plasmonic resonance and nonlinear effects, paving the way

for future investigations of TLPs [235,242–246], particularly involving anapoles and skyrmions. TLPs also show novel effect, which is worthy of study, such as simultaneous spatiotemporal superoscillations [246].

The spatiotemporal skyrmions discussed above are field-based. Similarly, Stokes parameters can likewise form skyrmionic configurations in the spatiotemporal domain, conceptually analogous to the spatially defined Stokes skyrmions previously introduced—yet here involving the manipulation of polarization in both space and time [234,247]. A novel approach for generating such spatiotemporal skyrmions has been developed via coherent superposition of spatiotemporal optical vortices (STOVs) [234], which have attracted significant research interest due to their ability to carry transverse OAM and exhibit strong spatiotemporal coupling [145–147,248].

As illustrated in Fig. 20(b), experimental realization involves spatiotemporal Fourier transformation of polychromatic Bessel–Gaussian beams using gratings and lenses, followed by SLMs for precise polarization shaping in the spatiotemporal domain. Superposition of spatiotemporal Gaussian and vortex modes yields stable skyrmionic textures, which demonstrate notable robustness against dispersion and diffraction. Their polarization distribution and evolution have been confirmed through temporally resolved interferometric measurements.

These advances in the generation and control of spatiotemporal skyrmions open new prospects for ultrafast photonics and information processing, with potential applications in optical computing, communications, and quantum information technologies [249]. The capability to engineer optical topology across both space and time promises to transform strategies for information encoding and transmission in next-generation optical systems.

4.3.2. Momentum-Space Skyrmions

Momentum space, where the wavevector $\vec{k}$—the momentum of light—serves as the coordinate, has brought new vitality to the field of optical skyrmions. Momentum-space skyrmions arise from wavevector-dependent polarization textures in photonic systems [25,37,163,250,251]. These textures comprise well-defined polarization states from the momentum-space plane-wave components $(\vec{k}, \omega)$ of light, with ω denoting the frequency.

The primary platforms for realizing such skyrmions are photonic crystals (PhCs) and other periodic dielectric structures. These structures have optical bands in momentum space, where each point on optical bands corresponds to an optical eigenmode. When these eigenmodes are leaky and radiate into the far field of free space, they usually form plane waves with well-defined polarization states. By projecting the polarizations of optical eigenmodes onto momentum space, we can obtain distinct momentum-space intrinsic polarization fields [150–152]. Protected by structural symmetries such as mirror or rotational symmetry, these fields often form vortex configurations with topological singularities, including BIC. The winding of polarization in the Brillouin zone can facilitate the formation of optical skyrmions. However, symmetry protection often restricts the polarization to linear or nearly linear states, thereby excluding circularly polarized points necessary for Stokes-type momentum-space skyrmion formation. A key mechanism for generating intrinsic momentum-space skyrmions is thus to reduce or break these symmetries [252–256]. Symmetry breaking introduces diverse polarization states, including circular polarization, into the vortex structure, effectively enabling a “dimensional expansion” of the vortex and making it possible to construct intrinsic momentum-space skyrmions [163,257].

In addition to intrinsic skyrmions in periodic systems, another type of momentum-space skyrmion emerges from the polarization textures of the plane-wave components $(\vec{k}, \omega)$ in free-space beams. Constructing such skyrmions is relatively straightforward, as it involves tailoring the polarization of the momentum-space components of a free-space field. One may directly engineer the momentum-space polarization of free-space beam. A natural setting for direct manipulation is provided by periodic optical structures, which inherently offer momentum-space resonance properties and thereby enable precise control over polarization textures [25,37,157]. Alternatively, another indirect approach employs mechanisms of Fourier optics using lens and diffraction gratings to spatially separate momentum and frequency components, effectively mapping momentum-space elements into real space for manipulation [258,259].

Intrinsic skyrmionic textures in momentum space can be theoretically realized using a PhC slab patterned with a symmetry-broken honeycomb or Kagome lattice of air holes [163,250]. Breaking the inversion symmetry opens a band gap at the Dirac cones located at the corners of the Brillouin zone, resulting in skyrmionic textures near the K and K' points [163,250], as illustrated in Fig. 21(a). These works unlock novel connections between skyrmionic topology and momentum-space topology. However, these textures are fixed and not tunable once the sample is fabricated. In contrast, an electrically tunable liquid crystal microcavity (LCMC) device provides a dynamically reconfigurable platform for eigenmode-based skyrmion generation [255,257], shown in Fig. 21(b). The cavity consists of a nematic LC layer with uniaxial birefringence, embedded between two distributed Bragg reflectors resembling 1D PhCs. The strong birefringence breaks symmetry and induces spin–orbit coupling within the cavity, generating merons accompanied by C-points and diabolical points. The LCMC device allows electrical tuning of the meron textures, offering new opportunities for momentum-space photonics and spinoptronic applications. Notably, this work presents a platform for creating Möbius strips, with potential for extension to a wider range of topological textures.

Besides the intrinsic momentum-space skyrmions, the momentum-space topological manipulation of light via periodic photonic structures provides a highly promising platform for realizing skyrmionic topologies and advancing practical optical applications. A theoretical work demonstrated that the intrinsic momentum-space meron spin texture can be imprinted onto momentum-space profile of light via resonances [25]. This work paves the way for the direct generation of skyrmions in momentum space. Another distinctive experiment demonstrates that the meron spin textures in momentum space of beams can be generated by BICs in PhC slabs [37], as illustrated in Figs. 22(a) and 22(b). These BICs are eigen-polarization vortex singularities of the optical modes in momentum space. Through resonance between circularly polarized incident light and optical modes, the polarization vortex topology of BICs is transformed into a momentum-space Stokes meron topology in the transmitted light. The generation of merons can be controlled by switching the circular polarization of the incident light and the properties of the BICs, allowing for switchable polarity and vorticity. By leveraging BICs and the dispersion of photonic bands, merons can be generated across multiple wavelengths while maintaining robust skyrmion numbers. This compact approach to engineering momentum-space topology requires only a simple periodic structure and avoids complex alignment procedures. These advantages underscore its strong potential for applications in optical sensing, metrology, communications, computing, and other advanced information processing systems based on skyrmions. The study reveals a novel mechanism for topological transformation in momentum space, further elucidating the intricate relationship between vortices and skyrmions discussed in Section 3.2.2. Moreover, the potential of BICs to generate diverse topological textures in

Figure 21

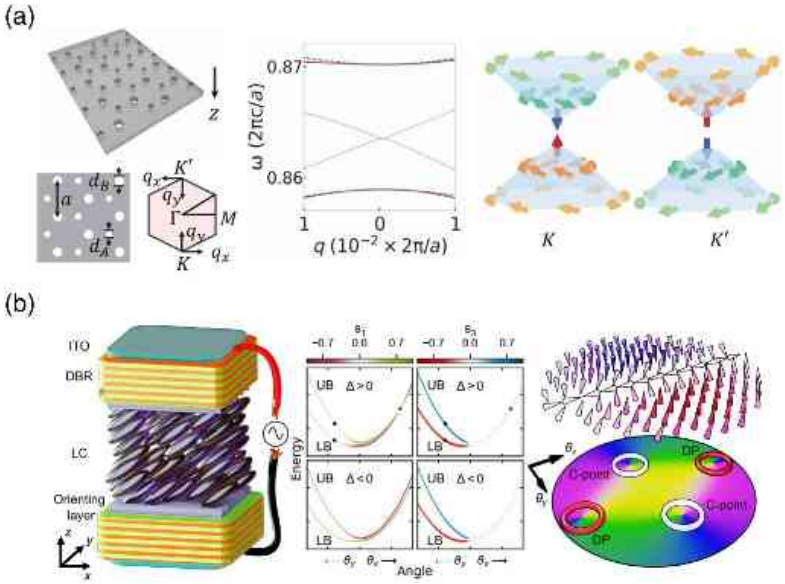

Intrinsic momentum-space merons in periodic optical structures. (a) Momentum-space merons theoretically realized via a symmetry-broken honeycomb PhC slab [163]. (b) Tunable liquid crystal microcavity device associated momentum-space polarization singularities and textures [257]. (a) Reprinted with permission from Guo *et al.*, Phys. Rev. Lett. **124**, 106103 (2020), Ref. [163]. Copyright 2020 by the American Physical Society. (b) Reprinted from [257] under a Creative Commons license.

multidimensions, such as merons, skyrmions, hopfions, and Möbius strips, considerably enriches our understanding of topological photonic phenomena and opens new pathways for advanced optical technologies.

Fourier transform projecting momentum space of beams onto real space is a significant method, which enables precise polarization manipulation for momentum-space skyrmion generations [249,259–261]. This transformation can be implemented using simple optical elements such as lenses or chirped Bragg gratings. In a notable work, researchers engineered polarization textures on a curved 2D spectral surface embedded as a 2D manifold within the 3D momentum-energy space [259]. This was achieved through a spatiotemporal modulation strategy that maps the meron spin texture onto the curved spectral surface via a birefringent metasurface [Fig. 22(c)], resulting in a space-time wave packet. The resulting space-time meron propagates with a tunable group velocity and exhibits distinctive refractive properties. While this method may be influenced by alignment precision, this method exhibits remarkable potential for versatile tuning of momentum-space merons, promising for advanced applications in optical communications and sensing.

4.3.3. Optical Hopfions

Optical skyrmions are 2D topological quasiparticles characterized by non-trivial polarization textures mapped onto a 2D plane. Optical hopfions extend this concept to 3D, forming particle-like structures through a Hopf fibration, where skyrmion-like textures are twisted and linked in 3D space. Mathematically, hopfions can be viewed as "twisted skyrmion tubes" closed into a loop or knot.

Hopfions are characterized by a 3D mapping from real space to the S^3, described by the Hopf fibration ($S^3 \rightarrow S^2$), where the preimages of points on S^2 form linked loops in

Figure 22

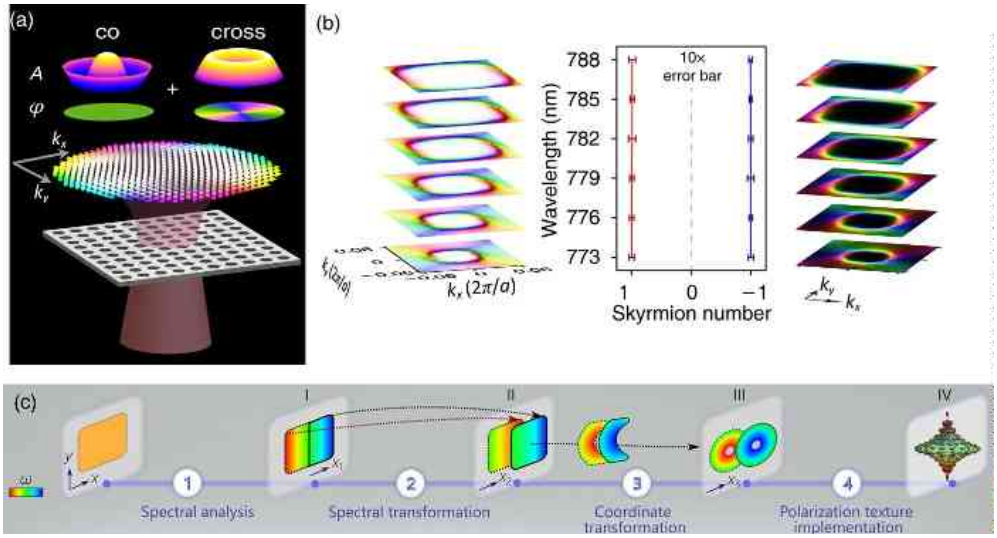

Meron spin textures in momentum space of beams. (a) Merons can be directly generated in momentum space by BIC-related resonance via circularly polarized incidence [37]. (b) Robust meron generation across wavelengths. (c) Merons indirectly generated in momentum-energy space of beams by Fourier transform and polarization engineering via a birefringent metasurface [259]. (a) and (b) Reprinted with permission from Rao *et al.*, Phys. Rev. Lett. **135**, 026203 (2025), Ref. [37]. Copyright 2025 by the American Physical Society. (c) Reprinted from [259] under a Creative Commons license.

real space. The Hopf index N_H quantifies this linking and is computed by integrating the hopfion number density Σ, given by:

$$\Sigma = \frac{1}{16\pi^2}\nabla\gamma \cdot (\nabla \cos\beta \times \nabla\alpha), \tag{42}$$

where α (azimuthal angle of S^2) and β (polar angle of S^2) describe the 2D polarization texture (mapping to S^2), analogous to the skyrmion's unit vector $\hat{\mathbf{n}} = (\sin\beta\cos\alpha, \sin\beta\sin\alpha, \cos\beta)$, and γ (phase angle) introduces an additional degree of freedom, extending the mapping to S^3.

Hopfions generalize skyrmions to 3D. For skyrmion, it arise from a 2D mapping (e.g., polarization states on a Poincaré sphere), with their skyrmion number determined by the Jacobian of (α, β).

The Hopfion density Σ characterizes the 3D topological structure of the field. When γ is trivial, this 3D configuration continuously reduces to a 2D skyrmion, whose skyrmion number is expressed as:

$$N_{sk} = -\frac{1}{4\pi}\iint (\nabla \cos\beta \times \nabla\alpha)_z \mathrm{d}x\mathrm{d}y. \tag{43}$$

For hopfions, it incorporates an additional twist encoded in γ that leads to their characteristic linked ring structures and a non-zero Hopf index N_H.

Optical hopfions can be constructed by complex light field engineering, where scalar fields $E_R(r)$ and $E_L(r)$ represent right- and left-circularly polarized light:

$$(\mathrm{Re}\{E_R\})^2 + (\mathrm{Im}\{E_R\})^2 + (\mathrm{Re}\{E_L\})^2 + (\mathrm{Im}\{E_L\})^2 = I. \tag{44}$$

These fields are expressed as:

$$E_L = \sqrt{I}\sin\frac{\beta}{2}e^{i\frac{\gamma+\alpha}{2}}, \quad E_R = \sqrt{I}\cos\frac{\beta}{2}e^{i\frac{\gamma-\alpha}{2}}, \tag{45}$$

where $I = |E_L|^2 + |E_R|^2$. And here we define Φ_L, Φ_R to be the phase of E_L, E_R respectively. We can obtain the relationship that $\cos\beta = \cos^2\frac{\beta}{2} - \sin^2\frac{\beta}{2} = \frac{|E_R|^2-|E_L|^2}{|E_R|^2+|E_L|^2}$, $\gamma = \Phi_L + \Phi_R$, $\alpha = \Phi_L - \Phi_R$.

Optical Stokes hopfions can be produced by superposing orthogonally polarized LG modes:

$$E_H(\rho, \phi, z) = E_L|L\rangle + E_R|R\rangle, \tag{46}$$

where the LG modes have been defined in Eq. (37), and we set $z_0 = 0$ for brevity.

We study the case when E_L and E_R in Eq. (46) are two LG monomodes, respectively:

$$E_H(\rho, \phi, z) = E_L|L\rangle + E_R|R\rangle = LG_{p_1,\ell_1}|L\rangle + LG_{p_2,\ell_2}|R\rangle. \tag{47}$$

From Eqs. (45) and (47), along with parameters defined after Eq. (45), we can obtain:

$$\begin{cases} \alpha = \Phi_L - \Phi_R = (\ell_1 - \ell_2)\phi + (2p_2 + |\ell_2| - 2p_1 - |\ell_1|)\arctan\frac{z}{z_0} \\ \cos\beta = \frac{|E_R|^2-|E_L|^2}{|E_R|^2+|E_L|^2} = \frac{\frac{2p_2!}{(p_2+|\ell_2|)!}\xi^{2|\ell_2|}L_{p_2}^{|\ell_2|}(\xi^2)^2 - \frac{2p_1!}{(p_1+|\ell_1|)!}\xi^{2|\ell_1|}L_{p_1}^{|\ell_1|}(\xi^2)^2}{\frac{2p_2!}{(p_2+|\ell_2|)!}\xi^{2|\ell_2|}L_{p_2}^{|\ell_2|}(\xi^2)^2 + \frac{2p_1!}{(p_1+|\ell_1|)!}\xi^{2|\ell_1|}L_{p_1}^{|\ell_1|}(\xi^2)^2} \end{cases}. \tag{48}$$

We study the isopolarization contour line in R^3. This line has a constant direction for the unit vector $\mathbf{S}$. Our aim is to see if a closed loop of this kind can form a hopfion structure. Equation (48) shows a relation for specific α and β values. For a given ϕ we find a certain z. This z equals $z_0 \tan\frac{\alpha-(\ell_1-\ell_2)\phi}{2p_2+|\ell_2|-2p_1-|\ell_1|}$. A fixed $\cos\beta$ value lets us find a specific ξ. This ξ indicates a corresponding ρ. Here ρ is $\frac{\sqrt{2}}{2}\xi w(z)$. Thus, a contour line forms in the 3D space. The domain for ϕ is $[0, 2\pi)$. This determines that the range of z is $(-\infty, \infty)$. Therefore, the contour line does not form a loop. We conclude that an optical hopfion structure cannot be formed. It cannot be made merely by two LG monomode lights of left and right circular polarization.

Next, we set the LCP component $E_L = \sum_{p=0}^{\ell} C_p LG_{p,0}$, and $E_R = LG_{0,\ell}$ as a monomode, which indicates that the RCP component is a superposition of LG modes:

$$E_H(\rho, \phi, z) = \sum_{p=0}^{\ell} C_p LG_{p,0}|L\rangle + LG_{0,\ell}|R\rangle. \tag{49}$$

Here we set $\{C_p | C_p \in \mathbb{R}, \forall p = 0, 1, 2, \cdots, \ell\}$, and we consequently prove that a ℓ-order hopfion of arbitrary $\ell \in \mathbb{Z}$ can be constructed.

Recall that $\tan\frac{\beta}{2} = \chi$, $\cos\beta = \frac{1-\chi^2}{1+\chi^2}$, $\xi = \frac{\sqrt{2}\rho}{w(z)}$, $\psi = \tan^{-1}\frac{z}{z_R}$. Here we define three complex ratios, Ψ_α, Ψ_γ, and Ψ_L, each characterized by a common absolute value $\chi = \frac{|E_L|}{|E_R|}$, representing the magnitude ratio between the LCP and RCP field components. $\Psi_\alpha = \frac{E_L}{E_R} = \chi e^{i\alpha}$ characterizes the relative phase between the left- and right-circularly polarized components, defining the azimuthal parameter α on the Poincaré sphere. $\Psi_\gamma = \frac{E_L}{E_R^*} = \chi e^{i\gamma}$ describes the correlation between E_L and the complex conjugate of E_R, representing the global phase γ. Finally, $\Psi_L = \frac{E_L}{|E_R|} = \chi e^{i\Phi_L}$ isolates the intrinsic phase of the left-handed component E_L, which is essential for evaluating the phase

circulation associated with the hopfion topology. Consequently, we have:

$$\begin{cases} \Psi_\alpha = \dfrac{\sum_{p=0}^{\ell} C_p LG_{p,0}}{LG_{0,\ell}} = \dfrac{\sqrt{|\ell|!}\sum_{p=0}^{\ell} C_p L_p^0(\xi^2)\mathrm{e}^{\mathrm{i}(|\ell|-2p)\psi-\mathrm{i}\ell\phi}}{\xi^{|\ell|}} = \chi\mathrm{e}^{\mathrm{i}\alpha} \\ \Psi_\gamma = \dfrac{\sum_{p=0}^{\ell} C_p LG_{p,0}}{LG_{0,\ell}^*} = \dfrac{\sqrt{|\ell|!}\sum_{p=0}^{\ell} C_p L_p^0(\xi^2)\mathrm{e}^{-\mathrm{i}(|\ell|+2p)\psi+\mathrm{i}\ell\phi}}{\xi^{|\ell|}} = \chi\mathrm{e}^{\mathrm{i}\gamma}\cdot \\ \Psi_L = \dfrac{\sum_{p=0}^{\ell} C_p LG_{p,0}}{|LG_{0,\ell}|} = \dfrac{\sqrt{|\ell|!}\sum_{p=0}^{\ell} C_p L_p^0(\xi^2)\mathrm{e}^{-2\mathrm{i}p\psi}}{\xi^{|\ell|}} = \chi\mathrm{e}^{\mathrm{i}\Phi_L} \end{cases} \tag{50}$$

We rewrite Ψ_L into

$$\Psi_L = \frac{\sqrt{|\ell|!}\sum_{p=0}^{\ell} C_p L_p^0(\xi^2)\mathrm{e}^{-2\mathrm{i}p\psi}}{\xi^{|\ell|}} = \sqrt{|\ell|!}\sum_{p=0}^{\ell} A_p(\psi)\xi^{2p-|\ell|}, \tag{51}$$

where we define $A_p(\psi)$ as:

$$A_p(\psi) = \frac{(-1)^p}{(p!)^2}\sum_{m=p}^{\ell}\frac{C_m m!}{(m-p)!}\mathrm{e}^{-2\mathrm{i}m\psi}. \tag{52}$$

We have $A_p(0) = \frac{(-1)^p}{(p!)^2}\sum_{m=p}^{\ell}\frac{C_m m!}{(m-p)!}$, and when $z\to\pm\infty$:

$$\lim_{z\to\pm\infty} A_p(\psi) = A_p\left(\pm\frac{\pi}{2}\right) = \frac{(-1)^p}{(p!)^2}\sum_{m=p}^{\ell}\frac{C_m m!}{(m-p)!}(-1)^m. \tag{53}$$

We carefully modulate $\{C_p\}$ so that for each ξ, when z varies from $-\infty$ to ∞, Φ_L goes from $-\pi$ to π, which indicates $\mathrm{e}^{\mathrm{i}\Phi_L}$ undergoes a counterclockwise circulation of $2n_p\pi$ from -1, which indicates that $\int_{\psi=-\frac{\pi}{2}}^{\psi=\frac{\pi}{2}}\mathrm{d}\Phi_L = 2n_p\pi$, and this will be applied in Eq. (55).

We compute hopfion number density:

$$\begin{aligned} \Sigma &= \frac{1}{16\pi^2}\nabla\gamma\cdot(\nabla\cos\beta\times\nabla\alpha) = \frac{1}{16\pi^2}\begin{vmatrix} \frac{\partial\gamma}{\partial\rho} & \frac{1}{\rho}\frac{\partial\gamma}{\partial\phi} & \frac{\partial\gamma}{\partial z} \\ \frac{\partial\cos\beta}{\partial\rho} & \frac{1}{\rho}\frac{\partial\cos\beta}{\partial\phi} & \frac{\partial\cos\beta}{\partial z} \\ \frac{\partial\alpha}{\partial\rho} & \frac{1}{\rho}\frac{\partial\alpha}{\partial\phi} & \frac{\partial\alpha}{\partial z} \end{vmatrix} \\ &= \frac{-\ell}{16\pi^2\rho}\left(\frac{\partial\cos\beta}{\partial\rho}\frac{\partial\alpha}{\partial z} - \frac{\partial\cos\beta}{\partial z}\frac{\partial\alpha}{\partial\rho} - \frac{\partial\cos\beta}{\partial z}\frac{\partial\gamma}{\partial\rho} + \frac{\partial\cos\beta}{\partial\rho}\frac{\partial\gamma}{\partial z}\right) \\ &= \frac{\ell}{2\pi^2\rho}\frac{\chi}{(\chi^2+1)^2}\left(\frac{\partial\chi}{\partial\rho}\frac{\partial\Phi_L}{\partial z} - \frac{\partial\chi}{\partial z}\frac{\partial\Phi_L}{\partial\rho}\right). \end{aligned} \tag{54}$$

Hence, we have the hopfion number:

$$\begin{aligned} N_H &= \int_{-\infty}^{\infty}\int_{-\pi}^{\pi}\int_0^{\infty}\Sigma\rho\mathrm{d}\rho\mathrm{d}\phi\mathrm{d}z = \frac{\ell}{\pi}\int_{-\infty}^{\infty}\int_0^{\infty}\frac{\chi}{(\chi^2+1)^2}\begin{vmatrix} \frac{\partial\chi}{\partial\rho} & \frac{\partial\chi}{\partial z} \\ \frac{\partial\Phi_L}{\partial\rho} & \frac{\partial\Phi_L}{\partial z} \end{vmatrix}\mathrm{d}\rho\mathrm{d}z \\ &= \frac{\ell}{\pi}\int_{-\frac{\pi}{2}}^{\frac{\pi}{2}}\int_0^{\infty}\frac{\chi}{(\chi^2+1)^2}\begin{vmatrix} \frac{\partial\chi}{\partial\xi} & \frac{\partial\chi}{\partial\psi} \\ \frac{\partial\Phi_L}{\partial\xi} & \frac{\partial\Phi_L}{\partial\psi} \end{vmatrix}\mathrm{d}\xi\mathrm{d}\psi \\ &= \frac{\ell}{\pi}\int_{-\pi}^{(2n_p-1)\pi}\int_0^{\infty}\frac{\chi}{(\chi^2+1)^2}\mathrm{d}\chi\mathrm{d}\Phi_L \\ &= \frac{\ell}{2\pi}\int_{-\pi}^{\pi}\mathrm{d}\Phi_L = n_p\ell. \end{aligned} \tag{55}$$

Figure 23

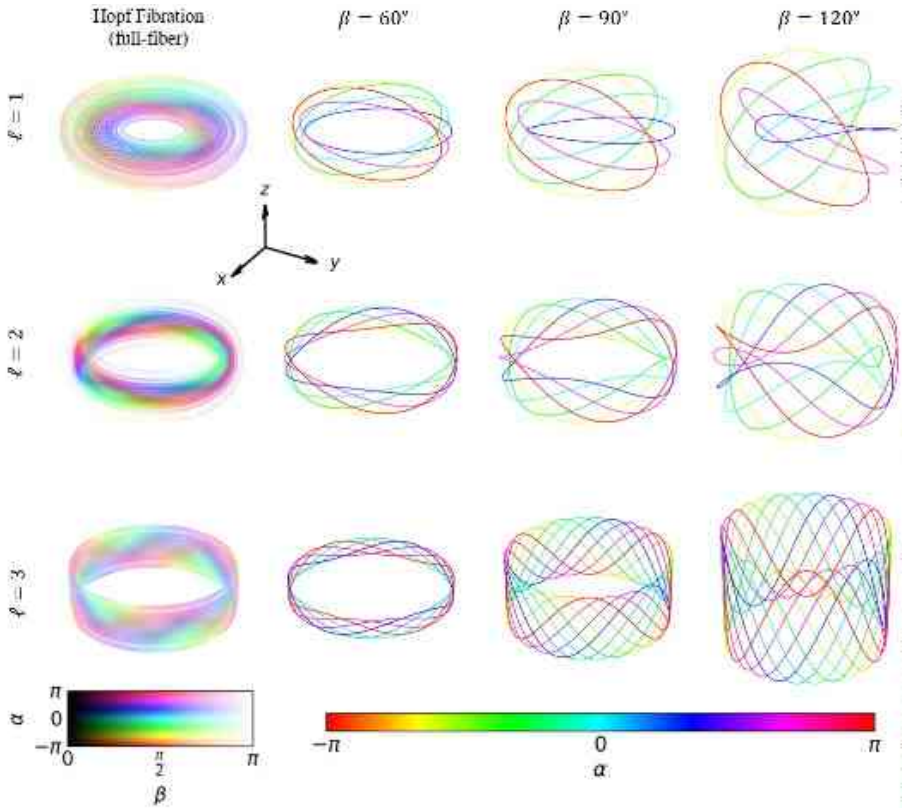

Isopolarization contour lines of $\mathbf{S} = (\sin\beta\cos\alpha,\ \sin\beta\sin\alpha,\ \cos\beta)$ generated by superimposing the LCP component $E_L = \sum_{p=0}^{\ell} C_p LG_{p,0}$ with the RCP component $E_R = LG_{0,\ell}$. Rows correspond to different topological charges $\ell = 1, 2, 3$, while columns correspond to polarization angles $\beta = 60^\circ, 90^\circ, 120^\circ$. Each bundle of closed loops represents trajectories of constant polarization and phase, where the color encodes the mapping from the Poincaré sphere parameters (α, β). The evolution of linkage and twisting of these loops with increasing ℓ and varying β illustrates the 3D knotted topology characteristic of optical hopfions.

We discuss a special case that $n_p = 1$ by carefully modulating C_p, and an ℓ-order Hopfion in 3D real space can hence be obtained. When β is fixed, the isopolarization contours of different α on the 2-sphere form torus knots, and considering all α values covers the entire torus, constructing a single layer of the Hopf fibration. Loops from different β form coaxially nested tori, resembling a "matryoshka doll" structure. These loops define the Hopf index $N_H = n_p \times n_q$, where n_p is the number of windings around the torus and n_q the number through its hole. In Fig. 23, each loop of order ℓ winds ℓ times around and once through, giving $n_p = 1$, $n_q = \ell$, and hence $N_H = \ell$ for the Hopfion generated by Eq. (49). As shown in Fig. 23, higher ℓ leads to more complex contours: for $\ell = 1, 2, 3$, loops knot at the first, second, and third times, respectively, reflecting the increasing topological complexity of higher-order hopfions.

A variety of approaches have been developed for the experimental generation of optical hopfions, typically relying on phase shaping, polarization engineering, and spatiotemporal modulation techniques. These methods provide distinct routes to realize nested toroidal structures, linked polarization filaments, and higher-order topologies in optical fields. Below, we summarize several representative experimental strategies. Many researchers have utilized experimental generation of optical hopfions using phase and polarization manipulation techniques in laser beams [38,120,148,171,262–264].

The generation of optical Stokes hopfions can be approached in two distinct ways: one based on the superposition of LG modes and another relying on STOV modulation. In the first approach, phase-only spatial light modulation is employed to create hopfionic structures by encoding circularly polarized components as Fourier holograms on an SLM operating in split-screen mode. For instance, the RCP component can be realized as a superposition of $LG_{0,0}$ and $LG_{0,1}$ modes to form a vortex ring, while the LCP component is represented by the $LG_{-1,0}$ mode with an axial vortex. Recombination of these components through a polarizing beam splitter and polarization conversion using a quarter-wave plate (QWP) results in the formation of a 3D hopfion structure at the focus, characterized by nested tori of constant polarization ellipticity and linked C-line singularities. Full-field reconstruction of the Stokes parameters and phase yields a Skyrme number close to unity, confirming the Hopf fibration topology [38], as depicted in Fig. 24(a). By superimposing multiple circularly polarized beams with different LG modes, higher-order hopfions can be obtained. For example, an RCP beam formed by $LG_{0,0}$, $LG_{0,1}$, and $LG_{0,2}$ modes, combined with an LCP beam in the $LG_{2,0}$ mode, produces a second-order hopfion with doubly linked polarization filaments. Experimental Stokes parameter reconstructions confirm a Skyrme number near the theoretical prediction of -2, validating the higher-order topology [120] as shown in Fig. 24(b). For higher-order hopfions, the torus-knot indices n_p and n_q are varied, leading to different topological configurations. The Hopf index $N_H = n_p \times n_q$ determines the complexity of the topology, with higher-order hopfions being achieved by modifying the superposition of LG modes, resulting in more intricate polarization patterns and topological textures, including Néel-type, Bloch-type, and antitype configurations [171], as shown in Fig. 24(c). These hopfions are experimentally realized by precisely controlling the phase parameters φ and θ of the LG modes in the expression $(LG_{0,0} + e^{i\varphi} LG_{1,0})|L\rangle + e^{i\theta} LG_{0,\ell})|R\rangle$, enabling the generation of hopfions with tunable topological properties.

The above discussions on optical Stokes hopfions have mainly focused on monochromatic Stokes Hopfions. In contrast, Ref. [177] emphasizes the superposition of bichromatic LG modes under different circular polarization bases, as illustrated in Fig. 25(a). In this framework, the three axes x, y, and ct form the space-time domain of interest. The presence of a beat frequency between the bichromatic components introduces a periodicity along the time axis, enabling the realization of truly spatiotemporal structures. By tailoring the polarization and phase of these bichromatic fields or dipole arrays, skyrmion lattices can be constructed, confined by the temporal envelope of the electromagnetic field. This approach allows the formation of both 1D and 3D skyrmion crystals, significantly extending previous techniques based solely on spatial modulation, and further enabling higher-order topological orders with arbitrary charges.

One approach to theoretically construct photonic spin hopfions is by structuring monochromatic light such that its spin distribution exhibits a hopfion texture in 3D real space [262], as illustrated in Fig. 25(b). This is achieved by engineering the transverse components of the electric and magnetic fields in a specific manner. The spin density vector, which characterizes the photonic spin, is constructed from the electric and magnetic field vectors in the electromagnetic wave. By combining LCP and RCP components with a Gaussian envelope, the photonic spin distribution can be made to exhibit a topologically non-trivial structure. The configuration of the electric field is expressed in terms of two components, each with distinct azimuthal phases, which leads to the creation of a skyrmion texture in a 2D plane. This skyrmion texture co-rotates with the azimuthal angle, creating a twisted loop structure known as a Hopfion in 3D space. The Hopf charge of this texture, which is a topological invariant, can be engineered by modifying the phase and amplitude of the electric field components. By carefully choosing the parameters of these components, the Hopf charge can be

Figure 24

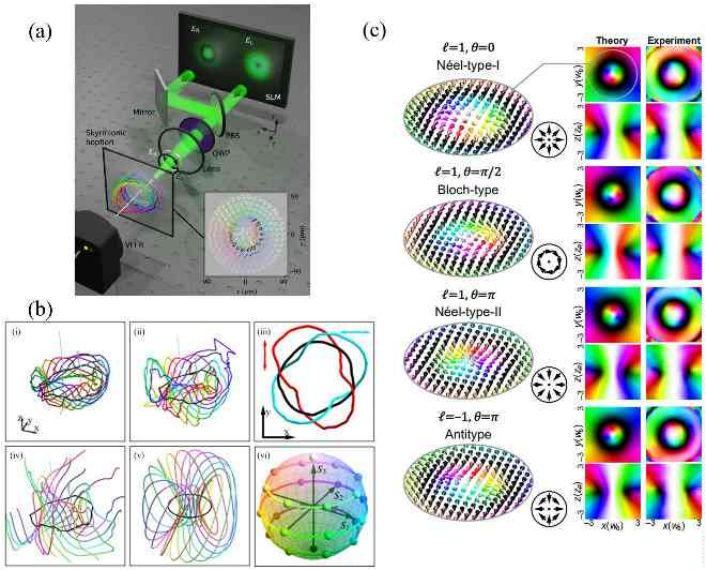

Generation of optical Stokes hopfions by the superposition of LG modes under different polarizations. (a) Schematic of generation of optical hopfions by shaping a laser beam using a phase-only SLM operating in split-screen mode. (b) Generation of optical second order hopfion. The polarization structure of the second-order hopfion is illustrated at varying S_3 values, with (i)–(iv) showing experimental results and (v) presenting simulations. The filaments are color-coded based on their corresponding positions on the (vi) Poincaré sphere. (c) The left panel shows the simulation results of the Stokes vector distributions in the x–y plane, revealing the skyrmionium textures within the photonic hopfions. The right panel shows the theoretical and experimental polarization distributions for the topological hopfions, characterized by Poincaré parameters (polarization ellipse orientation and ellipticity) in the x–y and y–z planes. (a) Reprinted from [38] under a Creative Commons license. (b) Reprinted from [120] under a Creative Commons license. (c) Reprinted from Shen *et al.* "Topological transformation and free-space transport of photonic hopfions," Adv. Photonics **5**, 015001, Ref. [171] under a Creative Commons license.

controlled to produce Hopfions of arbitrary integer values. This method provides a means of generating photonic spin Hopfions with quantized topological charges, and the resulting texture can be used in various applications involving nanoparticle manipulation and fluid dynamics [262].

In summary, experimental generation of optical hopfions has been demonstrated through several complementary techniques, ranging from static beam shaping with phase-only SLMs, to spatiotemporal modulation of pulsed beams, to structured superpositions of LG modes. These methods confirm the existence of diverse hopfionic topologies in optics and provide versatile tools for engineering higher-dimensional topological light fields.

5. PROPAGATION OF OPTICAL SKYRMIONS

As a form of electromagnetic waves, optical fields possess inherent propagation capabilities that enable complex information transfer through their wave properties. The topological light fields not only introduce enhanced topological stability but also provide topological numbers as an exceptional degree of freedom for information

Figure 25

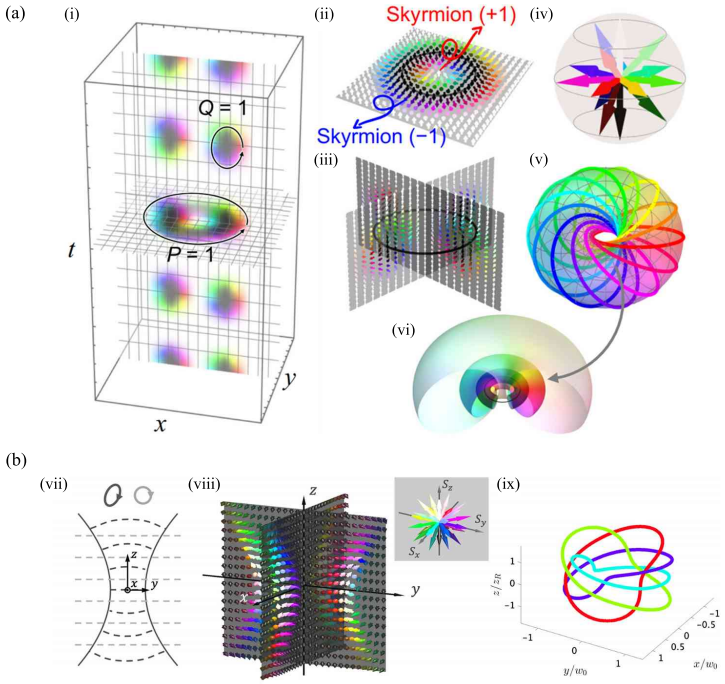

(a) Generation of optical space-time hopfions. (i) A 1D space-time hopfion crystal. (ii) Transverse (x–y) and (iii) longitudinal spin texture cross-sections of a unit hopfion lattice. (iv) Representation of all spin states on a parametric S^2 sphere. (v) Torus-knot configuration formed by the isospin lines of selected equatorial spins. (vi) Layer-by-layer torus-knot fibration shown by all isospin lines in the hopfion lattice. (b) Structure of photonic spin hopfion and its creation. (vii) The structured beam setup: a Gaussian beam (superposition of LCP and RCP, dark lines) and an RCP plane wave (gray dashed lines), both propagating in the $+z$ direction. (viii) Corresponding 3D distribution of the normalized spin vector $\hat{\mathbf{n}}$. The vector orientation is color-coded (see inset), and the visualization uses a modified vector where S_z is divided by 3 before rescaling to unit length. (ix) Lines of constant spin orientation in real space, with colors indicating different orientations. (a) Reprinted with permission from Lin *et al.*, Phys. Rev. Lett. **135**, 083801 (2025), Ref. [177]. Copyright 2025 by the American Physical Society. (b) Reprinted with permission from Wang *et al.*, Phys. Rev. Lett. **131**, 263801 (2023), Ref. [262]. Copyright 2023 by the American Physical Society.

encoding, fundamentally expanding information capacities. As 2D topological structured light fields, optical skyrmions carrying robust skyrmion numbers provide a possibility for stable and high-density information propagation [12,15,36,230,236,265]. These skyrmionic textures exhibit either in spatial domains as planar transverse-field configurations or spatiotemporal domains with dynamic evolution across space-time coordinates. In this section, we will describe propagation properties of skyrmions in both spatial and spatiotemporal domains, focusing on their free-space evolution, quasi-non-diffraction properties, and topological stability in complex media.

5.1. Evolution in Free Space

5.1.1. Evolution of Spatial Optical Skyrmions

Spatial optical skyrmions, including energy flow skyrmions, Stokes skyrmions, and spin skyrmions, evolve during free-space propagation. For Poynting vector skyrmions, light fields in a 4π-focal system can display skyrmionic textures constructed by Poynting

vectors, exhibiting configuration variations across different z coordinates [36]. Another study demonstrates the construction and evolution of optical skyrmions in a 3D energy flux field of free space generated by focusing a vortex beam in a high-NA system, revealing their dependence on both longitudinal inverse energy flow and transverse vortex-like energy flow [266]. These energy flow skyrmions show intriguing evolution characteristics of switchable inverse energy flow along the optical axis, whereas the phase-driven transverse momentum distribution governs the topology and dynamic "zipper-like" splitting behavior of the skyrmions.

Stokes skyrmions in the spatial domain, as topological polarization fields, are paraxial and can propagate with free-space evolution. In Section 3.2.2, we discuss the fundamental topological connections between Stokes skyrmions and optical phase vortices, revealing novel approaches for skyrmion construction and modulation. In addition, their propagation characteristics closely relate to the vortex beam components. The two vortex components with different topological charges exhibit distinct Gouy phases inducing a phase difference during propagation, causing variations in skyrmion configurations over distance [8,15,170,189,230,265,267], as illustrated in Fig. 26. For instance, when two LG beams with coincident focal positions constitute a Stokes skyrmion, the skyrmion can evolve between different types while maintaining its skyrmion number. A skyrmion with positive vorticity can transform from Bloch-type before focus, to Néel-type at focus, and to another Bloch-type with opposite helicity after focus. In contrast, anti-type skyrmions (negative vorticity) rotate in the 2D plane without type changes during propagation [170]. When LG beams focus at different positions, the skyrmion number can vary with propagation distance. These propagation-induced Gouy phase shifts and focal position mismatches between superimposed modes enable dynamic skyrmion number transitions [15]. On the other hand, several recent studies have demonstrated the generation of propagation-invariant topological textures by utilizing metasurfaces or SLMs to engineer the two orthogonal components of Stokes skyrmions [220,230]. Through tailored control of the dimensions and rotation angles of elliptical silicon nanopillars, both the co-polarized and cross-polarized components maintain a constant dynamic phase, enabling the creation of Stokes skyrmions whose topological structure remains stable during propagation [Fig. 18(c)] [230]. All control elements are integrated within a single metasurface, resulting in a compact configuration suitable for integration. Another study proposed the design of propagation-invariant meron lattices, some of which maintain a consistent sign of the Skyrme density [220]. By employing SLMs to modulate multiple interfering plane waves, lattices with various rotational symmetries can be generated. Ensuring that the transverse wavevectors of all plane waves lie on the same ring guarantees the invariance of the configuration upon propagation. These propagation-invariant structures open up new possibilities for the application of topological structured light in both fundamental research and practical technologies.

Initially realized in near field, spin skyrmions were scarcely studied in terms of their propagation properties in free space. Subsequent advances, utilizing tightly focused beams and standing-wave interference, enabled the construction of spin skyrmions in free space [189]. Although—like most optical skyrmions—they are primarily generated through interference rather than nonlinear interactions, these spin skyrmions can exhibit almost full circular or linear polarization and demonstrate unique robustness. This underscores the close relationship between the strong topological characteristics of skyrmions and their remarkable stability. However, non-paraxial generation limits the long-distance propagation of such spin skyrmions. Recent studies have shown that another free-space spin skyrmions can propagate over long distances, which form spontaneously through diffraction effects driven by simple geometric structures under circularly polarized illumination [268]. The symmetry breaking and spin–orbit coupling

Figure 26

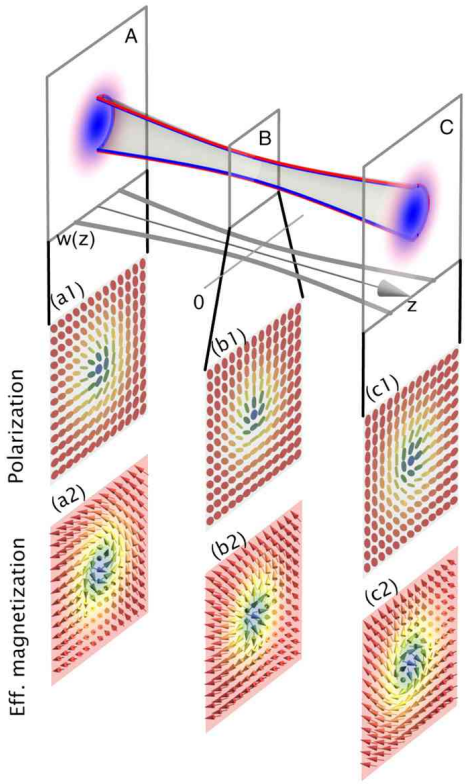

Evolution of Stokes skyrmions. Stokes skyrmions constructed by superposition of vortex beams evolve during propagation. Reprinted with permission from Gao *et al.*, Phys. Rev. A **102**, 053513 (2020), Ref. [211]. Copyright 2020 by the American Physical Society.

introduced by the geometry itself leads to the generation of the spin skyrmion lattice. These spin skyrmion lattices are generated directly in free space can even organize into distinctive spin skyrmion tubes. These findings affirm spin skyrmions as a promising platform for applications leveraging propagation-based topological phenomena. We also anticipate that a wider variety of skyrmions and their novel propagation characteristics will be revealed in future studies.

Furthermore, hopfions, skyrmionic hopfions, and link structures are also intimately connected to the propagation dynamics of skyrmions [38,171,262,264]. A hopfion can be understood as arising from the superposition and co-propagation of multiple beams, thus inheriting intrinsic propagation characteristics. In these quasiparticles distributed in 3D space, we can observe the propagation and evolution of skyrmions along the z-axis, reflecting the deep topological connection between optical skyrmions and hopfions discussed in Section 3. The hopfion texture can be visualized as a twisted skyrmion loop, and indeed, the hopfion itself can be regarded as a distinctive type of linked structure. Studying the inherent properties and evolution of hopfions—whether Stokes hopfions [38,171,264], spin hopfions [262], or other varieties yet to be discovered—is a compelling research direction. For instance, by introducing an additional parameter dimension [262], researchers have identified monopole loops serving as topological defects that separate photonic spin textures with different Hopf charges. Studies of propagation of these topological defects and textures may facilitate the basic understanding of topological light fields and suggest opportunities for engineering topological phenomena.

5.1.2. Evolution of Spatiotemporal Optical Skyrmions

Skyrmionic textures can manifest in short pulses and spatiotemporal domains. These spatiotemporal optical skyrmions introduce an additional temporal degree of freedom, enabling diverse phenomena. Here, we explore the evolution of spatiotemporal optical skyrmions, focusing on TLPs and Stokes skyrmions in spatiotemporal domains.

TLPs are short pulses exhibiting skyrmionic textures. First proposed nearly three decades ago [269], these donut-like few-cycle spatiotemporal wave packets display a distinctive field distribution [12,26,236,242–244,270], as shown in Fig. 20(a). At their center, only longitudinal electric field vectors exist, with no transverse components. Moving radially outward, the transverse electric field components initially increase and then decrease, while the longitudinal electric field first decreases before increasing in the opposite direction. This field distribution constitutes a field skyrmion, with the distribution space manifold forming a curved surface in the spatiotemporal domain. While polarity and helicity of TLPs can be modulated through configuration, their vorticity remains constant at +1 due to their field distribution. During propagation, TLPs will deform, where their configuration evolves with polarity alternating between +1 and −1. These TLPs exhibit space-time non-separable properties that remain invariant during propagation, detailed in Section 5.3.2. TLPs have been successfully generated using metasurfaces [26], and researchers believe that they can be produced through photonic mode resonances in PhC slabs [236], which link spatial frequency k and temporal frequency ω.

Stokes skyrmions in spatiotemporal domains are constructed using STOV, where phase vortices distribute across spatiotemporal domains. These Stokes skyrmions parallel those discussed in Section 5.1.1, with the spatial plane replaced by a space-time plane. While these Stokes skyrmions exhibit asymmetric intensity deformations during propagation, their polarization configurations remain robust, covering the full Poincaré sphere on spatiotemporal planes, thus preserving their skyrmion number [247].

5.2. Quasi-Non-Diffraction

After discussing the fundamental propagation properties, we will then concentrate on several critical and valuable properties of skyrmions. Among these, non-diffraction is a significant property that enables light to maintain its spatial distribution unchanged during propagation. Non-diffracting optical skyrmions can preserve both their spatial intensity profiles and topological characteristics, introducing a robust mechanism for optical information transmission. While perfect skyrmions with non-diffraction require infinite energy or other strict conditions which are experimentally unrealizable, various practical approximations can be applied to achieve quasi-non-diffracting optical skyrmions. In the following sections, we will introduce several implementations of non-diffracting skyrmions in optical fields.

5.2.1. Optical Skyrmions in the Non-Diffracting Vortex Beam Profile

Besides variation during propagation we discussed in Section 5.1.1, the invariant propagation characteristics of optical phase vortices can be transferred to Stokes skyrmions. The Stokes skyrmions can be mathematically represented as superpositions of Bessel vortex beams which are vortex beams well-known for the non-diffraction properties [215,217,265,271,272]. This type of Stokes skyrmions is also called "Bessel skyrmions." Bessel skyrmions manifest as monochromatic non-diffracting beams with non-trivial 2D transverse spatial properties. The light intensity distribution of Bessel beams is localized, maintaining its profile during propagation, which indicates that a Bessel skyrmion is also propagation-invariant. The non-diffracting properties are directly determined by the Bessel beam components and their respective orders [265].

However, an ideal Bessel skyrmion is impossible to experimentally generate due to the infinite width and energy requirements of ideal Bessel beams [265]. This limitation can be circumvented by introducing Gaussian modulation [217], where the superposition of two Bessel-Gaussian beams with different orders generates quasi-non-diffracting Bessel skyrmions. The non-diffraction property of these Bessel skyrmions is partially retained. These skyrmions maintain their light intensity distribution over a finite propagation distance.

Furthermore, the Bessel beam composition of skyrmions introduces additional properties, including skyrmion configuration evolution and self-healing capabilities [265]. Longitudinal intensity mismatch can lead to propagation-dependent skyrmion configuration transitions from Bloch-type to Néel-type, while longitudinal intensity match preserves the skyrmion configuration during propagation. The self-healing property enables Bessel skyrmions to reconstruct their configuration after encountering obstacles during propagation. This property is not limited to Bessel skyrmions, but is also present in other types of skyrmions, such as LG-based skyrmions [273]. These unique properties significantly facilitate the practical application of spatial optical skyrmions.

Recent work has demonstrated the possibility to overcome the infinite width and energy requirements of ideal non-diffracting skyrmions. The topologically structured polarization texture surrounding an optical vortex represents a promising candidate [232,274], where the skyrmionic texture propagates without diffraction and remains confined within a subwavelength-scale tube. Its confinement occurs within a tube whose radius is on the order of or smaller than the wavelength, a dimension dictated by the orbital and spin angular momenta of the host optical vortex. Unlike conventional non-diffracting beams such as Bessel or Airy beams, this structure does not require infinite power or specialized wavefront engineering. The non-diffracting behavior is inherently topological, arising from the skyrmionic polarization texture encircling the phase singularity. Experimental results confirm that the skyrmion remains unchanged in size even as the surrounding vortex beam diverges.

5.2.2. Non-Diffracting Spatiotemporal Light Pulses with Skyrmionic Textures

When considering the temporal dimension, skyrmionic textures can be found in non-diffracting spatiotemporal wave packets in free space, including Stokes merons in the 3D light bullets [25] and field-related skyrmions in the supertoroidal light pulses (STPs) [236]. We firstly clarify the mechanism of non-diffracting properties in non-diffracting spatiotemporal wave packets [275,276]. The non-diffracting properties of spatiotemporal wave packet stem from a special space-time coupling between their temporal and spatial components, which can be understood in frequency-momentum space. This space-time coupling is the relationship between the spatial frequency along z direction k_z and the temporal frequency ω. The space-time coupling of non-diffracting properties can be mathematically expressed as:

$$k_z = k_0 + \left(\frac{\omega}{c} - k_0\right)\tan\varphi, 0 \le \varphi < \frac{\pi}{2}, \tag{56}$$

where k_0 is a constant axial wavenumber, and φ is a parameter angle. Here, to understand the space-time coupling of non-diffracting properties, we can expand the real-space field distribution of the pulses $E(\boldsymbol{r}, z; t)$ into different plane-wave components in frequency-momentum space:

$$E(\boldsymbol{r}, z; t) = \iiint \mathrm{d}\boldsymbol{k}_{\|}\mathrm{d}\omega \widetilde{E}(\boldsymbol{k}_{\|}, \omega) e^{i(\boldsymbol{k}_{\|}\boldsymbol{r} + k_z z - \omega t)}. \tag{57}$$

Here, $\widetilde{E}(\boldsymbol{k}_{\|}, \omega)$ is the plane-wave component. And $\boldsymbol{k}_{\|}$ denotes the in-plane spatial frequency. Moreover, a plane-wave in frequency-momentum space can also be regarded

Figure 27

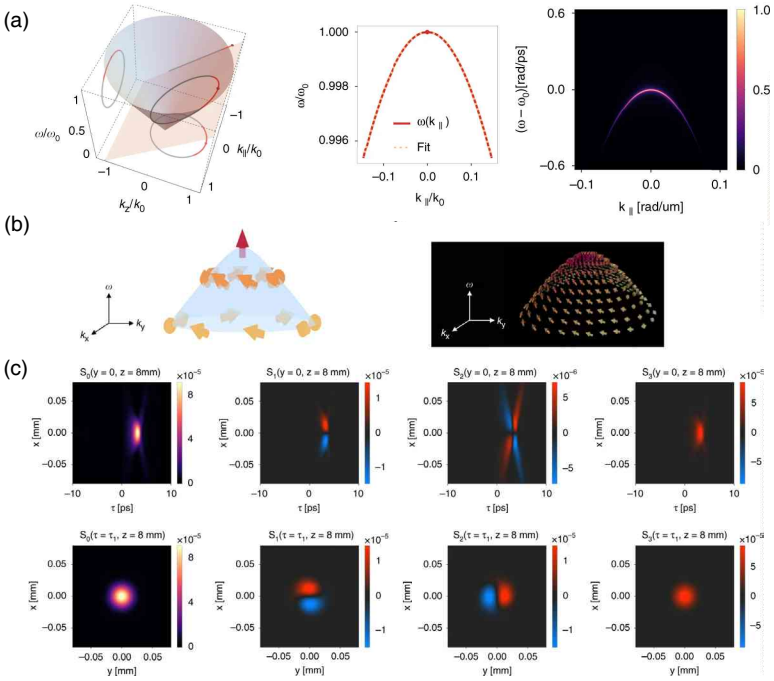

Non-diffracting light bullet with skyrmionic textures. (a) Non-diffracting profile in the light cone and corresponding dispersion. (b) Skyrmionic textures in a photonic band of a non-local PhC slab. (c) Skyrmionic textures in the light bullet. Reprinted from [25] under a Creative Commons license.

as a point in the light-cone:

$$k_{\|}{}^2 + k_z{}^2 = \frac{\omega^2}{c^2}, \tag{58}$$

where c is the speed of light in free space. These relations connecting $\boldsymbol{k}_{\|}$, k_z, and ω, allowing simplification of the Eq. (57) as a function of $\boldsymbol{k}_{\|}$:

$$\begin{aligned} E(\boldsymbol{r}, z; t) &= \iint \mathrm{d}\boldsymbol{k}_{\|} \widetilde{E}(\boldsymbol{k}_{\|}) e^{i(\boldsymbol{k}_{\|}\boldsymbol{r} + k_0 z(1-\tan\varphi) + \omega(\frac{z}{c}\tan\varphi - t))} \\ &= \Phi(\boldsymbol{r}, \frac{z}{c}\tan\varphi - t)) e^{i(k_0 z(1-\tan\varphi))}, \end{aligned} \tag{59}$$

where $\Phi(\boldsymbol{r}, \frac{z}{c}\tan\varphi - t))$ is a function of $(\frac{z}{c}\tan\varphi - t)$. Equation (59) results in the non-diffraction properties, as the same pulsed envelope $\Phi(\boldsymbol{r}, \frac{z}{c}\tan\varphi - t))$ can be found at time t for different z during propagation. The space-time coupling of non-diffraction can also be understood in Fig. 27(b). The intersection of the plane perpendicular to the plane $k_z - \omega$ and the light cone forms this space-time coupling. The plane angle between the plane of this intersection and the plane $k_{\|} - k_z$ equals φ. This intersection can be projected onto the $k_z - \omega$ plane as a unique dispersion. However, this dispersion line cannot actually be generated, since actual pulses exhibit a finite spectral line width in their dispersion.

Both 3D light bullets and STPs are proposed to exhibit similar dispersion and skyrmionic textures, suggesting their quasi-non-diffracting nature. The 3D light bullets are propagation-invariant spatiotemporal light pulses, analogous to real bullets [25]. The dispersion of the light bullets is shown in Fig. 27(a), approximately conforming to the quasi-non-diffracting space-time coupling relationship. These light bullets can be generated through resonances with a photonic band of a non-local PhC slab. The

Figure 28

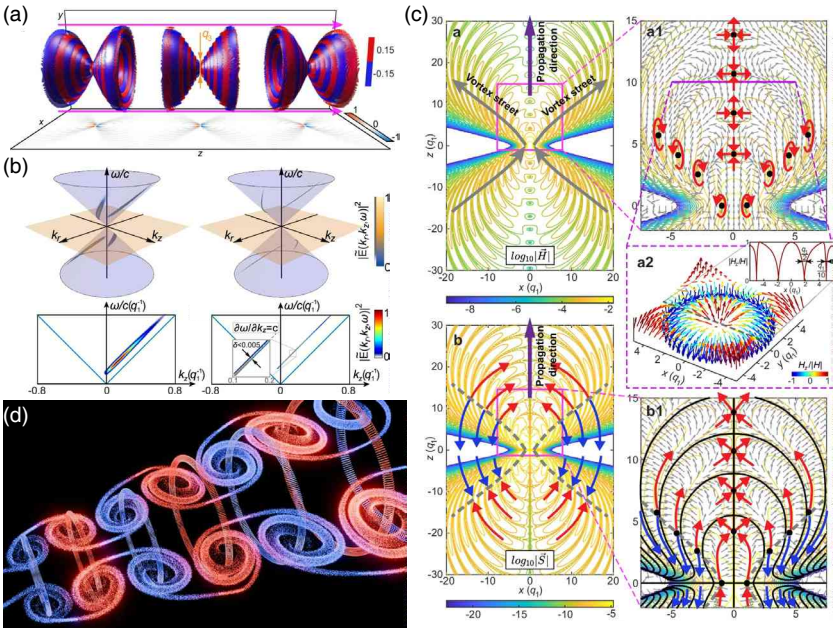

Non-diffracting STPs with skyrmionic textures. (a) The non-diffracting STPs under propagation. (b) Non-diffracting profile in the light cone and corresponding spectrum. Left: the spectrum of an STP with a broad line-width. Right: the spectrum of a non-diffracting STP with a thin line-width. (c) The field distribution, energy flux distribution, and skyrmionic topology of the non-diffracting STP. (d) Schematic of novel 3D Kármán vortex-ring streets in the non-diffracting STP. Reprinted from [236] under a Creative Commons license.

eigen-polarization of this photonic band exhibits a meronic texture, as demonstrated in Fig. 27(b). These meronic characteristics are preserved in the generated light bullet, with the Stokes parameters displayed in Fig. 27(c) clearly showing the characteristics of a Stokes meron. It is noteworthy that such diffraction-free 3D light bullets with merons have been experimentally realized, thereby laying the experimental groundwork for their practical applications [Fig. 22(c)] [259].

As a special type of TLPs, the STPs also manifest as donut-like spatiotemporal wave packets capable of non-diffracting propagation [12,236], as illustrated in Fig. 28(a). The left panel of Fig. 28(b) illustrates the spectrum of an STP with relatively strong diffraction, where the line-width of the spectrum is broad. The right panel of Fig. 28(b) shows the spectrum of a quasi-non-diffracting STP, where the line-width of the spectrum is thin. The dispersion of a quasi-non-diffracting STP approximately follows the non-diffracting mechanism, with a notable absence of electric field distribution at the Γ point in frequency-momentum space. Figure 28(c) shows the real-space cross-section of the non-diffracting STPs. As one type of TLPs, the unique field distributions give rise to skyrmionic topology [Fig. 28(c)] and structures reminiscent of "Kármán vortex-ring streets" in the spatiotemporal field distributions of the STPs [Fig. 28(d)]. These STPs exhibit fascinating properties, such as the formation of mushroom-cloud-like vortex rings [243]. These phenomena have attracted growing experimental interest, with an increasing number of studies [242–244].

These two examples of skyrmionic textures in non-diffracting spatiotemporal wave packets represent just the beginning, with more such textures awaiting discovery. The emergence of skyrmionic textures in the spatiotemporal domain introduces an additional

temporal degree of freedom that enables richer information encoding and manipulation. The combination of non-diffracting properties and unique topological characteristics offers unprecedented opportunities for robust information transmission.

5.3. Topological Stability and Robustness

In the two preceding subsections, we introduced the propagation dynamics, evolutionary characteristics, and quasi-non-diffracting properties of optical skyrmions in free space. These fundamental properties of propagation along with the integer skyrmion numbers establish their potential as information carriers. However, practical propagation environments often involve perturbations such as turbulence, scattering effects, and structural disorder, which differ significantly from idealized free-space conditions. Achieving reliable information transmission in such complex media constitutes a crucial challenge for implementing optical-skyrmion-based propagation systems.

The inherent topological protection and structural robustness of optical skyrmions offer potential solutions for achieving stable propagation in disordered media [95,277,278]. These intrinsic properties confer resistance to optical skyrmions for environmental perturbations, enabling maintenance of structural integrity during propagation through complex media. In this subsection, we will introduce the exploration of the topological stability and robustness of skyrmions in complex media and demonstrate the preservation of topological invariance during the propagation of optical skyrmions.

5.3.1. Topological Stability in Complex Media

The topological stability of optical skyrmions stems from their non-trivial topology, which provides robustness in complex media through global topological invariants [278–280]. This capability is not absolute. It enables skyrmions to demonstrate superior anti-perturbation capabilities in complex environments, such as isotropic noise and scattering media. The topological stability can help minimize changes in the information carriers, offering advantages over traditional methods to reduce perturbation.

Recent studies have validated and expanded the interpretation of the topological stability of optical skyrmions from multiple perspectives. Early studies primarily focused on experimentally demonstrating the stable propagation of various types of skyrmions through different complex media. Various field skyrmions constructed by 3D vectorial holography are observed to propagate through disorder media, including Néel-type, Bloch-type, anti-type, merons, and quarter-skyrmions [277], as shown in Fig. 29(a). These skyrmions maintained robustness when propagating through two types of disorder media (with discontinuous and continuous variations of the dielectric constant). While strong disorder media caused some distortions, the topological features remained preserved. The topological configurations and skyrmion numbers show stability against phase disorder but relative sensitivity to amplitude disorder. Stokes skyrmions' topological stability has been extensively investigated, demonstrating stability during propagation through various complex media, including nonlinear media [281], metafiber [19], atmospheric turbulence [282], waveguides [283], and scattering media [284]. Moreover, Stokes skyrmions exhibit measurement-free topological resilience against randomness, requiring no pre- or post-correction about the propagating medium. This robustness has been experimentally demonstrated [279], which showed that the wrapping topology of the skyrmion remains invariant upon transmission through random media, even though light intensity becomes severely distorted. Their work represents a breakthrough in overcoming real-world optical distortion using Stokes skyrmions transmitted through complex media, achieving for the first time nearly perfect robust optical communication. This advancement paves the way for applying topological light—both classical and quantum [23,27,104]—in optical communications and other

Figure 29

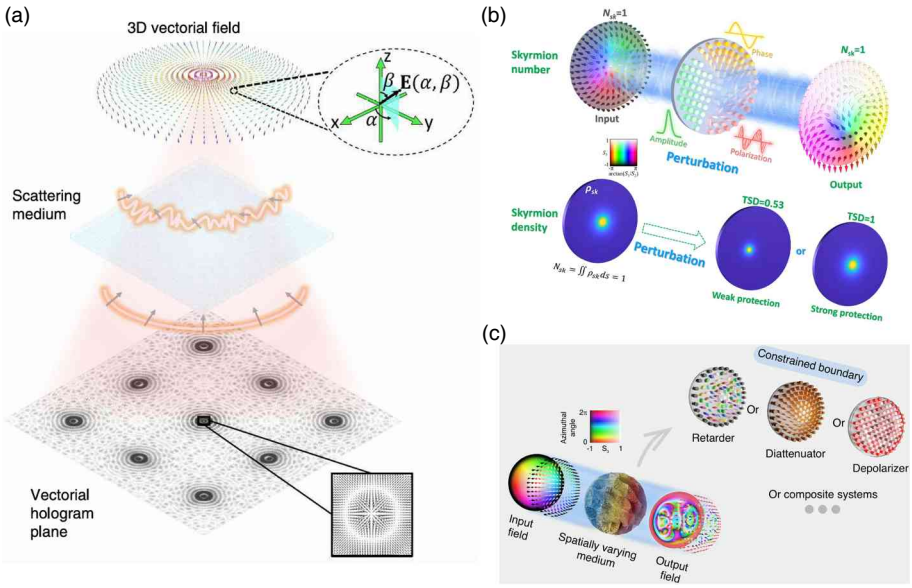

Propagation of optical skyrmions in complex media. (a) Field skyrmions propagate through scattering mediums [277]. (b) Topological similarity degree of skyrmions [278]. (c) Stokes skyrmions with different orders propagate through corrupting elements [95]. These skyrmions with compatible boundaries exhibit topological stability, maintaining their skyrmion numbers and topological configurations. (a) Reprinted with permission from Liu *et al.*, Phys. Rev. Lett. **129**, 267401 (2022), Ref. [277]. Copyright 2022 by the American Physical Society. (b) Reprinted with permission from [278]. © 2025 Chinese Laser Press. (c) Reprinted from [95] under a Creative Commons license.

information processing technologies. Stokes skyrmions exhibit stability not only in classical regimes but also in quantum settings [27,285]. Even when quantum skyrmions are subjected to noise or experience a reduction in entanglement, their topological properties remain robust.

With advancing research, the study of skyrmion topological stability is transitioning from qualitative descriptions to quantitative analysis. A study proposed the significant concept of "topological protection degrees of optical skyrmions," which quantitatively evaluates the stability of optical skyrmions under perturbations for the first time [278], as shown in Fig. 29(b). Besides, they designed a compact electrically controlled generator that can flexibly generate optical skyrmions. This work establishes a novel quantitative perspective for evaluating the stability of optical skyrmions through complex media, which may be extended to the stability of other topological textures.

Some studies have moved beyond experimental demonstration and are incorporating mathematical frameworks to reveal the mechanism of topological protection. A study breakthroughly revealed the significance of skyrmion boundaries [95]. As discussed in Section 3.1.1, boundary-determined compactification influences fundamental skyrmionic topology. This work discovered that skyrmion topological stability originates from compatible boundaries [95]. Skyrmions with compactification maintain near-integer skyrmion numbers when encountering various phase differences, including depolarizers, retarders, diattenuators, and their composite systems [Fig. 29(c)]. While skyrmion number errors remain relatively small, they tend to increase with higher skyrmion numbers. This group also proposed a tunable linear retarder arrays, which can be used for generating, analyzing, and correcting the skyrmionic beams [286]. Their work provides a versatile and powerful platform for researching the propagation of

skyrmions and the topological protection. These insights all enhance our understanding of topological stability across various skyrmions and can be extended to other physical systems like magnetism and acoustics.

The topological stability of optical skyrmions represents a direct manifestation of their topological invariance in complex media, as demonstrated through theoretical models and experimental verification. Their key advantage lies in encoding information within topological properties, circumventing the noise sensitivity of traditional information transmission systems. Future research opportunities exist in exploring interactions between skyrmion topological protection and complex media to optimize their application in information technology.

5.3.2. Invariance of Optical Skyrmions

Invariance of light fields seems to be an ideal concept. As light propagates through complex media, it inevitably encounters various disturbances, including diffraction, scattering, obstruction, and reflection. While topological stability can reduce the impact of these disturbances on topological light fields, complete elimination remains challenging. This leads to an alternative approach: seeking invariants underlying the topological light field rather than focusing on the topological light field itself. In this subsection, we will explore such invariance in optical skyrmions during complex media propagation.

Classical entanglement represents one form of invariance in optical skyrmions [270,287–291]. Unlike non-local quantum entanglement, classical entanglement manifests locally, representing non-separability between two light field quantities, such as spin–orbit non-separability in vectorial beams [160,292] (e.g., Stokes skyrmions) and space-time non-separability in TLPs [26,242–244,246,270,293]. This entanglement establishes one-to-one correspondence between two quantities. In spin–orbit non-separability, the phase vortex (orbit, OAM) and polarization (spin, SAM) of such vectorial beams become classically entangled, with vortex components corresponding to specific polarization states. Measurement of a polarized component determines the vortex charge of the component. During propagation, the entanglement entropy, which quantifies the degree of the entanglement, remains invariant in complex media, due to the unitary nature of perturbation matrices. This invariance persists under various perturbations, including tilted lenses, atmospheric turbulence, and optical fibers, preserving information transmission. This novel approach was first demonstrated using vectorial vortex beams by Forbes' group, and they also demonstrated the optical communication capability of vectorial vortex beams via this approach, but its applicability is not limited to vectorial vortex beams [160]. Higher-dimensional structured light fields [103], such as Stokes skyrmions, also arise from superpositions of two classically entangled bases, where the method may be applied to reveal their entanglement invariant entropy. This technique opens up new possibilities for applications of skyrmions such as robust optical communication [160,294].

Similarly, as shown in Fig. 30, TLPs exhibit space-time non-separability through frequency-momentum-space spectrum, where wavevectors closely correspond to specific frequencies, manifesting as position-dependent wavelength content across the transverse plane [26,270,293]. Experimental studies have demonstrated the classical entanglement and robust topological resilience in propagating TLPs [26,242–244]. These results demonstrate their remarkable ability to maintain structural stability against perturbations. Notably, such achievements overcame long-standing challenges in measuring the longitudinal field component and capturing the full spatiotemporal structure of the pulses. These capabilities open promising avenues for applications in robust optical communications and structured light technologies.

Figure 30

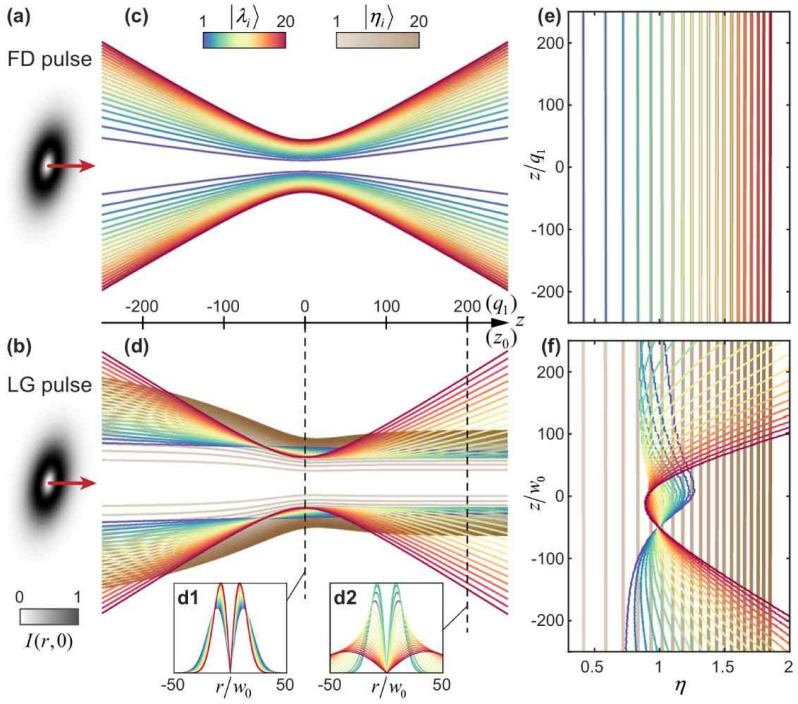

Classical entanglement of TLPs. (a), (c), and (e) The isodiffraction propagation profiles of TLPs. One wavelength component λ_i corresponds to the same radial ratio of $\eta_i = r_i/r_{max}$ at different propagation distances z. (b), (d), and (f) The propagation profiles of LG pulses without isodiffraction. Reprinted from Shen *et al.*, Phys. Rev. Res. **3**, 013236 (2021), Ref. [270] under a Creative Commons license. Copyright 2021 by the American Physical Society.

Generalized skyrmions offer a new topological perspective on invariance under perturbations [295]. Skyrmion instability in complex-media propagation typically results from compromised compactness, preventing complete Poincaré sphere wrapping. The perturbed field wraps around only several small areas of the Poincaré sphere instead of the full surface. However, considering these areas as complete topological invariants offers a way to neutralize perturbation effects. This perspective suggests that any formation maintaining certain Poincaré sphere coverage constitutes a skyrmion. The generalized skyrmion number remains almost invariant unless the Poincaré sphere wrapping suffers complete destruction. This concept extends beyond incomplete wrappings to encompass repeated wrappings and singularities, potentially enabling additional skyrmion numbers within single light fields.

The study of optical skyrmion invariance offers exciting possibilities for both fundamental research and practical applications. The discovered invariance, from classical entanglement to generalized skyrmions, provides robust frameworks for information encoding and transmission through complex media. The concept of generalized skyrmions particularly promises new approaches to topology-protected information processing and communication systems. Understanding and utilizing these invariance properties could revolutionize optical communication technology, enabling more reliable and efficient information transmission through challenging environments. Moreover, these principles might find applications beyond optics, influencing fields such as quantum computing, materials science, and telecommunications. Further study directions might explore more invariance mechanisms and their hybrid, combining multiple types of invariance to enhance stability.

6. DYNAMIC MANIPULATION OF OPTICAL SKYRMIONS

Dynamic manipulation techniques allow researchers to tailor skyrmions in response to external stimuli, such as phase modulation, polarization control, and structured light engineering. By adjusting the excitation conditions or introducing additional degrees of freedom (such as spin–orbit coupling effect), one can achieve precise control over skyrmion textures and positions. Furthermore, real-time manipulation of optical skyrmions paves the way for innovative applications in optical communication, information storage, metrology, or quantum information science. In this section, we will discuss the approaches to dynamically manipulate the characteristics for different types of optical skyrmions such as field skyrmions, spin skyrmions and Stokes skyrmions.

6.1. Manipulation of Field Skyrmion

Taking optical field skyrmions formed through the SPP interference as examples, their manipulation relies on three interdependent mechanisms: the characteristics of the incident optical field, photonic structures enabling light–SPP coupling, and medium interactions during SPP propagation. The incident optical field, defined by its phase, polarization, and intensity, sets the initial conditions for SPP excitation and interference. Photonic structures, including various plasmonic architectures such as plasmonic gratings and metasurfaces, along with structural symmetry [182], enable efficient light–SPP coupling and shape the skyrmion field. Meanwhile, properties of the medium—such as refractive index variations, chirality, and material anisotropy—govern SPP dispersion and stability, further influencing skyrmion dynamics. Specifically, the field skyrmion manipulation has been achieved through four key parameters: the phase and intensity profile of the excitation light [20,296,297], the geometric design of SPP couplers [298], and the material properties [296,299] of the surrounding medium. A conceptual schematic is presented in Fig. 31(a).

An early simulation work [20] proposed demonstrates dynamic control over optical skyrmion lattices formed by the interference of three pairs of SPP standing waves, which are excited by the Gaussian beams coupled through hexagonal gratings, as shown in Fig. 32(a). The study employs FDTD simulations with a grating structure fabricated on a 120-nm-thick silver film. The grating period is 485 nm, designed to match the SPP wavelength excited by a 532 nm beam. Each slit has a length of 5.8 μm and a width of 194 nm. The key parameter to manipulate SPP field skyrmions is the phase difference $\phi_{spp1} - \phi_{spp2}$ between the two excited SPP waves within each pair of SPP standing waves. This phase difference is given by: $\phi_{spp1} - \phi_{spp2} = (\phi_1 - \phi_2) + (\varphi_1 - \varphi_2) + \pi$, where ϕ_1, ϕ_2 are the initial phases of the two excitation beams, and φ_1, φ_2 are their relative polarization directions. By changing the phase difference, the SPP standing wave pattern can be spatially shifted, ultimately leading to a modification of the entire skyrmion texture. Specifically, when the polarization directions are fixed, the shape and position of the skyrmion lattice can be dynamically manipulated by independently controlling the phases of the six excitation beams (ϕ_1 to ϕ_6). For instance, altering the phase difference of one pair of standing waves from 0 to $\pi/2$ (setting $\phi_1 = \pi/2$) shifts the yellow standing wave upward by 1/4 of its period [see Fig. 32(b)]. This adjustment modifies the overall symmetry of the interfering waves, leading to a transformation of the skyrmion unit cell shape. More precisely, the unit cell changes from hexagonal to triangular, with the triangle orientation (upward or downward) depending on whether the phase difference is $+\pi/2$ or $-\pi/2$. Meanwhile, adjusting the phase difference of two pairs of standing waves from 0 to π (setting $\phi_2 = \phi_3 = \pi$) induces a lateral shift of the entire lattice. The displacement is 0.433 times the SPP wavelength relative to its original position. This shift occurs without altering the hexagonal shape of the lattice.

Figure 31

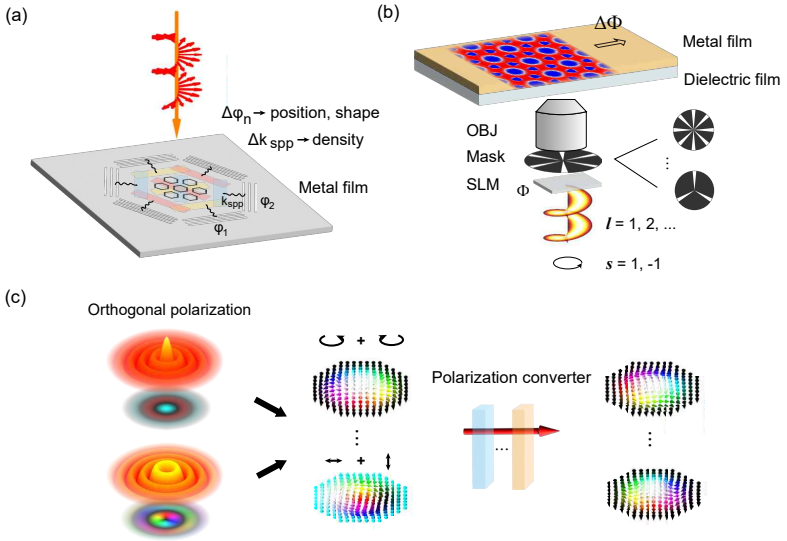

Simplified mechanism of manipulating various types of skyrmions. (a) The interfering SPP field skyrmion patterns can be manipulated by tuning the initial phase and wavevectors, which depend on the input structured light, excitation geometry, and surface properties. (b) Spin skyrmions generated by tightly focused spin–orbit coupling vector beam can be manipulated by tuning the shape of the aperture, the phase profiles and the topological charge of the incident light. (c) The dynamic manipulation of Stokes skyrmion can be achieved by passing the initial skyrmions through a series of wave plates.

Later, a method for manipulating optical skyrmions and merons by modifying field symmetry and introducing chirality in plasmonic structures based on metal–chiral–metal waveguides was presented in [296], as shown in Fig. 32(b). The key ideas of this work are to control the transformation between skyrmions and merons through field symmetry and to modulate the twist degree of the fields using material chirality. In the study, the field symmetry is altered by adjusting the phase relationships of the SPP waves excited through the slits patterned in hexagonal or square plasmonic structures. For example, increasing the phase of one of the three pairs of SPP standing waves in a hexagonal lattice by π (e.g., $\phi_2 = \phi_5 = \pi$) laterally shifts the skyrmion lattice. In addition, introducing a π phase shift in the SPP wave excited through a single slit (e.g., $\phi_2 = \pi$) transforms the skyrmion lattice into a meron lattice. The introduction of a chiral material within the plasmonic structure modifies the initial wavevector relation $k_x^2 + k_y^2 - k_z^2 = k^2$, resulting in the splitting of the hyperboloid into two separate hyperboloids in momentum space: $k_x^2 + k_y^2 - k_{z\pm}^2 = k_\pm^2, \quad k_\pm = (n_0 \pm \xi)k_0$, where ξ is a chirality parameter. This splitting occurs because circularly polarized light is always an eigenmode in a chiral medium, leading to an asymmetry between the left- and right-circularly polarized components. As a result, the normal spin component $\mathbf{S_n}$ (the normal part of the spin texture) splits into two components, $\mathbf{S}_-$ and $\mathbf{S}_+$. This separation introduces an additional spin component, the longitudinal spin $\mathbf{S_L}$, which is perpendicular to $\mathbf{S_n}$ and parallel to the local wavevector. Unlike the transverse spin, which is locked to the energy flow (or the local wavevector) and reverses its sign across the boundary—this being the reason why, in a non-chiral system, the skyrmion is always Néel-type—$\mathbf{S_L}$ does not obey the spin-momentum locking rule. Instead, it remains unchanged, with its sign solely determined by the chirality parameter ξ. This longitudinal spin component induces an enantioselective twist in the

Figure 32

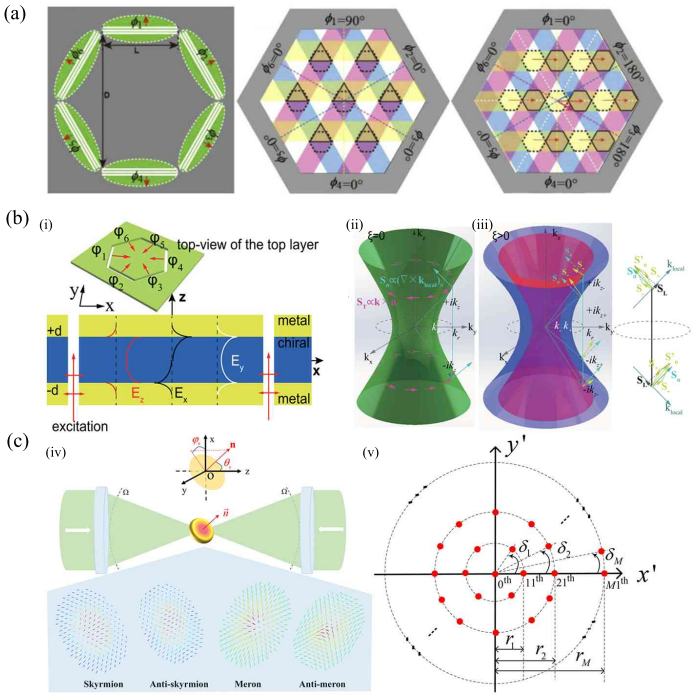

Manipulation of field skyrmions. (a) Schematic diagram of grating structure and the shape and position of the skyrmions. The grating structure with six excitation beams generates SPP standing waves. By adjusting the phase of these beams, the shape and position of skyrmions can be dynamically controlled, enabling tunable optical topologies. Reprinted from [20] under a Creative Commons license. (b) Skyrmion manipulation by controlling field symmetry and structural chirality. (i) Schematic of hexagonal plasmonic coupling pattern and typical electric field distributions in a metal-chiral-metal structure. (ii) and (iii) The introduction of chirality splits the hyperboloid into two, resulting in the transformation of Néel-type skyrmions to Bloch-type. Reprinted from [296] under a Creative Commons license. (c) Manipulation of field skyrmion in free space. (iv) Schematic illustration of optical setup to manipulating electric-field skyrmions and merons in the focal region by applying MCAD. (v) Arrangement of the dipoles of MCAD. Reprinted from [300] under a Creative Commons license.

skyrmion and meron textures, effectively governing the transition between Néel-type and Bloch-type skyrmions. Specifically, the sign of ξ dictates the twist direction of Bloch-type skyrmions: a clockwise rotation for $\xi < 0$ and a counterclockwise rotation for $\xi > 0$.

In addition to manipulating field skyrmions in the SPP surface wave system, skyrmions in free space can also be controlled. Recent study [300] presented a method [shown in Fig. 32(c)] for dynamically manipulating tightly focused optical skyrmions and merons by controlling the distribution of electric-field vectors. The key innovation lies in utilizing a multiple concentric-ring array of dipoles (MCAD) as a radiation source within a 4π-focusing system to tailor the electric-field vector distribution in the focal region. By adjusting the oscillation direction of each dipole [red dots in Fig. 32(b)] in the MCAD, specifically their polar angle ($\theta_{d,m}$) and azimuthal angle ($\varphi_{d,mn}$), the topology types (Néel, Bloch, intermediate, and anti-skyrmion/meron) can be controlled. Specifically, the topological parameters polarity (p), vorticity (v), and helicity (φ_r) serve as the main degrees of freedom for manipulation, which are tightly related to

$\theta_{d,m}$ and $\varphi_{d,mn}$ as:

$$\theta_{d,m} = (p+1)\pi/2 - p\theta'_{d,m},$$

$$\varphi_{d,mn} = v \cdot \varphi_{p,mn} + \varphi_r.$$

Here, $\theta'_{d,m}$ denotes the initial oscillation polar angle of the dipoles in the mth ring. Polarity is determined by the oscillation direction of the 0th dipole ($p = \pm 1$), which dictates the out-of-plane orientation. The helicity φ_r, which influences the initial phase of the in-plane electric-field vector, enables continuous deformation between Néel- and Bloch-type textures. Adjusting vorticity ($v = \pm 1$) switches between skyrmions and anti-skyrmions. Furthermore, the normal direction of the MCAD arrangement plane, defined by angles θ_0 and φ_0, allows for the generation of skyrmions and merons on arbitrarily specified planes. This can be integrated with the previously applied MCAD manipulation methods for comprehensive control of the focused optical topology.

6.2. Manipulation of Spin Skyrmions

The formation of SPP spin skyrmions fundamentally originates from the intrinsic transverse spin–orbital angular momentum lock-in effect in surface waves and the symmetry-dependent multi-beam plasmonic interference. These two fundamental mechanisms enable two primary approaches for manipulating spin skyrmions: orbital component engineering and interference symmetry control. In the orbital component engineering approach, the topological charge distribution can be directly reconfigured by tailoring the spin and OAM of the excitation light using polarizers and SLMs. For interference symmetry control [192,301,302], amplitude masks [14,303] allow precise tuning of the interference symmetry in propagating SPPs, which enables dynamic switching between skyrmion and meron configurations. Recently research has shown that interference symmetry can be decomposed into controllable sublattices, enabling programmable topological transformations in photonic spin quasicrystals [304]. Meanwhile, the material properties [192,305–307] also provide alternative approaches to influencing the system's symmetry, thereby enabling control over skyrmion textures. An illustrative schematic is provided in Fig. 31(b) for clarity.

Early research [34] demonstrated dynamic position control of photonic spin skyrmions by imposing a phase profile on the incident laser beam, as shown in Fig. 33(a). The key method involves employing an SLM to add a cosine phase profile, $\Phi = 2\pi d/\lambda_{\mathrm{SPP}} \cos(\varphi - \varphi_0)$, where d is the shifting distance, φ_0 is the shifting direction with respect to the x-axis, φ is the azimuthal angle of the phase profile, and λ_{SPP} is the SPP wavelength. Based on the Fourier shift theorem, by adjusting d and φ_0, the SLM enables precise and flexible 2D control of the skyrmion's position in real space without distorting its spin textures. Experimentally, a circularly polarized vortex beam with a topological charge 1 is focused to generate the spin skyrmions, and their spin textures are mapped using a nanoparticle-on-film configuration. The experimental results show that the photonic skyrmion can be manipulated along the x-axis by varying d from $-2\lambda_{\mathrm{SPP}}$ to $2\lambda_{\mathrm{SPP}}$, and it can be made to circle around the original position by varying φ_0 from 0° to 360°. The authors also demonstrate that when a LC plate is used instead of the SLM to provide the phase profile, the shifting directions of the photonic skyrmions become intrinsically locked to their chirality. Unlike the SLM, which is only effective for linearly polarized light, the LC plate interacts with the incident circular polarization through the anisotropic alignment of its molecules. As a result, skyrmions with opposite topological charges exhibit opposite shifting directions, demonstrating a chirality-dependent transport mechanism. This effect originates from the spin–orbit interaction induced by the LC molecules, which mediates the phase accumulation in a polarization-sensitive manner.

Figure 33

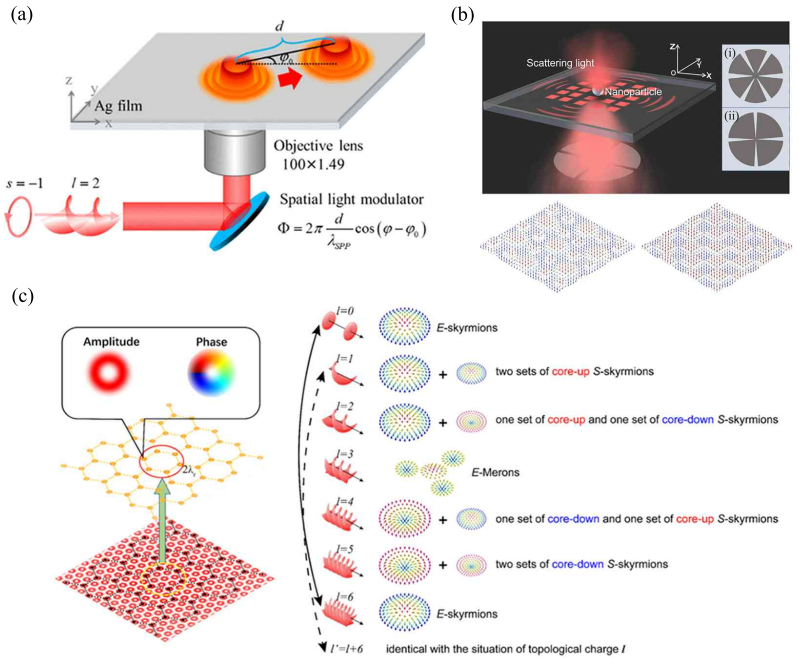

Manipulation of spin skyrmions. (a) Schematic of the experimental setup for spin skyrmion position control. An SLM modulates the phase of an incident vortex beam, which excites SPPs on an Ag film. The interference pattern, governed by the modulation phase **Φ**, allows precise control over the skyrmion position along the defined trajectory. Reprinted with permission from Lin *et al.*, ACS Photonics, **8**, 2567–2572 (2021) [34]. Copyright (2021) American Chemical Society. (b) Spin lattice manipulation through symmetry control. A radially polarized beam excites SPPs on a thin silver film, where intensity masks with six-fold or four-fold symmetry modulate the incident beam. The resulting spin–orbit interaction enables the formation of spin-skyrmion or spin-meron lattices. Reprinted with permission from Lei *et al.*, Phys. Rev. Lett. **127**, 237403 (2021), Ref. [14]. Copyright 2021 by the American Physical Society. (c) Schematic of OAM-controlled topology engineering in skyrmion lattices. Various OAM states manipulate the resulting skyrmion or meron patterns, dynamically tuning the hexagonal lattice topology and enabling selective generation of distinct configurations. Reprinted with permission from Zhang *et al.*, Appl. Phys. Rev. **11**, 011409 (2024) [308]. Copyright 2024, AIP Publishing LLC.

Besides controlling the position of spin skyrmions, a concurrent study [14] demonstrated dynamic manipulation of photonic skyrmions and merons by controlling the symmetry of the electromagnetic field through spin–orbit coupling, as shown in Fig. 33(b). The key method involves applying intensity masks with either six-fold or four-fold symmetry. Experimentally, an incident radially polarized laser beam with a helical wavefront (topological charge $l = 1$, wavelength $\lambda = 532$ nm) was modulated by intensity masks and then focused onto a thin silver film. This excitation generated SPPs carrying OAM at the air–silver interface, ultimately leading to the formation of spin Néel-type skyrmion textures. The symmetry of the mask dictates the resulting spin texture: six-fold symmetry induces spin-skyrmion lattices, while four-fold symmetry produces spin-meron lattices. This control mechanism arises from the interference of SPPs under conditions of broken rotational symmetry, which governs the formation and spatial distribution of the spin textures. The resulting spin structures are then characterized using a spin-resolved near-field scanning optical microscope, with a dielectric nanosphere serving

as a near-field probe. Furthermore, the study points out that in the absence of spin–orbit coupling ($l = 0$), the spin lattices transition into dynamic field-skyrmion or field-meron lattices. This transition bridges the manipulation of spin-skyrmions with dynamic field-skyrmions, revealing their common origin in interference-based SPP excitations.

Recently, a study presented both experimental and theoretical evidence of the periodic vectorial characteristics of field- and spin-based skyrmion lattices, controlled by plasmonic vortices with varying topological charges, as shown in Fig. 33(c). By adjusting the topological charge l of the incident vector beam in conjunction with system symmetry, the researchers achieved the selective formation of distinct skyrmion and meron topological structures. The study indicates that the vortex patterns within the lattice are organized based on periodic tiling, which is dictated by the symmetry of the lattice. This periodic tiling enforces a structured periodicity on the topological charges, aligning with the lattice's rotational symmetry. Consequently, this alignment influences the coupling of energy flow density among individual vortices, with variations depending on different OAM values. Experimentally, radially polarized laser beams (wavelength: 532 nm) with different helical wavefronts were shaped using an SLM and served as excitation sources. The interplay of various OAM and hexagonal/square symmetry leads to distinct spin or filed skyrmion lattices. Specifically, the study reveals a variety of skyrmions or merons topological structures by altering the topological charge (l) of the incident vector beam, from $l = 0$ to $l = 5$ for hexagonal (exhibiting a periodicity of 6 in OAM, which means that l and $l + 6$ produce identical lattice configurations) and $l = 0$ to $l = 3$ for square lattices. The field lattices are formed arising from the absence of spin–orbit interaction when $l = 0$ (field skyrmions) and $l = N/2$ (field merons where N defines the N-fold rotational symmetry of the lattice), while the rest of the topological charges result in the spin skyrmions combining of two sets of skyrmion sublattices.

6.3. Manipulation of Stokes Skyrmions

At the generation stage, by tailoring the OAM of the orthogonal polarization components, particularly through modulation with SLMs, various skyrmion states can be generated [215,309,310]. Following their generation, the control of the skyrmion mainly focuses on manipulating their local spatial polarization and tuning the orthogonally polarized structured light components. One texture can be transformed into another through multiple pathways, such as polarization tuning and local spatial modulation, as previously mentioned, as well as via direct skyrmion–skyrmion interactions [311]. Specifically, since the topological texture of Stokes skyrmions is determined by their spatial polarization distribution, optical components capable of modulating polarization can be employed to flexibly manipulate their texture. For example, wave plates [16], lenses [267,312], a Pancharatnam–Berry phase approach utilizing waveplate combinations [313], or other polarization-converting devices [176] provide a versatile means to dynamically tailor skyrmion textures. In addition, based on the principle of their generation, dynamic manipulation can be achieved by adjusting the combination of orthogonal polarization components and different topological charges of the incident optical field [19]. The overall process is illustrated in Fig. 31(c). In addition, tailoring the phase distribution of skyrmions could also enable intriguing manipulations, endowing them with unique profiles or propagation characteristics [176,226].

Since Stokes skyrmions are described by Stokes parameters, their manipulation can be characterized using Mueller matrices. By predesigning the target Stokes vector form of the skyrmion pattern, the required wave plates with specific phase delays and initial fast-axis orientations can be determined. Previous study [16] demonstrated dynamic manipulation of Stokes skyrmions using wave plates characterized by Mueller matrices. This approach enables controlled conversions between different skyrmion types, as

shown in Fig. 34(a). In their study, helicity, vorticity, and polarity are identified as three critical parameters for tailoring skyrmion textures. Specifically, a polarization rotator (PR), composed of two QWPs and a retarder, is used to modulate skyrmion helicity. Setting the PR's rotation to $\frac{\pi}{4}$ converts an incident Néel-type skyrmion into a Bloch-type skyrmion, as it effectively rotates the Stokes vector in the S_1-S_2 plane. A single half-wave plate (HWP) is used to reverse skyrmion polarity (e.g., transforming a Néel skyrmion into an anti-skyrmion) and simultaneously affect vorticity, as it alters the orientation of the S_3 Stokes parameter. In addition, homeomorphic conversion, such as the transformation of skyrmions into bimerons, is achieved using two QWPs set at $-\frac{\pi}{4}$ and $\frac{\pi}{2}$. Furthermore, the superposition of skyrmions with differing helicities or polarities is experimentally demonstrated, enabling the creation of complex structures through their fusion and annihilation. For instance, superimposing Néel-type and Bloch-type skyrmions results in an intermediate skyrmion state, whereas superimposing Néel and anti-skyrmions leads to skyrmion annihilation, resulting in a non-skyrmion state. The entire process is experimentally verified using a vectorial optical field generator, showcasing excellent agreement between theoretical predictions and experimental results.

A later study [312] demonstrated the dynamic manipulation of Stokes skyrmions through various configurations of cascaded gradient-index (GRIN) lenses [shown in Fig. 34(b)]. GRIN lenses are optical elements with a spatially varying refractive index profile and inherent birefringence, making them highly customizable components for shaping the polarization state of light. In this work, through the careful arrangement of GRIN lenses, either alone or in combination with different types of wave plates, a diverse range of skyrmion numbers (characterized by vorticity, polarity, radiality and centrality), and different skyrmion types can be manipulated. Specifically, polarity N_p, which is determined by the central spin state (either spin-up or spin-down), is controlled by the input polarization. In the case of a single GRIN-lens segment, tuning the input light polarization from LCP to linear polarization and then to RCP causes the skyrmion to evolve through intermediate states such as biskyrmions and quadrumerons, ultimately transforming into a skyrmion with opposite polarity. The radiality N_r of skyrmions, which represents the number of radially nested skyrmion structures, is controlled by the cascading of GRIN lens segments. For instance, a single GRIN lens segment produces a skyrmion, while cascading two identical segments results in a skyrmionium. In addition, vorticity N_v, determines the vortex charge of the transverse (x, y)-component distribution; Centrality N_c, interpreted as the number of singularities in the transverse-component distribution of the multiskyrmionic field, together with N_v, is jointly controlled by the combination of GRIN lens segments and different types of wave plates.

Recently, a study [267] demonstrated the manipulation of Stokes skyrmions by employing tight focusing, which leverages the Gouy phase shift to enable transformations between different skyrmion types [shown in Fig. 34(c)]. In their study, an initial incident Néel-type skyrmion is first generated by superposing two orthogonally polarized beams with orthogonal spatial modes—LG modes $LG_{0,0}$ with left-handed circular polarization and $LG_{0,1}$ with right-handed circular polarization. Experiment was conducted using a vectorial optical field generator and a high numerical aperture objective lens to verify the topology transformation. As the skyrmion passes through an objective lens, it acquires a Gouy phase shift during the focusing process. This phase shift is determined by the orbital OAM carried by the high-order mode component of the incident skyrmion. Specifically, a $\frac{\pi}{2}$ phase shift for the $LG_{0,1}$ mode with right-handed circular polarization induces a 90° rotation in the Stokes vectors of the focused field, effectively transforming a Néel-type skyrmion into a Bloch-type skyrmion. Although the intensity distribution of the focused beam is diffraction-limited, the variation of the

Figure 34

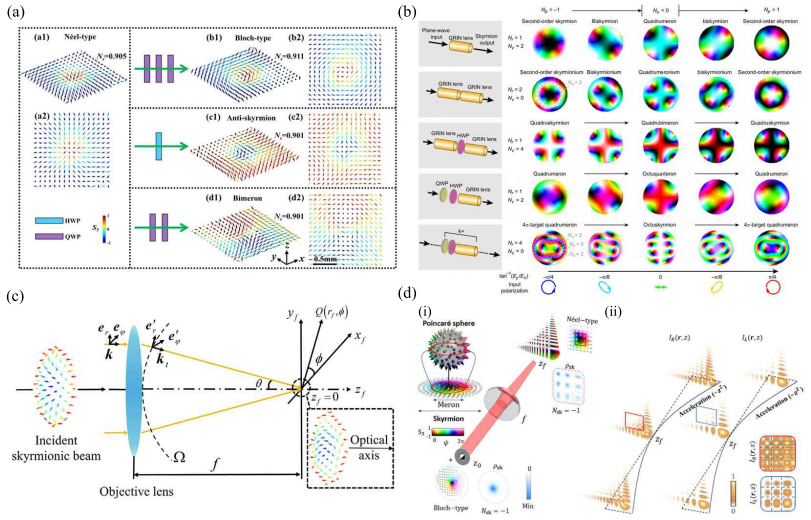

Manipulation of Stokes skyrmions. (a) The input Néel skyrmion is converted into different skyrmion types by adjusting the combination of various wave plates, such as HWPs and QWPs, to achieve helicity, polarity, and vorticity modifications while preserving topological protection. Reprinted from [16] under a Creative Commons license. (b) Manipulation of photonic quasiparticles using cascaded GRIN lenses. By adjusting the configuration of GRIN lenses, QWPs, and HWPs, diverse polarization vectorial light fields can be controlled, forming skyrmions, skyrmioniums, quadruskyrmions, and quadrumerons. The system enables precise control over polarity, radiality, and vorticity of topological photonic states. Reprinted with permission from Shen *et al.*, Phys. Rev. Appl. **21**, 024025 (2024), Ref. [312]. Copyright 2024 by the American Physical Society. (c) Experimental setup for manipulating skyrmionic beams under tight focusing. A high-NA objective lens focuses the incident skyrmionic beam, enabling topological transformation via the Gouy phase effect. Reprinted from [267] under a Creative Commons license. (d) Concept of manipulating optical skyrmions into accelerating skyrmion lattices using complex amplitude modulation holography. (i) Schematic of periodic skyrmion lattice generation via cubic phase modulation. (ii) Airy and vortex Airy-like beams exhibit periodic intensity lattices, complementary to each other, while accelerating along curved trajectories. Reprinted from [176] under a Creative Commons license.

Stokes vectors occurs on a sub-diffraction scale, with a full width at half maximum (FWHM) of approximately 0.67λ. The experimental results are evaluated by comparing the beam waist between theoretical calculations and experimental measurements. The estimated error was 4.27%, indicating excellent consistency.

Furthermore, a recent study experimentally realized the first accelerating optical skyrmion lattices in free space [176], as shown in Fig. 34(d). The key lies in using the complex amplitude modulation (CAM) hologram technique to simultaneously encode both phase and amplitude information onto an SLM. The generation scheme begins with a continuous-wave TEM_{00} laser that is split into two orthogonally polarized components. Each component is directed onto a separate region of an SLM, which encoded with distinct topological charges to generate two LG mode beams. The coherent superposition of these orthogonally polarized modes naturally gives rise to vector beams with skyrmion polarization textures, characterized by a full wrapping of the Stokes vector on the Poincaré sphere. To endow these skyrmion beams with self-accelerating behavior, a complex amplitude pattern, particularly incorporating a cubic phase component, is

also introduced on the corresponding region of the SLM with CAM. After Fourier transformation by a lens, the cubic phase is converted into the characteristic of an Airy beam. As a result, the output field directly manifests as an Airy beam carrying skyrmion lattices, a periodic array of skyrmion unit cells that self-accelerate along parabolic trajectories. Experimentally, the skyrmion lattices remain stable within a propagation range of ±1.22 Rayleigh lengths, whereas the inner meron lattices exhibit even greater robustness over ±3.06 Rayleigh lengths. This manipulation effectively couples the topological polarization textures of skyrmions with the unique propagation dynamics and spatial distributions of structured light beams, thereby providing a versatile platform for exploring non-trivial topological phenomena in free-space optics and offering richer possibilities of skyrmions for applications.

7. APPLICATION OF OPTICAL SKYRMIONS

Since the application of skyrmions is still at an early stage, only a limited number of studies explored their practical uses in the past few years. Consequently, previous reviews did not have many relevant articles on skyrmion applications to cover, focusing more on a broad, prospective outlook of potential applications [1,28–33]. Recently, however, an increasing number of publications have reported on skyrmion applications. In this section, we present some of these new developments, focusing on the direct applications of skyrmions themselves rather than on macroscopic structured light fields with topological properties. In addition, we provide a more detailed discussion of the application of skyrmions in the field of quantum information.

Due to the intrinsic characteristics of optical skyrmions, such as their ultrasmall and ultrafast properties, topological diversity, and topological stability, they hold immense potential for various applications, particularly in super-resolution imaging, metrology, and optical communication [22,23,314–319]. While these applications have not yet been fully realized, there are already some intermediate applications that lay the foundation for future advancements. In the following, we will provide a brief introduction to these applications.

7.1. Sensing and Metrology

Leveraging the inherent topological stability of skyrmions and their subwavelength features in local vector distributions [13] for sensing represents a promising application direction and lays the foundation for further advancements in metrology. Due to their topologically protected, nanoscale vectorial textures, skyrmion-based sensing and metrology enable detection with superior sensitivity and deep-subwavelength spatial resolution, as demonstrated by the high-resolution and high-precision detection of polar magnetization using optical spin meron lattices [320]. Earlier study has demonstrated the use of magnetic skyrmions for detection [21,321], specifically employing spoof plasmonic skyrmions supported by a space-coiling meta-structure to develop a high-performance microwave sensor for characterizing dielectric materials. This represents a milestone achievement in the development of ultra-compact and highly sensitive sensors.

Notably, the first application of optical skyrmions for nanoparticle displacement sensing was realized in recent years [22], as shown in Fig. 35(a). This is achieved by leveraging the precisely controlled spin texture of a spin skyrmion pair. In this research, a liquid-crystal phase modulator is used to generate a beam containing two circularly polarized components. These components excite a pair of SPP skyrmions (or evanescent optical vortices) with opposite topological charges on a silver surface. Under this configuration, the SAM texture exhibits a linear variation along the line connecting the skyrmions. This

Figure 35

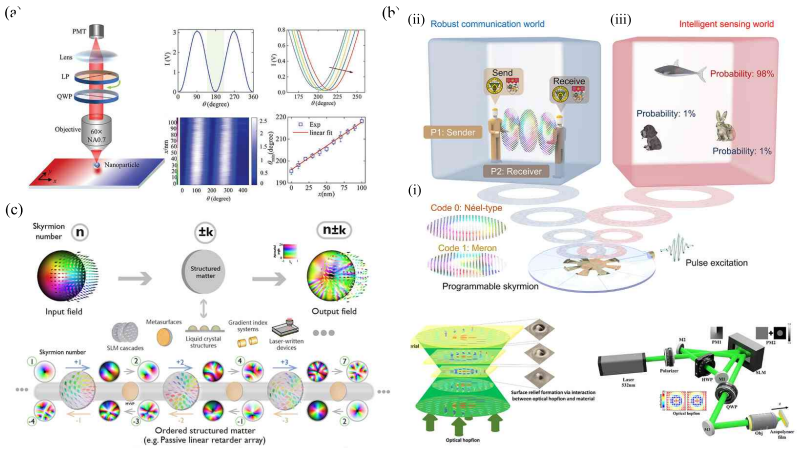

Applications of optical skyrmions in photonic information technologies. (a) Spin-manipulated photonic skyrmion-pair for displacement sensing. Experimental setup using a rotating linear polarizer to track polystyrene nanoparticle movement via intensity variations in a photomultiplier tube, demonstrating high-resolution optical sensing. Reprinted from [22] under a Creative Commons license. (b) Application of programmable plasmonic skyrmions for robust communication and intelligent sensing. (i) Programmable control of two skyrmion types achieved through the configuration of eight PIN diodes. (ii) Skyrmion-based optical communication for image transmission using binary encoding of two distinct skyrmion states. (iii) Intelligent sensing and recognition system based on Néel-type skyrmions. Reprinted with permission from Long Chen *et al.*, arXiv:2507.05944, Ref. [315]. (c) Optical skyrmion adders for photonic computing. Skyrmions of arbitrary order n passing through structured media perform addition or subtraction of skyrmion number, demonstrating both concept and robustness for photonic computing applications. Reprinted from [314] under a Creative Commons license. (d) Application of skyrmions for optical storage. Concept and experimental setup for encoding 3D polarization textures (optical hopfions) into a photosensitive azopolymer, with polarization states indicated by colors. Reprinted from [264] under a Creative Commons license.

linear region plays a crucial role in enabling displacement sensing, with a key parameter being the spacing between skyrmions. The study indicated that optimizing the spacing to $0.36\lambda_r$ (the wavelength of the evanescent optical vortices) makes the skyrmion pair highly effective for sensing applications. When a nanoparticle displaced within this region, it modifies the polarization state of the scattered light relative to the skyrmion pair. By analyzing this polarization change, precise displacement measurements can be achieved. Specifically, the elliptical polarization of the scattered light is analyzed using a QWP and a rotating polarizer. The measured light intensity reflects the polarization state, and the sensing precision is quantified by changes in the dip region (referred to as the "dip angle") of the detected intensity sinusoidal curve. The experiment shows a change of 0.22° nm^{-1} in dip-angle when moving the stage. Given the rotational stage's minimum increment of 0.00036°, a displacement resolution of 1.7 pm is achieved. The study further states that increasing the angular resolution of the rotation stage directly improves the displacement sensing resolution. This spin-based sensing method offers advantages over conventional techniques by circumventing interferometric setups and eliminating the need to measure weak signals near singularities, leading to a more robust and potentially more sensitive approach.

Recently, a work [315] demonstrates a programmable plasmonic skyrmion platform for intelligent sensing, as shown in Fig. 35(b). In the research, skyrmions are realized using a spoof localized surface plasmon (SLSP) platform with integrated PIN diodes for binary state control, leading to different topological textures. The system utilizes the skyrmions to interact with different objects, specifically twenty animal models. These models are placed in the skyrmion propagation path, and the interaction between the skyrmions and the models influences the electromagnetic response. A vector network analyzer precisely measures these EM-response data. The measured data reveal that different animal models exhibit distinct response characteristics at various frequency points within the test bandwidth, ensuring excellent classification performance. A convolutional neural network (CNN) is designed and trained on the collected experimental datasets. The trained CNN achieves a high accuracy rate of 98.33% during training. Further analysis showed that increasing the size of the EM-response data matrix enhances performance, and recognition accuracy is highest at the resonant frequency. By integrating these functionalities on the same platform, the work pioneers a new dimension of intelligent sensing through the unique topological properties of SLSP skyrmions.

Besides the aforementioned sensing applications, recent research has also demonstrated the use of skyrmions in metrology. Specifically, a study has achieved super-resolution 3D positioning of a receiver with a single emitting antenna, reaching centimeter-level localization accuracy by utilizing skyrmions embedded in non-separable toroidal pulses [24]. By leveraging the unique space-time non-separability and skyrmion topology of these toroidal pulses, each point in space can be associated with a distinct frequency-polarization signature. This distinctive property arises because the electromagnetic field of toroidal pulses exhibits a unique spatial and frequency distribution at each location, which is not separable into purely spatial or temporal components. As a result, the frequency and polarization states at each point provide a unique "fingerprint" for its position in 3D space. The receiver's 3D coordinates can be determined by comparing the measured spectral and polarization states with a pre-recorded database of these unique signatures, effectively eliminating the need for multi-antenna triangulation. This method not only simplifies the system architecture but also enables high-precision localization, even in complex environments like non-line-of-sight (NLOS) scenarios. In NLOS conditions, signals may reflect off obstacles or take indirect paths, making traditional positioning methods challenging, while the unique characteristics of the toroidal pulses allow for accurate positioning even in such complex environments.

7.2. Optical Information Technologies

In addition to their applications based on topological stability, skyrmions also exhibit remarkable topological diversity, which can be leveraged for various applications. Conventional optical information technologies, which rely on amplitude, phase, or polarization modulation, have enabled remarkable achievements in high-speed and high-capacity information processing and transmission. However, noise interference has always been a challenge. Optical skyrmions offer topologically structured, multi-degree-of-freedom carriers. Their quantized topological invariants make information resistant to noise and distortions, while their rich vectorial textures enable high-dimensional encoding, robust transmission, and reconfigurable photonic processing. In particular, by leveraging both their stability and topological versatility, skyrmions can act as robust carriers for information storage and transmission. At the same time, their topological diversity provides a foundation for novel computing approaches, potentially enabling secure and energy-efficient information processing.

For example, a novel high-density, long-range information transfer protocol has been proposed [312]. This protocol exploits the diverse topological properties of photonic

skyrmions, which are generated using cascaded GRIN lenses and wave plates. In this scenario, information is encoded into the topological numbers of various quasiparticles (characterized by polarity, vorticity, radiality, and centrality) using a shared secret key. The ciphertext light is then transmitted through free space. Due to the topological protection of the quasiparticles, it exhibits resistance to noise. Upon receiving the information, the receiver utilizes the known shared secret key to decode the message using Fourier lenses and Stokes polarimetry, reconstructing the originally transmitted information. This provides a feasible approach for utilizing skyrmions in communication applications.

Besides, the researchers [315] develop a wireless communication system based on binary amplitude shift keying (BASK) modulation, leveraging the programmable attributes of the SLSP skyrmions (shown in Fig. 35(b)). In this setup, the sender encodes information, such as an image, into a binary bitstream by switching the PIN diodes. This modulates the skyrmions between states representing code 0 (e.g., Néel-type skyrmion) and code 1 (e.g., meron). A transmitting antenna emits radio waves corresponding to these states. A receiving antenna, located 50 cm from the transmitter, captures the signal intensity, which is then processed for image reconstruction. Experimental results demonstrate successful transmission of both black-and-white and color images encoded in binary format. The topological protection inherent in skyrmions ensures the robustness of the transmitted signal, making it less susceptible to disturbance. To enhance communication speed, the advanced wireless communication system maintains a robust Néel-type skyrmion texture without actively switching the PIN diodes. This setup uses orthogonal frequency-division multiplexing techniques. A software-defined radio transceiver receives signals encoded by the skyrmions, with peak signal-to-noise ratios consistently ranging from 40 to 60 dB, and structural similarity index metric exceeding 99%, ensuring the quality and accuracy of the video or image transmission. Additionally, by introducing a time-periodic modulation to the programmable platform, the system generates harmonic skyrmions in the temporal dimension. Specifically, when the PIN diodes are driven by a square-wave signal with modulation frequency (f_s), the fundamental skyrmion mode at (f_0) gives rise to additional harmonic modes at ($f_0 \pm nf_s$, ($n = 1, 2, \ldots$)). These harmonic skyrmions effectively extend the available frequency channels beyond the single resonance. Leveraging this property, a frequency-division multiplexing communication scheme can be established, where different users are assigned to the fundamental and harmonic frequencies to simultaneously transmit and receive information. Only users tuned to these specific frequencies can achieve high-quality communication, while others cannot access the transmitted data. Owing to the topological protection of skyrmions, such multi-user communication remains robust against obstacles and interference, offering a promising route toward reliable wireless transmission in complex environments.

In addition to their potential in optical communication, skyrmions have recently been employed in photonic computing [314]. Before elaborating on the practical applications of skyrmions in photonic computing, it is worth noting that several works [95,286] have laid the foundation for employing skyrmions and other topologically structured optical fields in optical computing. One of these previous works [286] demonstrates the experimental realization of a tunable arbitrary retarder array using a cascade of low-functionality devices (such as SLMs and deformable mirrors). This system acts as a synthetic form of reconfigurable structured matter, enabling full dynamic control over (i) the axis geometry, which defines the ellipticity (e.g., linear, circular, or general elliptical) of the eigenpolarizations (fast/slow axes) of the retarder, (ii) the axis orientation, which specifies the angular orientation of the direction of the fast/slow axes, (iii) the retardance value, which represents the relative phase delay between the fast and slow axes, and (iv) the induced phase, which corresponds to the absolute phase shift encoded by the array

at each pixel (determined by their refractive index or geometry structure properties). With these four degrees of freedom, each virtual pixel can be reconfigured on demand, allowing the system to function as a beam generator, a beam analyzer, or a beam corrector.

Building on the previous modulation schemes, the recent application of skyrmions to photonic computing employs the skyrmion number to represent and manipulate data, analogous to how machine codes are used for operations in conventional computers [314], as shown in Fig. 35(c). The method employs specially designed structured matter—such as SLM cascades, metasurfaces, and gradient index systems—to act as adders and subtractors that modify the skyrmion number of an optical field. A key example is a spatially varying retarder with well-defined boundary conditions. In such devices, the change in skyrmion number between input and output is determined solely by the topological structure of the boundary, ensuring robustness against fabrication imperfections or inhomogeneities within the medium. To perform multi-stage operations, these functional modules can be cascaded sequentially. In practice, HWPs are often inserted between stages to restore the boundary polarization state, thereby aligning the output state of one module with the input requirement of the next. This enables the construction of complex photonic circuits using topologically protected skyrmion transformations. The study further introduces generalized skyrmion numbers, extending the standard concept from a single integer to a tuple $(n_1, n_2, \ldots, n_k)$. Each integer represents a connected component of the Poincaré sphere, carved out by the image of the boundary curve of the polarization field. This generalization increases information density, since it captures more details of the polarization field (Further details on the principles of generalized skyrmions can be found in the previous basic work [295]). Specifically, passive optical components (using a cascade of SLMs) convert a skyrmion of degree n into a generalized skyrmion $(n + k_1, n + k_2, \ldots)$ by manipulating the boundary conditions of the polarization field as it passes through the component. This process creates new connected components on the Poincaré sphere, where the values k_i are determined by how the boundary curve encircles each component. Experiments with gradient index systems and SLM cascades verified the concept. Disorder was deliberately introduced in SLM experiments, yet the skyrmion number remained stable. The main advantage of this approach is its enhanced robustness against perturbations. This robustness extends to perturbations in both the input field and the material parameters of the optical component itself, even at the boundary. This work demonstrates a promising framework for robust and high-density photonic computation.

Applying skyrmions to storage is also a promising direction [264,322]. The recent research [264] demonstrates the direct projection of 3D polarization textures of optical hopfions onto azopolymers to create surface relief structures, as shown in Fig. 35(d). This process "imprints" the complex polarization patterns of the hopfions onto the material's surface. The azopolymers, which are photosensitive polymers containing azobenzene, undergo light-induced mass transport when illuminated with visible light. This means that the material moves from brighter regions to darker regions in response to the polarization direction of the light beam. As a result, the surface of the azopolymer film is deformed, creating a relief structure that reflects the spatial intensity profile and, more importantly, the polarization texture of the optical hopfion. The polarization texture of the optical hopfion dictates the direction of mass transport within the azopolymer. Specifically, the azopolymers reorient themselves perpendicularly to the polarization of the irradiating light field. When carefully controlled, the polarization of the optical hopfion drives the azopolymer material to move, creating surface structures that resemble its 3D polarization textures. These structures effectively store the polar-

ization information of the hopfion on the surface of the azopolymer film with nanoscale precision. This method provides a novel way to encode and store information using the intricate 3D polarization properties of skyrmionic beams.

Notably, a recent study demonstrates real-time, reversible electrical control over optical skyrmions and hopfions in electro-optic crystals such as lithium niobate [323]. By applying an external voltage, the electro-optic effect induces a tunable phase mismatch that generates an effective pseudomagnetic field, enabling dynamic manipulation of topological parameters. Crucially, this electrical switching operates on millisecond timescales and exhibits quasi-nonvolatile behavior: once written, the topological state remains stable even after the voltage is removed, provided the system remains undisturbed. This capability enables electrically rewritable topological optical memory, which allows information to be written, erased, and reconfigured as distinct skyrmionic states. Meanwhile, because the encoded data are represented by quantized topological invariants, they inherit intrinsic robustness against noise and fabrication imperfections. This work opens a promising route toward high-density, low-power, and fault-tolerant photonic storage devices compatible with integrated optoelectronic circuits.

7.3. Quantum Information

Quantum information, with entanglement as a key resource in many protocols, provides intrinsic security for communication and storage, and has therefore attracted extensive research interest in recent years. However, entanglement is inherently fragile and can rapidly decay under the influence of decoherence and dephasing channels, which poses a major challenge to its practical implementation. An exciting avenue to address this limitation is the exploitation of topological protection, where non-trivial topological structures—often realized in topological matter or emergent quasiparticles [324,325]—are employed to preserve entanglement against local perturbations. In particular, skyrmions, with their rich topological textures and tunable degrees of freedom, provide a promising platform to encode, stabilize, and manipulate quantum information in a robust manner. Such capabilities may help alleviate several limitations, including sensitivity to environmental noise, restricted encoding dimensionality, stringent fabrication tolerances, and the challenge of maintaining coherence over extended distances or timescales, thereby opening potential new directions for secure communication and long-term storage.

A non-local, quantum-entangled skyrmion has been experimentally created and characterized, representing a new class of skyrmions distinct from conventional localized ones [23], as shown in Fig. 36(a). These skyrmions are uniquely encoded in the quantum correlations between two spatially separated entangled photons, while the individual photons themselves exhibit no inherent topological structure. The entangled state is described by:

$$|\Psi\rangle = \frac{1}{\sqrt{2}}\left(|\ell_1\rangle_A|H\rangle_B + e^{i\gamma}|\ell_2\rangle_A|V\rangle_B\right),$$

where ℓ_1 and ℓ_2 denote the OAM of the photons, H and V are polarization states, and γ is a phase factor controlling the texture of the skyrmion. In this study, quantum state tomography measurements were performed to characterize the experimentally prepared quantum state. For an example state with $\ell_1 = 1$, $\ell_2 = 0$, and $\gamma = 0$, the measured fidelity was found to be $F = 95.0\%$, demonstrating a close match between the experimentally generated state and the theoretically expected entangled state. To further verify the skyrmionic nature of the generated two-photon state, the Skyrme number was experimentally measured as $N_{exp} = 0.972$, which closely aligns with the theoretical prediction ($N_{th} = 1$). This agreement confirms the successful creation of a

Figure 36

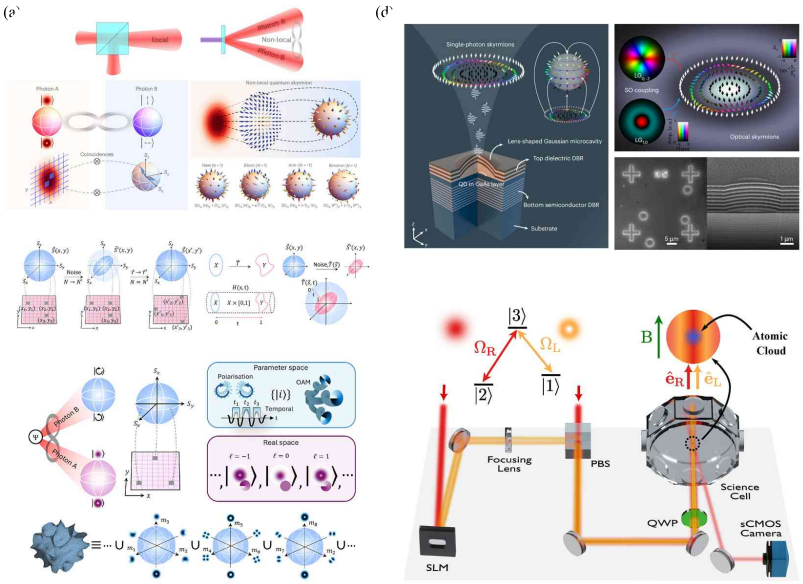

Applications of skyrmions in quantum information technologies. (a) Non-local quantum skyrmions. Entangled photons exhibit a skyrmionic topology, with photon A encoding OAM and photon B encoding polarization on respective Bloch spheres. Their entanglement enables non-local topological mapping, exhibiting the potential of quantum skyrmions as robust skyrmion carriers. Figure reproduced from [23], with permission from Springer Nature. (b) Topological protection of quantum skyrmions. The skyrmion wave function defines a map from the plane to the sphere. Although noise can distort this map, smooth deformations preserve the topology, ensuring robustness of quantum skyrmion states against perturbations. Reprinted from [316] under a Creative Commons license. (c) Topological spectrum in high-dimensional quantum states. (i) and (ii) Photonic quantum states are mapped from real space to parameter spaces using polarization, temporal modes, and OAM. (iii) High-dimensional manifolds can be deconstructed into collections of 2-spheres, giving rise to multiple topological mappings. Reprinted with permission from Robert de Mello Koch *et al.*, arXiv:2503.12540, Ref. [104]. (d) Single-photon skyrmions. A quantum dot–microcavity system generates single photons with skyrmionic polarization via spin–orbit coupling of degenerate modes. Figure reproduced from [317], with permission from Springer Nature. (e) Optical-to-atomic skyrmion mapping. Tailored LG and Gaussian beams transfer skyrmion topology to cold atoms in a Λ-system, enabling high-fidelity topological state storage. Reprinted from [318] under a Creative Commons license.

non-local, quantum-entangled skyrmion. The study further explored its controllability by dynamically tailoring the OAM difference ($\Delta\ell = \ell_2 - \ell_1$) and the phase γ. This enabled the generation of a diverse range of skyrmionic textures and topologies, including anti-skyrmions ($N < 0$), Néel-type ($N = 1, \gamma = 0$), Bloch-type ($N = 1, \gamma = \frac{\pi}{2}$), and higher-order skyrmions ($N > 1$). This versatility suggests their potential application as information carriers. In particular, the topological resilience of these skyrmions was demonstrated. The quantum Skyrme number remains robustly constant as the entanglement between the photons gradually decays. This topological protection persists until the entanglement vanishes entirely, highlighting a significant potential for topologically protected quantum information. What's more, subsequent work [27] delves more deeply into the noise robustness of the quantum skyrmions, with the findings opening a path to quantum information technologies.

Recently, a study [316] introduces a new entanglement observable based on skyrmion topologies and develops a framework to study its evolution within general quantum channels [shown in Fig. 36(b)]. The study provides a theoretical framework that explains why the skyrmion number is insensitive to local perturbations and remains invariant under smooth deformations. The article focuses on photons entangled in OAM and polarization space, demonstrating that noise affecting both photons can be simplified as a position-dependent perturbation acting only on the photon in the polarization state, thus confining the noise to a finite-dimensional Hilbert space. The framework predicts resilience against non-depolarizing and depolarizing noise through rigorous arguments and numerical simulations, respectively: for non-depolarizing channels such as retarders and diattenuators, the authors construct explicit homotopies showing that the noisy state can be smoothly deformed back to the original state, thereby proving invariance of the skyrmion number. In contrast, for depolarizing channels described by convex sums of Kraus operators, the invariance cannot be proven analytically, but numerical simulations with spatially varying and stochastic perturbations confirm that the skyrmion number remains robust, indicating that topology protects the entanglement observable even under realistic noisy conditions. Local noise sources that could destabilize the topology are also identified, but the authors suggest these can be ignored in many practical situations. This research provides a foundational understanding of how topology enhances the resilience of entanglement observables, with direct implications for distributing information via entanglement in noisy quantum computers and networks.

Another study unveils a novel approach to understanding and exploiting the intricate topological properties of high-dimensional quantum states [104], specifically using photonic quantum states in the OAM degree of freedom as a synthetic dimension [shown in Fig. 36(c)]. The central concept introduced is the "topological spectrum." Unlike traditional approaches that characterize quantum states with single topological numbers, it offers a more comprehensive description using a multitude of topological invariants. The authors develop a theoretical model leveraging Lie algebra structures to classify topological mappings across various dimensions. This model predicts topologies in high-dimensional manifolds, enabling a richer understanding of the underlying quantum states. The theoretical predictions are then rigorously tested and confirmed through experimental means, employing photonic quantum states with dimensionalities reaching up to 48 and topological spectra spanning over 17,000 mappings. The topological spectrum exhibits unique properties, enabling simultaneous robustness to perturbations and the ability to probe for them [324]. The study also explores and validates the existence of half-integer maps, arising from disk-to-disk mappings, and successfully extends them to sphere-to-sphere maps through a process of topological gluing. Additionally, the research investigates the emergence of topology, revealing that while the non-trivial elements of the topological spectrum remain invariant under state perturbations, emergent topological features arise in the trivial spaces of the spectrum, offering potential insights into complex channel dynamics.

In addition to the non-local skyrmion realized in quantum-entangled photon pairs, a different type of quantum optical skyrmion—the single-photon skyrmion—was reported very recently [317]. As mentioned before, the non-local skyrmion exhibits an emergent topological property encoded non-locally in the entanglement between two photons, with each individual photon carrying no skyrmionic texture on its own, whereas the single-photon skyrmion represents a local topological mode imprinted directly onto a single photon's polarization field. Specifically, this recent article presents the experimental realization of nanophotonic quantum skyrmions using a semiconductor cavity quantum electrodynamics system, as shown in Fig. 36(d). The researchers achieve this by manipulating the photonic spin–orbit coupling within a Gaussian microcavity.

This manipulation results in confined optical modes exhibiting skyrmionic topologies. A quantum dot is embedded in the microcavity, serving as a single-photon emitter deterministically coupled to the cavity mode. By tuning the quantum dot's emission wavelength to the cavity resonance, single-photon skyrmions are generated and detected. A key aspect of the work is the ability to control the polarity of the single-photon skyrmions by flipping the polarization of the quantum emitter through the Zeeman effect. The researchers tested the robustness of the generated quantum optical skyrmions by passing them through optical elements that introduced perturbations in intensity (attenuator), polarization (polarizing beam splitter), and phase (LC phase shifter). The skyrmion number remained largely unchanged, indicating topological protection. This work advances skyrmion–matter interactions into the single-photon regime, offering a promising route toward robust quantum technologies with high-dimensional qubits and large-capacity quantum memories.

Despite their potential for robust quantum information encoding, studies addressing the transfer and storage of quantum states structured with the topology of optical skyrmions into matter remain scarce.

Recently, the research demonstrates the high-fidelity transfer of topological skyrmion textures from structured light to matter [318], specifically a cold gas of strontium-87 (^{87}Sr) atoms [shown in Fig. 36(e)]. The skyrmions are created using a superposition of Gaussian and LG laser beams with orthogonal circular polarizations. The transfer of the skyrmion topology to matter is achieved using a technique analogous to electromagnetically induced transparency, involving adiabatic passage into a dark state within a Λ-scheme three-level atomic system. The resulting skyrmionic beam drives transitions between specific Zeeman ground states and an excited state in the Sr atoms. By carefully controlling the Rabi frequencies of these transitions, the topological texture of the optical skyrmion is imprinted onto the atomic pseudospin excitation. Here, the atomic pseudospin is represented by a two-component spinor characterized by the mixing angle (θ) and relative phase (ϕ). The θ represents the relative proportion of the two ground states $|1>$ and $|2>$ in the dark state, determining the radial direction of the pseudospin. The relative phase (ϕ) determines the phase relationship between the two states and governs the azimuthal direction of the pseudospin. To characterize the transfer of skyrmion topology to atoms, state-sensitive shadow imaging technique is employed to measure the spatial distribution of atomic populations in different quantum states. By measuring (θ) and ϕ across the atomic cloud, the pseudospin texture is reconstructed, yielding both the atomic pseudospin texture in the x–y plane and its compactified representation on a sphere, which enables quantitative evaluation of the skyrmion number. The resulting topological charge is preserved, with $Q \approx 0.84$ for the atomic skyrmion, slightly lower than the optical skyrmion's $Q \approx 0.91$, primarily due to the beam width exceeding the sample size. Nevertheless, this still effectively demonstrates a high-fidelity transfer of skyrmion topology from light to matter within the spatial overlap of the beam and atomic cloud. This work opens avenues for topological photonic state storage, advanced structured light analysis, and potential applications in data encoding and quantum information processing.

Besides, another recent work reports an on-chip entanglement-assisted transfer of quantum skyrmions [326]. In this scheme, the skyrmion topology is first encoded locally onto a single photon using integrated microring resonators, and then transferred to a non-local entangled state shared between two photons through a spin–momentum Bell-state measurement. Importantly, the skyrmion number remains robust against substantial environmental noise and even persists when entanglement fidelity is degraded, as long as quantum correlations are not entirely lost. This demonstrates a scalable and

noise-resilient route for topological information transfer in integrated quantum photonic systems, pointing toward robust quantum interconnects for distributed quantum technologies.

7.4. Other Applications

The applications of optical skyrmions are not limited to the areas discussed above. As research in this field accelerates, several novel and promising directions have emerged, highlighting the versatility and potential of skyrmion-based technologies.

One such direction is the use of skyrmions in polarization-sensitive imaging systems [327,328]. Recent studies propose leveraging the topological charge of skyrmionic beams to quantitatively analyze and correct diattenuation aberrations. This approach offers a new method for evaluating the performance of polarization adaptive optics techniques, providing a topologically grounded framework for enhancing image quality in complex optical systems.

Another promising area is particle trapping and sorting [179]. Recently, skyrmion-inspired Bloch surface wave lattices have been shown to generate tunable optical forces and topological potential wells for on-chip nanoparticle manipulation. Different lattice geometries (such as vortex, hexagonal, and honeycomb) offer distinct field and energy-flow topologies, leading to versatile functionalities. The vortex lattice enables stable trapping and even controlled rotation of particles, while the honeycomb lattice proves effective for size-dependent sorting by exploiting the sensitivity of optical forces to particle size and flow conditions. These capabilities point to compact and reconfigurable platforms for lab-on-chip applications.

In addition, nonlinear optical effects [162,329] have enabled innovative applications such as optical Hall devices and solitonic tractors. These advancements further expand the functional landscape of skyrmion-based systems, showing how their interaction with nonlinear media can lead to entirely new device concepts.

Overall, while practical implementations of optical skyrmions remain in the early stages, these unique topological structures offer a robust foundation for future technologies. Their inherent stability and versatility continue to inspire innovative applications across optics, quantum information, and beyond.

8. PERSPECTIVE AND CONCLUSION

Recent studies on optical skyrmions have unveiled their profound topological features in both fundamental physics and practical applications. As intricate topological structures with rich characteristics, their potential extends far beyond current explorations. Looking forward, several critical aspects warrant thorough investigation, from basic properties to novel effects and applications.

Although various physical mechanisms and types of optical skyrmions have been investigated, the field holds vast potential for further expansion. Studies could extend beyond traditional 2D real space, venturing into spatiotemporal domains, and momentum space to reveal unprecedented physical phenomena [25,37,163,234,245,247,330,331]. Understanding the stability and evolution of optical skyrmions during propagation remains crucial, particularly their resilience against perturbations in complex media [15,27,95]. Moreover, exploring related topological structures across multiple dimensions can reveal deeper topological nature and applications [38,104,120,127,148,171,264,332]. For instance, investigating optical knots within real turbulence environments [333] and higher-dimensional topological structures [104] may bring new insights and simultane-

ously enrich our understanding of optical skyrmions. Non-Abelian physics can also be introduced into optical skyrmions, realizing non-Abelian optical skyrmions through physical processes such as adiabatic processes [82].

On the path toward practical applications, several key challenges require resolution in generation, manipulation, and measurement. Compact and efficient methods for generating high-quality optical skyrmions remain to be explored. Novel approaches utilizing metasurfaces, PhCs, metamaterials, and other micro/nano photonic devices could enable more efficient and controllable skyrmion generation, facilitating widespread applications [19,25,334–337]. While rich topological configurations of optical skyrmions with different integer skyrmion numbers show promising applications, the generation of higher-order skyrmions needs further investigation [120,169]. Advanced manipulation techniques for skyrmionic configurations are significant for achieving precise dynamic control over skyrmion topological properties [16,228,312]. Additionally, as high-dimensional topological structures, efficient and complete measurement of their properties presents significant challenges, necessitating the development of high-sensitivity detection schemes and characterization methods [11,338,339].

The distinctive properties of optical skyrmions present promising opportunities for both fundamental effects and practical applications [340]. However, innovative approaches are still needed to transform scientific understanding into technological breakthroughs, unlocking the full potential of optical skyrmion technologies in information processing, quantum optics, sensing, metrology, light–matter interactions, etc. In information processing, optical skyrmions could serve as robust information carriers in next-generation platforms, enabling secure data transmission and processing in optical communications [18], data storage [341–343], and encoding [103,344,345]. The perturbation-resistant integer computing capabilities of optical skyrmions could advance optical computing significantly [314,346]. In quantum systems, optical skyrmions might facilitate the generation and manipulation of stable quantum-entangled states for quantum communications and computing [23,27,317,347]. Recent studies have also revealed promising applications in enhanced sensing and metrology [21,22,24]. Furthermore, the unique light-matter interactions of optical skyrmions suggest potential applications in nonlinear optical effects and novel coupling mechanisms [264,318,322,329]. Optical skyrmions also show promise in advanced manufacturing, particularly for high-precision material processing and fabrication [348–350]. The ability of optical skyrmions to overcome traditional diffraction limits could revolutionize super-resolution imaging techniques [11,13,19,351], opening new possibilities in biological imaging and microscopy.

To summarize, the study of optical skyrmions has emerged as a vibrant frontier in topological photonics, bridging abstract mathematical concepts with groundbreaking experimental realizations [1]. Rooted in the homotopy theory of spheres, these structured light fields derive their stability from mappings between physical parameter spaces and spatial or spatiotemporal manifolds [10]. The interplay of compactness [95], manifold flexibility, and dimensional reduction—particularly through Hopf fibrations—unifies diverse topological phenomena [108], from vortices and skyrmions to hopfions and knots, across electromagnetic [9], acoustic [86], and hydrodynamic systems [89]. This mathematical framework not only explains their robustness but also guides the engineering of novel topological states.

Historically, the conceptual journey of skyrmions traces back to foundational ideas in classical physics, evolving through quantum field theory into modern photonics. While Maxwell's vortex models and Kelvin's knotted ether laid early topological groundwork [5], contemporary advances in structured light and nanophotonics have enabled precise

creation and manipulation of optical skyrmions. Experimental breakthroughs—such as plasmonic skyrmion lattices [9,11], spin-textured vector beams [13,15], and spatiotemporal hopfions [148]—demonstrate how tailored interference of OAM states and metasurface-engineered phase profiles can sculpt light into topological configurations [19,95].

The propagation dynamics of optical skyrmions reveal intriguing dualities between stability and adaptability [15,25,236]. In free space, polarization skyrmions exhibit Gouy-phase-driven transformations between Néel and Bloch types while preserving their topological charge [15], whereas spatiotemporal skyrmions in toroidal pulses maintain non-separable space-time correlations [160,290]. Their quasi-non-diffracting nature [25,236], observed in Bessel-like configurations [217], enables robust transmission of topological information over extended distances. These properties, coupled with resilience to weak perturbations [23,27,95,277], position skyrmions as ideal candidates for applications demanding stable light-matter interactions [264,318,322].

FUNDING

National Key Research and Development Program of China (2023YFA1406900, 2022YFA1404800); National Natural Science Foundation of China (12234007, 12321161645, 12404427, 124B2084, 12221004, T2394480, T2394481); Science and Technology Commission of Shanghai Municipality (24YF2702400, 22142200400, 21DZ1101500, 2019SHZDZX01, 23DZ2260100, 24142200100); National Postdoctoral Program for Innovative Talents (BX20230079); China Postdoctoral Science Foundation (2023M740721).

ACKNOWLEDGMENT

We thank Dr. Bo Wang for helpful discussions.

DISCLOSURES

The authors declare no conflicts of interest.

DATA AVAILABILITY

Data underlying the results presented in this paper are not publicly available at this time but may be obtained from the authors upon reasonable request.

REFERENCES

1. Y. Shen, Q. Zhang, P. Shi, *et al.*, "Optical skyrmions and other topological quasiparticles of light," Nat. Photonics **18**, 15–25 (2024).
2. Y. Zhou, S. Li, X. Liang, *et al.*, "Topological spin textures: basic physics and devices," Adv. Mater. **37**, e2312935 (2025).
3. T. H. R. Skyrme, "A non-linear field theory," Proc. Royal Soc. London. Ser. A Math. Phys. Sci. **260**, 127–138 (1961).
4. T. H. R. Skyrme, "A unified field theory of mesons and baryons," Nuc. Phys. **31**, 556–569 (1962).
5. W. Thomson, "II. On vortex atoms," The London, Edinburgh, Dublin Philos. Mag. J. Sci. **34**, 15–24 (1867).

6. G. S. Adkins, C. R. Nappi, and E. Witten, "Static properties of nucleons in the skyrme model," Nucl. Phys. B **228**, 552–566 (1983).
7. C. Pappas, E. Lelievre-Berna, P. Falus, *et al.*, "Chiral paramagnetic skyrmion-like phase in MnSi," Phys. Rev. Lett. **102**, 197202 (2009).
8. A. M. Beckley, T. G. Brown, and M. A. Alonso, "Full Poincaré beams," Opt. Express **18**, 10777–10785 (2010).
9. S. Tsesses, E. Ostrovsky, K. Cohen, *et al.*, "Optical skyrmion lattice in evanescent electromagnetic fields," Science **361**, 993–996 (2018).
10. N. Manton and P. Sutcliffe, *Topological Solitons* (Cambridge University Press, 2004).
11. T. J. Davis, D. Janoschka, P. Dreher, *et al.*, "Ultrafast vector imaging of plasmonic skyrmion dynamics with deep subwavelength resolution," Science **368**, eaba6415 (2020).
12. Y. Shen, Y. Hou, N. Papasimakis, *et al.*, "Supertoroidal light pulses as electromagnetic skyrmions propagating in free space," Nat. Commun. **12**, 5891 (2021).
13. L. Du, A. Yang, A. Zayats, *et al.*, "Deep-subwavelength features of photonic skyrmions in a confined electromagnetic field with orbital angular momentum," Nat. Phys. **15**, 650–654 (2019).
14. X. Lei, A. Yang, P. Shi, *et al.*, "Photonic spin lattices: symmetry constraints for skyrmion and meron topologies," Phys. Rev. Lett. **127**, 237403 (2021).
15. S. Gao, F. C. Speirits, F. Castellucci, *et al.*, "Paraxial skyrmionic beams," Phys. Rev. A **102**, 053513 (2020).
16. H. Teng, J. Zhong, J. Chen, *et al.*, "Physical conversion and superposition of optical skyrmion topologies," Photonics Res. **11**, 2042–2053 (2023).
17. J. Ma, Z. Xie, and X. Yuan, "Tailoring arrays of optical Stokes skyrmions in tightly focused beams," Laser Photonics Rev. **19**, 2401113 (2025).
18. Z. Wan, H. Wang, Q. Liu, *et al.*, "Ultra-degree-of-freedom structured light for ultracapacity information carriers," ACS Photonics **10**, 2149–2164 (2023).
19. T. He, Y. Meng, L. Wang, *et al.*, "Optical skyrmions from metafibers with subwavelength features," Nat. Commun. **15**, 10141 (2024).
20. C. Bai, J. Chen, Y. Zhang, *et al.*, "Dynamic tailoring of an optical skyrmion lattice in surface plasmon polaritons," Opt. Express **28**, 33616–33618 (2020).
21. X. Li, L. Liu, Z. Zhou, *et al.*, "Highly sensitive and topologically robust multimode sensing on spoof plasmonic skyrmions," Adv. Opt. Mater. **10**, 2200331 (2022).
22. A. Yang, X. Lei, P. Shi, *et al.*, "Spin-manipulated photonic skyrmion-pair for pico-metric displacement sensing," Adv. Sci. **10**, 2205249 (2023).
23. P. Ornelas, I. Nape, R. de Mello Koch, *et al.*, "Non-local skyrmions as topologically resilient quantum entangled states of light," Nat. Photonics **18**, 258–266 (2024).
24. R. Wang, P.-Y. Bao, X. Feng, *et al.*, "Single-antenna super-resolution positioning with nonseparable toroidal pulses," Commun. Phys. **7**, 356 (2024).
25. C. Guo, M. Xiao, M. Orenstein, *et al.*, "Structured 3D linear space–time light bullets by nonlocal nanophotonics," Light. Sci. Appl. **10**, 160 (2021).
26. A. Zdagkas, C. McDonnell, J. Deng, *et al.*, "Observation of toroidal pulses of light," Nat. Photonics **16**, 523–528 (2022).
27. P. Ornelas, I. Nape, R. de Mello Koch, *et al.*, "Topological rejection of noise by quantum skyrmions," Nat. Commun. **16**, 2934 (2025).
28. Y. Shen, H. Wang, and S. Fan, "Free-space topological optical textures: tutorial," Adv. Opt. Photonics **17**, 295–374 (2025).
29. S. R. Allam, Y. Yoneda, and T. Omatsu, "Optical quasiparticles in paraxial laser beams," in *Progress in Optics* (Elsevier, 2025), pp. 281–338, Vol. **70**.

30. A. Yang, A. Kong, F. Meng, *et al.*, "Optical skyrmions: from fundamentals to applications," J. Opt. **27**, 043002 (2025).
31. J. Yang, J. Jiang, J. Wang, *et al.*, "Singular electromagnetics: from phase singularities to optical skyrmions and beyond," Adv. Phys. Res. **4**, 2400083 (2025).
32. W. Gao, Y. Zhou, X. Li, *et al.*, "Topological light field: from singular to skyrmionic optics and beyond," J. Opt. **27**, 083001 (2025).
33. X. Lei and Q. Zhan, "Topological quasiparticles of light: from spin–orbit coupling to photonic skyrmions," Laser Photonics Rev. e01427 (2025).
34. M. Lin, W. Zhang, C. Liu, *et al.*, "Photonic spin skyrmion with dynamic position control," ACS Photonics **8**, 2567–2572 (2021).
35. Z. L. Deng, T. Shi, A. Krasnok, *et al.*, "Observation of localized magnetic plasmon skyrmions," Nat. Commun. **13**, 8 (2022).
36. S. Wang, Z. Zhou, Z. Zheng, *et al.*, "Topological structures of energy flow: Poynting vector skyrmions," Phys. Rev. Lett. **133**, 073802 (2024).
37. L. Rao, J. Wang, X. Wang, *et al.*, "Meron spin textures in momentum space spawning from bound states in the continuum," Phys. Rev. Lett. **135**, 026203 (2025).
38. D. Sugic, R. Droop, E. Otte, *et al.*, "Particle-like topologies in light," Nat. Commun. **12**, 6785 (2021).
39. L. Shi, Z. Che, and Y. Kivshar, "Embarking on a skyrmion odyssey," Photon. Insights **3**, C02 (2024).
40. J. C. Maxwell, "On physical lines of force," Philos. Mag. **90**, 11–23 (2010).
41. I. J. Aitchison, "Tony Skyrme and the origins of skyrmions," arXiv (2019).
42. N. Nagaosa and Y. Tokura, "Topological properties and dynamics of magnetic skyrmions," Nat. Nanotechnol. **8**, 899–911 (2013).
43. A. N. Bogdanov and C. Panagopoulos, "Physical foundations and basic properties of magnetic skyrmions," Nat. Rev. Phys **2**, 492–498 (2020).
44. A. Belavin and A. Polyakov, "Metastable states of two-dimensional isotropic ferromagnets," JETP Lett. **22**, 245–248 (1975).
45. A. N. Bogdanov and D. Yablonskii, "Thermodynamically stable "vortices" in magnetically ordered crystals. The mixed state of magnets," Zh. Eksp. Teor. Fiz. **95**, 178 (1989).
46. U. K. Roessler, A. Bogdanov, and C. Pfleiderer, "Spontaneous skyrmion ground states in magnetic metals," Nature **442**, 797–801 (2006).
47. Z. Yang, Z. Wang, and H. Chen, "The Dzyaloshinskii-Moriya interaction in spin-Peierls systems," J. Phys. Condens. Matter. **14**, L199 (2002).
48. Y. Han, W-x Ji, P.-J. Wang, *et al.*, "Strain-tunable skyrmions in two-dimensional monolayer Janus magnets," Nanoscale **15**, 6830–6837 (2023).
49. K. K. Mishra, A. H. Lone, S. Srinivasan, *et al.*, "Magnetic skyrmion: from fundamental physics to pioneering applications," Appl. Phys. Rev. **12**, 011315 (2025).
50. Z. Wang, J. Ji, H. Yu, *et al.*, "Skyrmionic states induced by local Dzyaloshinskii-Moriya interaction," Phys. Rev. B **111**, 054417 (2025).
51. A. Fert, V. Cros, and J. Sampaio, "Skyrmions on the track," Nat. Nanotechnol. **8**, 152–156 (2013).
52. S. L. Sondhi, A. Karlhede, S. Kivelson, *et al.*, "Skyrmions and the crossover from the integer to fractional quantum hall effect at small Zeeman energies," Phys. Rev. B **47**, 16419–16426 (1993).
53. S. Muehlbauer, B. Binz, F. Jonietz, *et al.*, "Skyrmion lattice in a chiral magnet," Science **323**, 915–919 (2009).
54. X. Z. Yu, Y. Onose, N. Kanazawa, *et al.*, "Real-space observation of a two-dimensional skyrmion crystal," Nature **465**, 901–904 (2010).

55. C. Moreau-Luchaire, C. Moutafis, N. Reyren, *et al.*, "Additive interfacial chiral interaction in multilayers for stabilization of small individual skyrmions at room temperature," Nat. Nanotechnol. **11**, 444–448 (2016).
56. A. Neubauer, C. Pfleiderer, B. Binz, *et al.*, "Topological Hall effect in the *a* phase of MnSi," Phys. Rev. Lett. **102**, 186602 (2009).
57. F. Jonietz, S. Mühlbauer, C. Pfleiderer, *et al.*, "Spin transfer torques in MnSi at ultralow current densities," Science **330**, 1648–1651 (2010).
58. A. Fert, N. Reyren, and V. Cros, "Magnetic skyrmions: advances in physics and potential applications," Nat. Rev. Mater. **2**, 1–15 (2017).
59. C. Donnelly, S. Finizio, S. Gliga, *et al.*, "Time-resolved imaging of three-dimensional nanoscale magnetization dynamics," Nat. Nanotechnol. **15**, 356–360 (2020).
60. K. Everschor-Sitte, J. Masell, R. M. Reeve, *et al.*, "Perspective: magnetic skyrmions—overview of recent progress in an active research field," J. Appl. Phys. **124**, 240901 (2018).
61. M. Henderson, B. Heacock, M. Bleuel, *et al.*, "Three-dimensional neutron far-field tomography of a bulk skyrmion lattice," Nat. Phys. **19**, 1617–1623 (2023).
62. X. Yu, Y. Tokunaga, Y. Kaneko, *et al.*, "Biskyrmion states and their current-driven motion in a layered manganite," Nat. Commun. **5**, 3198 (2014).
63. D. Capic, D. A. Garanin, and E. M. Chudnovsky, "Stability of biskyrmions in centrosymmetric magnetic films," Phys. Rev. B **100**, 014432 (2019).
64. H. Wu, B. Miao, L. Sun, *et al.*, "Hybrid magnetic skyrmion," Phys. Rev. B **95**, 174416 (2017).
65. W. Liyanage, N. Tang, L. Quigley, *et al.*, "Three-dimensional structure of hybrid magnetic skyrmions determined by neutron scattering," Phys. Rev. B **107**, 184412 (2023).
66. H. B. Tran and Y. i Matsushita, "Skyrmions in van der Waals centrosymmetric materials with Dzyaloshinskii–Moriya interactions," Scripta Mater. **239**, 115799 (2024).
67. X. Li, X. Liu, J. Yang, *et al.*, "Creation and manipulation of magnetic skyrmions in 2D van der Waals magnets," Mater. Today Phys. **54**, 101727 (2025).
68. K. Huang, D.-F. Shao, and E. Y. Tsymbal, "Ferroelectric control of magnetic skyrmions in two-dimensional van der Waals heterostructures," Nano Lett. **22**, 3349–3355 (2022).
69. R. Juge, N. Sisodia, J. U. Larrañaga, *et al.*, "Skyrmions in synthetic antiferromagnets and their nucleation via electrical current and ultra-fast laser illumination," Nat. Commun. **13**, 4807 (2022).
70. R. Chen, Y. Gao, X. Zhang, *et al.*, "Realization of isolated and high-density skyrmions at room temperature in uncompensated synthetic antiferromagnets," Nano Lett. **20**, 3299–3305 (2020).
71. M. V. Correia, J. P. Velásquez, and C. C. de Souza Silva, "Stability and dynamics of synthetic antiferromagnetic skyrmions in asymmetric multilayers," Phys. Rev. B **110**, 094430 (2024).
72. S. Zhou, C. Wang, C. Zheng, *et al.*, "Manipulating skyrmions in synthetic antiferromagnetic nanowires by magnetic field gradients," J. Mag. Mag. Mater. **493**, 165740 (2020).
73. S. Zhou, C. Zheng, X. Chen, *et al.*, "Skyrmion-based spin-torque nano-oscillator in synthetic antiferromagnetic nanodisks," J. Appl. Phys. **128**, 033907 (2020).
74. K. Palotás, L. Rózsa, E. Simon, *et al.*, "Spin-polarized scanning tunneling microscopy characteristics of skyrmionic spin structures exhibiting various topologies," Phys. Rev. B **96**, 024410 (2017).

75. K. M. Song, J.-S. Jeong, B. Pan, *et al.*, "Skyrmion-based artificial synapses for neuromorphic computing," Nat. Electron. **3**, 148–155 (2020).
76. D. Pinna, F. Abreu Araujo, J.-V. Kim, *et al.*, "Skyrmion gas manipulation for probabilistic computing," Phys. Rev. Appl. **9**, 064018 (2018).
77. J-y Choi, W. J. Kwon, and Y-i Shin, "Observation of topologically stable 2D skyrmions in an antiferromagnetic spinor Bose-Einstein condensate," Phys. Rev. Lett. **108**, 035301 (2012).
78. K. Tiurev, T. Ollikainen, P. Kuopanportti, *et al.*, "Three-dimensional skyrmions in spin-2 Bose–Einstein condensates," New J. Phys. **20**, 055011 (2018).
79. Y. Kawaguchi, M. Kobayashi, M. Nitta, *et al.*, "Topological excitations in spinor Bose-Einstein condensates," Prog. Theor. Phys. Suppl. **186**, 455–462 (2010).
80. R. C. Coelho, H. Zhao, M. Tasinkevych, *et al.*, "Sculpting liquid crystal skyrmions with external flows," Phys. Rev. Res. **5**, 033210 (2023).
81. J.-S. B. Tai, A. J. Hess, J.-S. Wu, *et al.*, "Field-controlled dynamics of skyrmions and monopoles," Sci. Adv. **10**, eadj9373 (2024).
82. A. P. Reddy, N. Paul, A. Abouelkomsan, *et al.*, "Non-abelian fractionalization in topological minibands," Phys. Rev. Lett. **133**, 166503 (2024).
83. C. Psaroudaki and C. Panagopoulos, "Skyrmion qubits: a new class of quantum logic elements based on nanoscale magnetization," Phys. Rev. Lett. **127**, 067201 (2021).
84. T. Yokouchi, S. Sugimoto, B. Rana, *et al.*, "Pattern recognition with neuromorphic computing using magnetic field–induced dynamics of skyrmions," Sci. Adv. **8**, eabq5652 (2022).
85. D. A. Smirnova, F. Nori, and K. Y. Bliokh, "Water-wave vortices and skyrmions," Phys. Rev. Lett. **132**, 054003 (2024).
86. H. Ge, X.-Y. Xu, L. Liu, *et al.*, "Observation of acoustic skyrmions," Phys. Rev. Lett. **127**, 144502 (2021).
87. L. Cao, S. Wan, Y. Zeng, *et al.*, "Observation of phononic skyrmions based on hybrid spin of elastic waves," Sci. Adv. **9**, eadf3652 (2023).
88. A. Forbes, M. De Oliveira, and M. R. Dennis, "Structured light," Nat. Photonics **15**, 253–262 (2021).
89. B. Wang, Z. Che, C. Cheng, *et al.*, "Topological water-wave structures manipulating particles," Nature **638**, 394–400 (2025).
90. H. Xue, Y. Yang, and B. Zhang, "Topological acoustics," Nat. Rev. Mater. **7**, 974–990 (2022).
91. A. Hatcher, *Algebraic Topology* (Cambridge University Press, 2002).
92. L. Lu, J. D. Joannopoulos, and M. Soljačić, "Topological photonics," Nat. Photonics **8**, 821–829 (2014).
93. R. L. Bishop and R. J. Crittenden, *Geometry of Manifolds: Geometry of Manifolds* (Academic Press, 2011), Vol. **15**.
94. L. C. Kinsey, *Topology of Surfaces* (Springer Science & Business Media, 1997).
95. A. A. Wang, Z. Zhao, Y. Ma, *et al.*, "Topological protection of optical skyrmions through complex media," Light. Sci. Appl. **13**, 314 (2024).
96. P. J. Hilton, *An Introduction to Homotopy Theory* (Cambridge University Press, 1953).
97. G. L. Naber and G. L. Naber, *Topology, Geometry, and Gauge Fields* (Springer, 1997).
98. A. Altland and B. D. Simons, *Condensed Matter Field Theory* (Cambridge University Press, 2010).
99. M. Nakahara, *Geometry, Topology and Physics* (CRC Press, 2018).
100. H. Hopf, "Über die Abbildungen der dreidimensionalen Sphäre auf die Kugelfläche," Math. Ann. **104**, 637–665 (1931).

101. Y. Bouligand, B. Derrida, V. Poenaru, *et al.*, "Distortions with double topological character: the case of cholesterics," J. Phys. **39**, 863–867 (1978).
102. M. Monastyrsky, *Topology of Gauge Fields and Condensed Matter* (Springer Science & Business Media, 2013).
103. C. He, Y. Shen, and A. Forbes, "Towards higher-dimensional structured light," Light. Sci. Appl. **11**, 205 (2022).
104. R. de Mello Koch, P. Ornelas, N. Gounden, *et al.*, "The topological spectrum of high dimensional quantum states," Nature Commun. **16**, 11095 (2025).
105. D. Marco and M. A. Alonso, "4D topological textures in light," Phys. Rev. Lett. **134**, 123805 (2025).
106. B. Zhen, C. W. Hsu, L. Lu, *et al.*, "Topological nature of optical bound states in the continuum," Phys. Rev. Lett. **113**, 257401 (2014).
107. J. H. Han, *Skyrmions in Condensed Matter* (Springer, 2017), Vol. **278**.
108. Y. Liu, W. Hou, X. Han, *et al.*, "Three-dimensional dynamics of a magnetic hopfion driven by spin transfer torque," Phys. Rev. Lett. **124**, 127204 (2020).
109. J. Hietarinta and P. Salo, "Faddeev-Hopf knots: dynamics of linked un-knots," Phys. Lett. B **451**, 60–67 (1999).
110. R. A. Battye and P. M. Sutcliffe, "Solitons, links and knots," Proc. Roy. Soc. London Ser. A: Math. Phys. Eng. Sci. **455**, 4305–4331 (1999).
111. D. Rolfsen, *Knots and Links* (American Mathematical Soc., 2003).
112. W. T. Irvine and D. Bouwmeester, "Linked and knotted beams of light," Nat. Phys. **4**, 716–720 (2008).
113. P. Sutcliffe, "Skyrmion knots in frustrated magnets," Phys. Rev. Lett. **118**, 247203 (2017).
114. H. Larocque, D. Sugic, D. Mortimer, *et al.*, "Reconstructing the topology of optical polarization knots," Nat. Phys. **14**, 1079–1082 (2018).
115. X. Guo, P. Li, J. Zhong, *et al.*, "Tying polarization-switchable optical vortex knots and links via holographic all-dielectric metasurfaces," Laser Photonics Rev. **14**, 1900366 (2020).
116. S. Seki, M. Suzuki, M. Ishibashi, *et al.*, "Direct visualization of the three-dimensional shape of skyrmion strings in a noncentrosymmetric magnet," Nat. Mater. **21**, 181–187 (2022).
117. L. Bo, L. Ji, C. Hu, *et al.*, "Spin excitation spectrum of a magnetic hopfion," Appl. Phys. Lett. **119**, 212408 (2021).
118. J.-S. B. Tai and I. I. Smalyukh, "Three-dimensional crystals of adaptive knots," Science **365**, 1449–1453 (2019).
119. M. Birch, D. Cortés-Ortuño, L. Turnbull, *et al.*, "Real-space imaging of confined magnetic skyrmion tubes," Nat. Commun. **11**, 1726 (2020).
120. D. Ehrmanntraut, R. Droop, D. Sugic, *et al.*, "Optical second-order skyrmionic hopfion," Optica **10**, 725–731 (2023).
121. V. E. Korepin and L. D. Faddeev, "Quantization of solitons," Theor. Math. Phys. **25**, 1039–1049 (1975).
122. B. Van Waeyenberge, A. Puzic, H. Stoll, *et al.*, "Magnetic vortex core reversal by excitation with short bursts of an alternating field," Nature **444**, 461–464 (2006).
123. N. Kent, N. Reynolds, D. Raftrey, *et al.*, "Creation and observation of hopfions in magnetic multilayer systems," Nat. Commun. **12**, 1562 (2021).
124. H. Wu, N. Mata-Cervera, H. Wang, *et al.*, "Photonic torons with 3D topology transitions and tunable spin monopoles," Phys. Rev. Lett. **135**, 063802 (2025).
125. M. Mochizuki, "Spin-wave modes and their intense excitation effects in skyrmion crystals," Phys. Rev. Lett. **108**, 017601 (2012).
126. S. S. Cherepov, B. C. Koop, A. Y. Galkin, *et al.*, "Core-core dynamics in spin vortex pairs," Phys. Rev. Lett. **109**, 097204 (2012).

127. W. Lee, A. H. Gheorghe, K. Tiurev, *et al.*, "Synthetic electromagnetic knot in a three-dimensional skyrmion," Sci. Adv. **4**, eaao3820 (2018).
128. K. Shibata, X. Yu, T. Hara, *et al.*, "Towards control of the size and helicity of skyrmions in helimagnetic alloys by spin–orbit coupling," Nat. Nanotechnol. **8**, 723–728 (2013).
129. S. Banerjee, J. Rowland, O. Erten, *et al.*, "Enhanced stability of skyrmions in two-dimensional chiral magnets with Rashba spin–orbit coupling," Phys. Rev. X **4**, 031045 (2014).
130. S. Woo, K. M. Song, H.-S. Han, *et al.*, "Spin-orbit torque-driven skyrmion dynamics revealed by time-resolved X-ray microscopy," Nat. Commun. **8**, 15573 (2017).
131. I. I. Smalyukh, "Knots and other new topological effects in liquid crystals and colloids," Rep. Prog. Phys. **83**, 106601 (2020).
132. J.-S. Wu and I. I. Smalyukh, "Hopfions, heliknotons, skyrmions, torons and both abelian and nonabelian vortices in chiral liquid crystals," Liq. Cryst. Rev. **10**, 34–68 (2022).
133. H. Zhao, J.-S. B. Tai, J.-S. Wu, *et al.*, "Liquid crystal defect structures with Möbius strip topology," Nat. Phys. **19**, 451–459 (2023).
134. Y. Yuan and I. I. Smalyukh, "Chiral, topological, and knotted colloids in liquid crystals," Crystals **14**, 885 (2024).
135. J. Ruostekoski and J. Anglin, "Creating vortex rings and three-dimensional skyrmions in Bose-Einstein condensates," Phys. Rev. Lett. **86**, 3934–3937 (2001).
136. L. Leslie, A. Hansen, K. Wright, *et al.*, "Creation and detection of skyrmions in a Bose-Einstein condensate," Phys. Rev. Lett. **103**, 250401 (2009).
137. T. Kawakami, T. Mizushima, M. Nitta, *et al.*, "Stable skyrmions in SU (2) gauged Bose-Einstein condensates," Phys. Rev. Lett. **109**, 015301 (2012).
138. R. Bisset, W. Wang, C. Ticknor, *et al.*, "Robust vortex lines, vortex rings, and hopfions in three-dimensional Bose-Einstein condensates," Phys. Rev. A **92**, 063611 (2015).
139. V. Ardizzone, F. Riminucci, S. Zanotti, *et al.*, "Polariton Bose–Einstein condensate from a bound state in the continuum," Nature **605**, 447–452 (2022).
140. A. Gianfrate, H. Sigurðsson, V. Ardizzone, *et al.*, "Reconfigurable quantum fluid molecules of bound states in the continuum," Nat. Phys. **20**, 61–67 (2024).
141. H.-B. Luo, G. Li, F.-Q. Dou, *et al.*, "Solitons in Bose-Einstein condensates with attractive self-interaction on a Möbius strip," Phys. Rev. A **111**, 023325 (2025).
142. Y. Shen, X. Wang, Z. Xie, *et al.*, "Optical vortices 30 years on: OAM manipulation from topological charge to multiple singularities," Light. Sci. Appl. **8**, 90 (2019).
143. P. Coullet, L. Gil, and F. Rocca, "Optical vortices," Opt. Commun. **73**, 403–408 (1989).
144. S. Franke-Arnold, "30 Years of orbital angular momentum of light," Nat. Rev. Phys. **4**, 361 (2022).
145. A. Chong, C. Wan, J. Chen, *et al.*, "Generation of spatiotemporal optical vortices with controllable transverse orbital angular momentum," Nat. Photonics **14**, 350–354 (2020).
146. N. Jhajj, I. Larkin, E. W. Rosenthal, *et al.*, "Spatiotemporal optical vortices," Phys. Rev. X **6**, 031037 (2016).
147. S. W. Hancock, S. Zahedpour, A. Goffin, *et al.*, "Free-space propagation of spatiotemporal optical vortices," Optica **6**, 1547–1553 (2019).
148. C. Wan, Y. Shen, A. Chong, *et al.*, "Scalar optical hopfions," eLight **2**, 22 (2022).
149. M. R. Dennis, R. P. King, B. Jack, *et al.*, "Isolated optical vortex knots," Nat. Phys. **6**, 118–121 (2010).

150. C. W. Hsu, B. Zhen, A. D. Stone, *et al.*, "Bound states in the continuum," Nat. Rev. Mater. **1**, 1–13 (2016).
151. M. Kang, T. Liu, C. Chan, *et al.*, "Applications of bound states in the continuum in photonics," Nat. Rev. Phys. **5**, 659–678 (2023).
152. J. Wang, P. Li, X. Zhao, *et al.*, "Optical bound states in the continuum in periodic structures: mechanisms, effects, and applications," Photon. Insights **3**, R01 (2024).
153. C. Maurer, A. Jesacher, S. Fürhapter, *et al.*, "Tailoring of arbitrary optical vector beams," New J. Phys. **9**, 78 (2007).
154. Q. Zhan, "Cylindrical vector beams: from mathematical concepts to applications," Adv. Opt. Photonics **1**, 1–57 (2009).
155. D. Marinica, A. Borisov, and S. Shabanov, "Bound states in the continuum in photonics," Phys. Rev. Lett. **100**, 183902 (2008).
156. C. W. Hsu, B. Zhen, J. Lee, *et al.*, "Observation of trapped light within the radiation continuum," Nature **499**, 188–191 (2013).
157. B. Wang, W. Liu, M. Zhao, *et al.*, "Generating optical vortex beams by momentum-space polarization vortices centred at bound states in the continuum," Nat. Photonics **14**, 623–628 (2020).
158. C. Huang, C. Zhang, S. Xiao, *et al.*, "Ultrafast control of vortex microlasers," Science **367**, 1018–1021 (2020).
159. J. Wang, X. Wang, Z. Wu, *et al.*, "Inherent spin–orbit locking in topological lasing via bound state in the continuum," Phys. Rev. Lett. **134**, 133802 (2025).
160. I. Nape, K. Singh, A. Klug, *et al.*, "Revealing the invariance of vectorial structured light in complex media," Nat. Photonics **16**, 538–546 (2022).
161. H. Kedia, I. Bialynicki-Birula, D. Peralta-Salas, *et al.*, "Tying knots in light fields," Phys. Rev. Lett. **111**, 150404 (2013).
162. A. Karnieli, S. Tsesses, G. Bartal, *et al.*, "Emulating spin transport with nonlinear optics, from high-order skyrmions to the topological hall effect," Nat. Commun. **12**, 1092 (2021).
163. C. Guo, M. Xiao, Y. Guo, *et al.*, "Meron spin textures in momentum space," Phys. Rev. Lett. **124**, 106103 (2020).
164. C. Moutafis, S. Komineas, and J. Bland, "Dynamics and switching processes for magnetic bubbles in nanoelements," Phys. Rev. B **79**, 224429 (2009).
165. M.-Y. Im, P. Fischer, K. Yamada, *et al.*, "Symmetry breaking in the formation of magnetic vortex states in a permalloy nanodisk," Nat. Commun. **3**, 983 (2012).
166. S. Wintz, C. Bunce, A. Neudert, *et al.*, "Topology and origin of effective spin meron pairs in ferromagnetic multilayer elements," Phys. Rev. Lett. **110**, 177201 (2013).
167. M.-Y. Im, K.-S. Lee, A. Vogel, *et al.*, "Stochastic formation of magnetic vortex structures in asymmetric disks triggered by chaotic dynamics," Nat. Commun. **5**, 5620 (2014).
168. N. Gao, S.-G. Je, M.-Y. Im, *et al.*, "Creation and annihilation of topological meron pairs in in-plane magnetized films," Nat. Commun. **10**, 5603 (2019).
169. M. Król, H. Sigurdsson, K. Rechcińska, *et al.*, "Observation of second-order meron polarization textures in optical microcavities," Optica **8**, 255–261 (2021).
170. Y. Shen, "Topological bimeronic beams," Opt. Lett. **46**, 3737–3740 (2021).
171. Y. Shen, B. Yu, H. Wu, *et al.*, "Topological transformation and free-space transport of photonic hopfions," Adv. Photonics **5**, 015001 (2023).
172. J. Tang, Y. Wu, W. Wang, *et al.*, "Magnetic skyrmion bundles and their current-driven dynamics," Nat. Nanotechnol. **16**, 1086–1091 (2021).
173. R. Voinescu, J.-S. B. Tai, and I. I. Smalyukh, "Hopf solitons in helical and conical backgrounds of chiral magnetic solids," Phys. Rev. Lett. **125**, 057201 (2020).

174. J.-S. B. Tai, J.-S. Wu, and I. I. Smalyukh, "Geometric transformation and three-dimensional hopping of Hopf solitons," Nat. Commun. **13**, 2986 (2022).
175. V. M. Kuchkin, N. S. Kiselev, F. N. Rybakov, *et al.*, "Heliknoton in a film of cubic chiral magnet," Front. Phys. **11**, 1201018 (2023).
176. H. Wu, W. Zhou, Z. Zhu, *et al.*, "Optical skyrmion lattices accelerating in a free-space mode," APL Photonics **10**, 050804 (2025).
177. W. Lin, N. Mata-Cervera, Y. Ota, *et al.*, "Space-time optical hopfion crystals," Phys. Rev. Lett. **135**, 083801 (2025).
178. H. J. Putley, B. Davies, F. J. Rodríguez-Fortuño, *et al.*, "Mixing skyrmions and merons in topological quasicrystals of the evanescent optical field," Optica **12**, 614–619 (2025).
179. H. Xu, X. Xie, C. Zhang, *et al.*, "Topological magnetic lattices for on-chip nanoparticle trapping and sorting," Nano Lett. **25**, 10611–10618 (2025).
180. P. Shi, X. Gou, Q. Zhang, *et al.*, "Spintwistronics: photonic bilayer topological lattices tuning extreme spin–orbit interactions," arXiv (2024).
181. L. Zhang, L. Wan, W. Deng, *et al.*, "Observation of moiré plasmonic skyrmion clusters," Science Adv. **11**, eadx0478 (2024).
182. J. Schwab, A. Neuhaus, P. Dreher, *et al.*, "Skyrmion bags of light in plasmonic moiré superlattices," Nat. Phys. **21**, 988–994 (2025).
183. J. Schwab, F. Mangold, B. Frank, *et al.*, "Skyrmion bag robustness in plasmonic bilayer and trilayer Moiré superlattices," Nanophotonics **14**, 3955–3964 (2025).
184. Z. Liao, C. Huang, L. Liu, *et al.*, "Plasmonic skyrmions with bound states in the continuum," APL Photonics **8**, 096103 (2023).
185. J. L. Sun, S. C. Wang, Z. K. Zhou, *et al.*, "Generation of optical skyrmions formed by electromagnetic field vectors under 4π focal configurations," Opto-Electron. Eng. **50**, 230059 (2023).
186. K. Y. Bliokh, A. Y. Bekshaev, and F. Nori, "Dual electromagnetism: helicity, spin, momentum and angular momentum," New J. Phys. **15**, 033026 (2013).
187. K. Y. Bliokh, J. Dressel, and F. Nori, "Conservation of the spin and orbital angular momenta in electromagnetism," New J. Phys. **16**, 093037 (2014).
188. K. Y. Bliokh, A. Y. Bekshaev, and F. Nori, "Extraordinary momentum and spin in evanescent waves," Nat. Commun. **5**, 3300 (2014).
189. R. Gutiérrez-Cuevas and E. Pisanty, "Optical polarization skyrmionic fields in free space," J. Opt. **23**, 024004 (2021).
190. X. Lei, L. Du, X. Yuan, *et al.*, "Optical spin–orbit coupling in the presence of magnetization: photonic skyrmion interaction with magnetic domains," Nanophotonics **10**, 3667–3675 (2021).
191. Y. Dai, Z. Zhou, A. Ghosh, *et al.*, "Ultrafast microscopy of a twisted plasmonic spin skyrmion," Appl. Phys. Rev. **9**, 011420 (2022).
192. X. Tang, Y. Kuai, Z. Fan, *et al.*, "Achiral and chiral optical force within topological optical lattices generated with plasmonic metasurfaces and tunable incident beam," Phys. Rev. Appl. **19**, 054016 (2023).
193. L. Xiong, Y. Li, D. Halbertal, *et al.*, "Polaritonic vortices with a half-integer charge," Nano Lett. **21**, 9256–9261 (2021).
194. P. Shi, L. Du, and X. Yuan, "Spin photonics: from transverse spin to photonic skyrmions," Nanophotonics **10**, 3927–3943 (2021).
195. H. Wang, C. C. Wojcik, and S. Fan, "Topological spin defects of light," Optica **9**, 1417–1423 (2022).
196. P. Shi, L. Du, A. Yang, *et al.*, "Dynamical and topological properties of the spin angular momenta in general electromagnetic fields," Commun. Phys. **6**, 283 (2023).

197. X. Lei and Q. Zhan, "Topological charge constrained photonic skyrmion defects in split plasmonic vortices," ACS Photonics **10**, 3551–3557 (2023).
198. X. Lei, L. Du, X. Yuan, *et al.*, "Metastability of photonic spin meron lattices in the presence of perturbed spin–orbit coupling," Opt. Express **31**, 2225–2233 (2023).
199. X. Luo, Y. Cai, X. Yue, *et al.*, "Non-Hermitian control of confined optical skyrmions in microcavities formed by photonic spin–orbit coupling," Photonics Res. **11**, 610–621 (2023).
200. H. Lei, B. Luo, J. Hu, *et al.*, "Creation and manipulation of optical meron topologies in tightly focused electromagnetic field," J. Opt. **26**, 065001 (2024).
201. P. Chen, K. X. Lee, T. C. Meiler, *et al.*, "Topological momentum skyrmions in Mie scattering fields," Nanophotonics **14**, 2211–2217 (2025).
202. X. Lei, A. Yang, X. Chen, *et al.*, "Skyrmionic spin textures in nonparaxial light," Adv. Photonics **7**, 016009 (2025).
203. Y. Lang, Q. Xu, F. Huang, *et al.*, "Experimental observation of topological transition in optical multimeron," Adv. Mater., **38**, e07528 (2025).
204. S. Donati, L. Dominici, G. Dagvadorj, *et al.*, "Twist of generalized skyrmions and spin vortices in a polariton superfluid," Proc. Natl. Acad. Sci. **113**, 14926–14931 (2016).
205. W. Han, W. Cheng, and Q. Zhan, "Flattop focusing with full Poincaré beams under low numerical aperture illumination," Opt. Lett. **36**, 1605–1607 (2011).
206. C. Wei, D. Wu, C. Liang, *et al.*, "Experimental verification of significant reduction of turbulence-induced scintillation in a full Poincaré beam," Opt. Express **23**, 24331–24341 (2015).
207. G. Arora, Ruchi, and P. Senthilkumaran, "Full Poincaré beam with all the Stokes vortices," Opt. Lett. **44**, 5638–5641 (2019).
208. W. Lin, Y. Ota, Y. Arakawa, *et al.*, "Microcavity-based generation of full Poincaré beams with arbitrary skyrmion numbers," Phys. Rev. Res. **3**, 023055 (2021).
209. S. Kumar, R. K. Saripalli, A. Ghosh, *et al.*, "Controlling the coverage of full Poincaré beams through second-harmonic generation," Phys. Rev. Appl. **19**, 034082 (2023).
210. J. Morgan, P. Rebernik Ribič, F. Capotondi, *et al.*, "Poincaré beams from a free electron laser," Nat. Photon. **19**, 946–951 (2025).
211. S. Gao, F. C. Speirits, F. Castellucci, *et al.*, "Erratum: Paraxial skyrmionic beams [Phys. Rev. A 102, 053513 (2020)]," Phys. Rev. A **102**, 049901 (2020).
212. Z. Ye, S. Barnett, S. Franke-Arnold, *et al.*, "Theory of paraxial optical skyrmions," Proc. Roy. Soc. A **480**, 20240109 (2024).
213. S. M. Barnett, S. Franke-Arnold, and F. C. Speirits, "Stokes and skyrmion tensors with application to non-Cartesian coordinates," arXiv (2025).
214. J. Geng, S. R. Allam, Q. Sheng, *et al.*, "Generation of watt-level optical quasi-particles with a dual output coupling configuration in a diode-pumped Nd:YVO_4 laser," Opt. Express **33**, 52630–52638 (2025).
215. Y. Shen, E. C. Martínez, and C. Rosales-Guzmán, "Generation of optical skyrmions with tunable topological textures," ACS Photonics **9**, 296–303 (2022).
216. A. McWilliam, C. M. Cisowski, Z. Ye, *et al.*, "Topological approach of characterizing optical skyrmions and multi-skyrmions," Laser Photonics Rev. **17**, 2300155 (2023).
217. K. Singh, P. Ornelas, A. Dudley, *et al.*, "Synthetic spin dynamics with Bessel-Gaussian optical skyrmions," Opt. Express **31**, 15289–15300 (2023).
218. J. Berškys and S. Orlov, "Accelerating Airy beams with particle-like polarization topologies and free-space bimeronic lattices," Opt. Lett. **48**, 1168–1171 (2023).
219. T. Li, M. Liu, C. Chen, *et al.*, "Realization of spinful metaphotonic Stokes skyrmions," J. Opt. **26**, 09LT01 (2024).

220. D. Marco, I. Herrera, S. Brasselet, *et al.*, "Propagation-invariant optical meron lattices," ACS Photonics **11**, 2397–2405 (2024).
221. V. Hakobyan, Y. Shen, and E. Brasselet, "Unitary spin–orbit optical-skyrmionic wave plates," Phys. Rev. Appl. **22**, 054038 (2024).
222. W. R. Kerridge-Johns, A. S. Rao, and T. Omatsu, "Optical skyrmion laser using a wedged output coupler," Optica **11**, 769–775 (2024).
223. W. Lin, Y. Ota, Y. Arakawa, *et al.*, "On-chip optical skyrmionic beam generators," Optica **11**, 1588–1594 (2024).
224. W. Li, J. LaMountain, E. Simmons, *et al.*, "Vortex beam nanofocusing and optical skyrmion generation via hyperbolic metamaterials," Nanophotonics **14**, 4545–4553 (2025).
225. Y. Fu, R. Xie, N. Mata-Cervera, *et al.*, ''Free-form conformal metasurfaces robustly generating topological skyrmions," arXiv (2025).
226. X. Zeng, J. Fang, H. Wu, *et al.*, "Tailoring ultra-high-order optical skyrmions," Laser Photonics Rev. **19**, e00732 (2025).
227. V. Aita, A. Zaleska, H. J. Putley, *et al.*, "Polarization conversion and optical meron topologies in anisotropic epsilon-near-zero metamaterials," ACS Photonics **12**, 2909–2915 (2025).
228. V. Hakobyan and E. Brasselet, "Plates: from optical vortices to optical skyrmions," Phys. Rev. Lett. **134**, 083802 (2025).
229. Y. Yoneda, S. R. Allam, W. R. Kerridge-Johns, *et al.*, "Multi-color optical quasi-particle laser source formed of a Pr^{3+} doped fiber laser with a dual-output coupling geometry," Laser Photonics Rev. **19**, 2401403 (2025).
230. N. Mata-Cervera, Z. Xie, C. Li, *et al.*, "Tailoring propagation-invariant topology of optical skyrmions with dielectric metasurfaces," Nanophotonics **14**, 4069–4077 (2025).
231. P. Guo, Y. Gao, Z. Feng, *et al.*, "Ultrafast optical skyrmions generated via an achromatic Sagnac vortex generator," Opt. Lett. **50**, 6678–6681 (2025).
232. N. Mata-Cervera, D. K. Sharma, Y. Shen, *et al.*, "Skyrmionic polarization texture around the phase singularity of optical vortices," Phys. Rev. Lett. **135**, 033805 (2025).
233. H. Wang, C. Guo, and S. Fan, "Spatiotemporal steering of nondiffracting wave packets," Phys. Rev. Lett. **134**, 073803 (2025).
234. H. Teng, X. Liu, N. Zhang, *et al.*, "Construction of optical spatiotemporal skyrmions," Light. Sci. Appl. **14**, 324 (2025).
235. R. Wang, B. Ying, S. Shi, *et al.*, "Hybrid electromagnetic toroidal vortices," Sci. Adv. **11**, eads4797 (2025).
236. Y. Shen, N. Papasimakis, and N. I. Zheludev, "Nondiffracting supertoroidal pulses and optical 'Kármán vortex streets'," Nat. Commun. **15**, 4863 (2024).
237. W. Yu and Y. Shen, "Higher-order spatiotemporal wave packets with Gouy phase dynamics," Nanophotonics **14**, 4435–4446 (2025) .
238. I. B. Zel'Dovich, "Electromagnetic interaction with parity violation," Sov. Phys. JETP **6**, 1184–1186 (1958).
239. N. Papasimakis, V. A. Fedotov, V. Savinov, *et al.*, "Electromagnetic toroidal excitations in matter and free space," Nat. Mater. **15**, 263–271 (2016).
240. F. Meng, A. Yang, K. Du, *et al.*, "Measuring the magnetic topological spin structure of light using an anapole probe," Light. Sci. Appl. **11**, 287 (2022).
241. C. McDonnell, J. Deng, S. Sideris, *et al.*, "Functional THz emitters based on Pancharatnam-Berry phase nonlinear metasurfaces," Nat. Commun. **12**, 30 (2021).
242. R. Wang, P.-Y. Bao, Z.-Q. Hu, *et al.*, "Observation of resilient propagation and free-space skyrmions in toroidal electromagnetic pulses," Appl. Phys. Rev. **11**, 031411 (2024).

243. R. Wang, D.-T. Yang, T. Xin, *et al.*, "Optical atompilz: propagation-invariant strongly longitudinally polarized toroidal pulses," Appl. Phys. Lett. **125**, 111101 (2024).
244. R. Wang, S. Shi, Z. Zhang, *et al.*, "Observation of space-time nonseparable helical pulses," Nature Commun. **16**, 10927 (2025).
245. L. Niu, X. Feng, X. Zhang, *et al.*, "Electric-magnetic-switchable free-space skyrmions in toroidal light pulses via a nonlinear metasurface," arXiv (2025).
246. Y. Shen, N. Papasimakis, and N. I. Zheludev, "Simultaneous superoscillations in space and time in nonseparable light pulses," arXiv (2025).
247. S. Vo, R. Gutiérrez-Cuevas, and M. Alonso, "Closed forms for spatiotemporal optical vortices and sagittal skyrmionic pulses," J. Opt. **26**, 095607 (2024).
248. H. Fan, Q. Cao, X. Liu, *et al.*, "Perfect spatiotemporal optical vortices," Photonics Res. **13**, 1776–1782 (2025).
249. X. Liu, Q. Cao, and Q. Zhan, "Spatiotemporal optical wavepackets: from concepts to applications," Photon. Insights **3**, R08 (2024).
250. M. Lin, L. Du, and X. Yuan, "Photonic pseudospin skyrmion in momentum space," IEEE Photon. J. **15**, 1–6 (2023).
251. Y.-M. R. Hu, E. A. Ostrovskaya, A. Yakimenko, *et al.*, "Emergent momentum-space topological pseudospin defects in non-Hermitian systems," arXiv (2025).
252. W. Liu, B. Wang, Y. Zhang, *et al.*, "Circularly polarized states spawning from bound states in the continuum," Phys. Rev. Lett. **123**, 116104 (2019).
253. A. Chen, W. Liu, Y. Zhang, *et al.*, "Observing vortex polarization singularities at optical band degeneracies," Phys. Rev. B **99**, 180101 (2019).
254. X. Yin, J. Jin, M. Soljačić, *et al.*, "Observation of topologically enabled unidirectional guided resonances," Nature **580**, 467–471 (2020).
255. X. Zhao, J. Wang, X. Wang, *et al.*, "Emergence of momentum-space topological half vortices in an anisotropic cavity," Phys. Rev. Appl. **20**, 054059 (2023).
256. X. Zhao, J. Wang, W. Liu, *et al.*, "Spin-orbit-locking chiral bound states in the continuum," Phys. Rev. Lett. **133**, 036201 (2024).
257. P. Oliwa, P. Kapuściński, M. Popławska, *et al.*, "Electrically tunable momentum space polarization singularities in liquid crystal microcavities," Adv. Sci. **12**, 2500060 (2025).
258. Y. Zhang, M. Zhao, J. Wang, *et al.*, "Momentum-space imaging spectroscopy for the study of nanophotonic materials," Sci. Bull. (Beijing) **66**, 824–838 (2021).
259. M. Yessenov, A. H. Dorrah, C. Guo, *et al.*, "Ultrafast space-time optical merons in momentum-energy space," Nat. Commun. **16**, 8592 (2025).
260. M. Yessenov, J. Free, Z. Chen, *et al.*, "Space-time wave packets localized in all dimensions," Nat. Commun. **13**, 4573 (2022).
261. M. Yessenov, L. A. Hall, K. L. Schepler, *et al.*, "Space-time wave packets," Adv. Opt. Photon. **14**, 455–570 (2022).
262. H. Wang and S. Fan, "Photonic spin hopfions and monopole loops," Phys. Rev. Lett. **131**, 263801 (2023).
263. C. Li, S. Wang, and X. Li, "Spatiotemporal pulse weaving scalar optical hopfions," Light. Sci. Appl. **12**, 54 (2023).
264. R. Tamura, S. R. Allam, N. M. Litchinitser, *et al.*, "Three-dimensional projection of optical hopfion textures in a material," ACS Photonics **11**, 4958–4965 (2024).
265. A. Srinivasa Rao, "Optical skyrmions in the Bessel profile," J. Opt. Soc. Am. A **41**, 1059–1069 (2024).
266. X. Zhao, H. Liang, L. Ren, *et al.*, "Optical skyrmion and its 'zipper-like' topological behavior in an energy flux field," Opt. Lett. **49**, 5391–5394 (2024).

267. J. Chen, X. Shen, Q. Zhan, *et al.*, "Gouy phase induced optical skyrmion transformation in diffraction limited scale," Laser Photonics Rev. **19**, 2400327 (2025).
268. A. Hegde, K. Gupta, Y. Dai, *et al.*, "Geometry-driven lattice of photonic spin-meron tubes in free space," arXiv (2025).
269. R. W. Hellwarth and P. Nouchi, "Focused one-cycle electromagnetic pulses," Phys. Rev. E **54**, 889–895 (1996).
270. Y. Shen, A. Zdagkas, N. Papasimakis, *et al.*, "Measures of space-time nonseparability of electromagnetic pulses," Phys. Rev. Res. **3**, 013236 (2021).
271. J. Durnin, "Exact solutions for nondiffracting beams. I. The scalar theory," J. Opt. Soc. Am. A **4**, 651–654 (1987).
272. C. Liang, Z. Yuan, W. Yan, *et al.*, "Radially self-accelerating Stokes vortices in nondiffracting Bessel–Poincaré beams," Appl. Opt. **60**, 8659–8666 (2021).
273. H. Guo, T. Das, H. Wu, *et al.*, "Self-healing of optical skyrmionic beams," J. Opt. **27**, 025604 (2025).
274. N. Mata-Cervera, D. K. Sharma, R. Paniagua-Dominguez, *et al.*, "Observation of the non-diffraction of natural skyrmions with subwavelength confinement around optical vortices," arXiv (2025).
275. H. E. Kondakci and A. F. Abouraddy, "Diffraction-free space–time light sheets," Nat. Photonics **11**, 733–740 (2017).
276. J. Ye, Z. Che, J. Wang, *et al.*, "Propagation-invariant spatiotemporal vortices," Sci. Bull. (Beijing) **70**, 3758–3763 (2025).
277. C. Liu, S. Zhang, S. A. Maier, *et al.*, "Disorder-induced topological state transition in the optical skyrmion family," Phys. Rev. Lett. **129**, 267401 (2022).
278. Z. Zhang, X. Xie, C. Zhuang, *et al.*, "Topological protection degrees of optical skyrmions and their electrical control," Photonics Res. **13**, B1–B11 (2025).
279. C. Peters, K. Everts, T. Kleine, *et al.*, "Seeing through randomness with topological light," arXiv (2025).
280. C. Peters, V. Cocotos, and A. Forbes, "Structured light in atmospheric turbulence—a guide to its digital implementation: tutorial," Adv. Opt. Photonics **17**, 113–184 (2025).
281. H. Kuratsuji and S. Tsuchida, "Evolution of the Stokes parameters, polarization singularities, and optical skyrmion," Phys. Rev. A **103**, 023514 (2021).
282. L. Wang, S. Liu, G. Chen, *et al.*, "The robustness of skyrmion numbers of structured optical fields in atmospheric turbulence," Opt. Commun. **579**, 131568 (2025).
283. A. A. Wang, Y. Ma, Y. Cai, *et al.*, "Optical skyrmions in waveguides," arXiv (2025).
284. P. Yu, Q. Zhao, X. Hu, *et al.*, "Tailoring arbitrary polarization states of light through scattering media," Appl. Phys. Lett. **113**, 121102 (2018).
285. Z. Guo, C. Peters, N. Mata-Cervera, *et al.*, "Topological robustness of classical and quantum optical skyrmions in atmospheric turbulence," arXiv (2025).
286. C. He, B. Chen, Z. Song, *et al.*, "A reconfigurable arbitrary retarder array as complex structured matter," Nat. Commun. **16**, 4902 (2025).
287. E. Karimi and R. W. Boyd, "Classical entanglement?" Science **350**, 1172–1173 (2015).
288. A. Forbes, A. Aiello, and B. Ndagano, "Classically entangled light," in *Progress in Optics* (Elsevier, 2019), Vol. **64**, pp. 99–153.
289. D. Paneru, E. Cohen, R. Fickler, *et al.*, "Entanglement: quantum or classical?" Rep. Prog. Phys. **83**, 064001 (2020).
290. Y. Shen and C. Rosales-Guzmán, "Nonseparable states of light: from quantum to classical," Laser Photonics Rev. **16**, 2100533 (2022).

291. E. Medina-Segura, P. C. Obando, L. Mkhumbuza, *et al.*, "Emulating a quantum Maxwell's demon with non-separable structured light," Photonics Res. **13**, B79 (2024).
292. Y. Shen, I. Nape, X. Yang, *et al.*, "Creation and control of high-dimensional multi-partite classically entangled light," Light. Sci. Appl. **10**, 50 (2021).
293. A. Zdagkas, N. Papasimakis, V. Savinov, *et al.*, "Space-time nonseparable pulses: constructing isodiffracting donut pulses from plane waves and single-cycle pulses," Phys. Rev. A **102**, 063512 (2020).
294. K. Singh, I. Nape, W. T. Buono, *et al.*, "A robust basis for multi-bit optical communication with vectorial light," Laser Photonics Rev. **17**, 2200844 (2023).
295. A. A. Wang, Z. Zhao, Y. Ma, *et al.*, "Generalized skyrmions," arXiv (2024).
296. Q. Zhang, Z. Xie, P. Shi, *et al.*, "Optical topological lattices of Bloch-type skyrmion and meron topologies," Photonics Res. **10**, 947–957 (2022).
297. L. Wang, L. Ge, K. Gong, *et al.*, "Graphene plasmonic skyrmion lattices generated by radially polarized light beams," Phys. Rev. B **109**, 195434 (2024).
298. J. Chen, B. Ji, P. Lang, *et al.*, "Impact of the geometry of the excitation structure on optical skyrmion," Opt. Express **31**, 37929–37942 (2023).
299. N. Zhang, X. Lei, J. Liu, *et al.*, "Dynamic manipulation of graphene plasmonic skyrmions," Opt. Express **31**, 30020–30029 (2023).
300. Y. Zeng, Y. Yu, X. Shen, *et al.*, "Tightly focused optical skyrmions and merons formed by electric-field vectors with prescribed characteristics," Nanophotonics **13**, 251–261 (2024).
301. A. Ghosh, S. Yang, Y. Dai, *et al.*, "The spin texture topology of polygonal plasmon fields," ACS Photonics **10**, 13–23 (2023).
302. M. Lin, X. Gou, Z. Xie, *et al.*, "Photonic quasicrystal of spin angular momentum," Sci. Adv. **11**, eadv3938 (2025).
303. Z. Shen, S. Lu, and X. Xiong, "Optical generation and continuous transformation of plasmonic skyrmions," Opt. Express **32**, 48289–48301 (2024).
304. H. Wang, H. Teng, J. Zhong, *et al.*, "Topological decomposition and transformation of photonic quasicrystals," Nanophotonics **14**, 4301–4310 (2025).
305. Q. Zhang, Z. Xie, L. Du, *et al.*, "Bloch-type photonic skyrmions in optical chiral multilayers," Phys. Rev. Res. **3**, 023109 (2021).
306. X. Xie, J. Wu, P. Shi, *et al.*, "Optical skyrmions and tunable fine spin structures in deep-subwavelength scale at metal/graded index material interfaces," Opt. Express **32**, 44375–44385 (2024).
307. Y. C. Zhang, L. M. Zhao, and Y. S. Zhou, "Modulation of photonic skyrmions in a thin metal film structure," Opt. Express **32**, 3157–3166 (2024).
308. Q. Zhang, A. Yang, Z. Xie, *et al.*, "Periodic dynamics of optical skyrmion lattices driven by symmetry," Appl. Phys. Rev. **11**, 011409 (2024).
309. H. Zhang, C. Gao, and S. Fu, "Selective formation of generalized optical skyrmions," Opt. Lett. **50**, 2840–2843 (2025).
310. J. Wang, X. Zeng, K. Ren, *et al.*, "Generation of ring-shaped optical skyrmion with a high topological number," Appl. Phys. Lett. **126**, 201103 (2025).
311. H. Teng, J. Zhong, X. Lei, *et al.*, "Optical skyrmion interaction mediated polarization topology," Chin. Opt. Lett **23**, 100015 (2025).
312. Y. Shen, C. He, Z. Song, *et al.*, "Topologically controlled multiskyrmions in photonic gradient-index lenses," Phys. Rev. Appl. **21**, 024025 (2024).
313. G. Liu, L. Shi, Y. Liu, *et al.*, "Control of optical skyrmionic textures via the Pancharatnam-Berry phase," Phys. Rev. A **112**, 053507 (2025).
314. A. A. Wang, Y. Ma, Y. Zhang, *et al.*, "Perturbation-resilient integer arithmetic using optical skyrmions," Nat. Photon. **19**, 1367–1375 (2025).

315. L. Chen, Y. Shen, X. Y. Li, *et al.*, "Programmable skyrmions for robust communication and intelligent sensing," arXiv (2025).
316. R. de Mello Koch, B.-Q. Lu, P. Ornelas, *et al.*, "Quantum skyrmions in general quantum channels," APL Quantum **2**, 026126 (2025).
317. J. Ma, J. Yang, S. Liu, *et al.*, "Nanophotonic quantum skyrmions enabled by semiconductor cavity quantum electrodynamics," Nat. Phys. **21**, 1462–1468 (2025).
318. C. Mitra, C. S. Madasu, L. Gabardos, *et al.*, "Topological optical skyrmion transfer to matter," APL Photonics **10**, 046113 (2025).
319. S. Liu, X. Xie, P. Shi, *et al.*, "Optical spin angular momentum: properties, topologies, detection and applications," Nanomaterials **15**, 1798 (2025).
320. J. Wu, W. Wei, K. Guo, *et al.*, "Deep-subwavelength resolution detection of polar magnetization by optical spin meron lattices on hyperbolic metamaterials," Nanophotonics **14**, 4323–4331 (2025).
321. S. Wang, Y. Shen, and Y. Zheng, "Coplanar hybridization of half-mode magnetic plasmonic skyrmions: realization and application in a flexible wearable microwave sweat metasensor," IEEE Trans. Microw. Theory Techni. **23**, 9415 (2025).
322. R. Tamura, P. Kumar, A. S. Rao, *et al.*, "Direct imprint of optical skyrmions in azopolymers as photoinduced relief structures," APL Photonics **9**, 046104 (2024).
323. J. Jia, J. Ren, S. Zhou, *et al.*, "Electrically tuning photonic topological quasiparticles in synthetic two-level system," Nat. Phys **21**, 1885–1892 (2025).
324. Q. Yan, X. Hu, Y. Fu, *et al.*, "Quantum topological photonics," Adv. Opt. Mater. **9**, 2001739 (2021).
325. M. Koni, F. Nothlawala, V. Hakobyan, *et al.*, "Dual-wavelength quantum skyrmions from liquid crystal topological defect," Phys. Rev. Letters **135**, 223804 (2025).
326. H. Zhao, Y. Zhang, I. Nape, *et al.*, "On-chip photon entanglement-assisted topology loading and transfer," arXiv (2025).
327. Y. Ma, Z. Zhao, A. Wang, *et al.*, "Polarization adaptive optics for diattenuation aberration correction," in *Adaptive Optics: Methods, Analysis and Applications* (Optica Publishing Group, 2024), paper OTh4F.7.
328. Y. Ma, Z. Zhao, Y. Shen, *et al.*, "Using optical skyrmions to assess vectorial adaptive optics capabilities in the presence of complex aberrations," Sci. Adv. **11**, eadv7904 (2025).
329. G. Poy, A. J. Hess, A. J. Seracuse, *et al.*, "Interaction and co-assembly of optical and topological solitons," Nat. Photonics **16**, 454–461 (2022).
330. Y. Shen, Q. Zhan, L. G. Wright, *et al.*, "Roadmap on spatiotemporal light fields," J. Opt. **25**, 093001 (2023).
331. A. Forbes, "Structured light in space and time," Photon. Insights **4**, C02 (2025).
332. H. Wang and S. Fan, "Photonic Shankar skyrmion," Phys. Rev. Lett. **135**, 233803 (2025).
333. D. Pires, D. Tsvetkov, H. Barati Sedeh, *et al.*, "Stability of optical knots in atmospheric turbulence," Nat. Commun. **16**, 3001 (2025).
334. A. H. Dorrah and F. Capasso, "Tunable structured light with flat optics," Science **376**, eabi6860 (2022).
335. B. Yang, Q. Guo, D. Wang, *et al.*, "Scalar topological photonic nested metacrystals and skyrmion surface states in the light cone continuum," Nat. Mater. **22**, 1203–1209 (2023).
336. W. Zhao, X. Yi, J. Huang, *et al.*, "All-on-chip reconfigurable generation of scalar and vectorial orbital angular momentum beams," Light. Sci. Appl. **14**, 227 (2025).
337. J. Chen, A. Forbes, and C.-W. Qiu, "More than just a name? From magnetic to optical skyrmions and the topology of light," Light. Sci. Appl. **14**, 28 (2025).

338. N. A. Rubin, G. D'Aversa, P. Chevalier, *et al.*, "Matrix Fourier optics enables a compact full-Stokes polarization camera," Science **365**, eaax1839 (2019).
339. S. Qi, S. Liu, L. Han, *et al.*, "Dynamically measuring the holo-information of light fields in three-dimensional space using a periodic polarization-structured light," Sci. China Phys. Mech. Astron. **64**, 264211 (2021).
340. T. Xia, J. Ma, Z. Xie, *et al.*, "Symmetric and asymmetric Hall effect-like splitting of optical Stokes skyrmions via a hybrid multi-zone filter," Photonics Res. **13**, 1365–1374 (2025).
341. X. Li, T.-H. Lan, C.-H. Tien, *et al.*, "Three-dimensional orientation-unlimited polarization encryption by a single optically configured vectorial beam," Nat. Commun. **3**, 998 (2012).
342. M. Gu, X. Li, and Y. Cao, "Optical storage arrays: a perspective for future big data storage," Light. Sci. Appl. **3**, e177 (2014).
343. Y. Chen, X. Yang, and J. Gao, "3D Janus plasmonic helical nanoapertures for polarization-encrypted data storage," Light. Sci. Appl. **8**, 45 (2019).
344. J. Du and J. Wang, "High-dimensional structured light coding/decoding for free-space optical communications free of obstructions," Opt. Lett. **40**, 4827–4830 (2015).
345. Y. Zhang, A. A. Wang, Z. Zhao, *et al.*, "Skyrmions based on optical anisotropy for topological encoding," arXiv (2025).
346. Z. Zhang, L. Kong, L. Zhang, *et al.*, "Structured light meets machine intelligence," eLight **5**, 26 (2025).
347. I. Nape, B. Sephton, P. Ornelas, *et al.*, "Quantum structured light in high dimensions," APL Photonics **8**, 051101 (2023).
348. C. Hnatovsky, V. Shvedov, W. Krolikowski, *et al.*, "Revealing local field structure of focused ultrashort pulses," Phys. Rev. Lett. **106**, 123901 (2011).
349. J. Ni, Q. Wei, Y. Zhang, *et al.*, "Super-resolution three-dimensional structured illumination profilometry for in situ measurement of femtosecond laser ablation morphology," APL Photonics **8**, 101302 (2023).
350. V. V. Belloni, M. Hassan, L. Furfaro, *et al.*, "Single shot generation of high-aspect-ratio nano-rods from sapphire by ultrafast first order Bessel beam," Laser Photonics Rev. **18**, 2300687 (2024).
351. B.-C. Chen, W. R. Legant, K. Wang, *et al.*, "Lattice light-sheet microscopy: imaging molecules to embryos at high spatiotemporal resolution," Science **346**, 1257998 (2014).

Cheng Cheng received his B.S. degree in applied physics from Tongji University, Shanghai, China, in 2023. Since 2023, he has been working toward his Ph.D. degree in physics at Fudan University under the supervision of Prof. Lei Shi. His research interests include optical skyrmions and hopfions, the novel topological structure in wave systems, manipulation of surface water waves, and dispersion relationships and bound states in the continuum in periodic structure.

Lixi Rao is a Ph.D. student in the Department of Physics, Fudan University, Shanghai, under the supervision of Prof. Lei Shi. He received his B.S. degree in physics from Fudan University in 2024. His current research interests are focused on the novel topological textures in optics, structured light, photonic crystals, and their applications in light–matter interactions.

Junyi Ye received his B.S. degree in optoelectronic information science and engineering from Zhejiang University of Technology, Hangzhou, China, in 2022. Since 2022, he has been working toward his Ph.D. degree in physics at Fudan University, Shanghai, China, under the supervision of Prof. Lei Shi. His research interests include optical metrology and wavefield manipulation of liquid surface waves.

Xingqi Zhao received his B.S. degree in physics from Fudan University, Shanghai, China, in 2022. Since 2022, he has been working toward his Ph.D. degree in condensed matter physics at Fudan University under the supervision of Prof. Lei Shi. His research interests include bound states in the continuum, photonic crystals, and topological photonics.

Zhiyuan Che is an assistant professor at the Institute of Acoustics, Tongji University, China. He received his Ph.D. degree in physics from the Department of Physics at Fudan University, China, in 2022. He conducted graduate studies in Optics at East China Normal University (2018) and earned his B.S. degree in physics from Lingnan Normal University, China, in 2015.

Wenzhe Liu is an assistant professor at the Institute for Nanoelectronic devices and Quantum Computing, Fudan University. He was previously a research assistant professor in the Department of Physics, the Hong Kong University of Science and Technology. He received his Ph.D. degree in physics from Fudan University in 2020 and his B.S. degree in physics from Fudan University in 2015. His research interests include light scattering in photonic crystals, bound states in the continuum, nanophotonics, and classical-wave metamaterials.

Jiajun Wang is an assistant professor at the State Key Laboratory of Surface Physics, Fudan University. He was previously a postdoctoral fellow at Fudan University, awarded the fellowship of China National Postdoctoral Program for Innovative Talents. He received his B.S. degree (2019) and Ph.D. degree (2023) in physics from Fudan University. His research interests include photonic crystals, bound states in the continuum, metamaterials, structured light, light-matter interactions, micro/nano lasers, applications of AI in optics and topological photonics.

Lei Shi is a professor at the Department of Physics, Fudan University. He received his B.S. degree in physics from Nanjing University in 2005 and his Ph.D. degree in Condensed Matter Physics from Fudan University in 2010. He conducted postdoctoral research at the Institute of Materials Science in Madrid, Spain, and subsequently at Aalto University in Finland. His notable awards include the Golden Bridge Award for Outstanding Individual Contribution from the China Technology Market Association, the 2022 China Industry-University-Research Collaboration Innovation and Promotion Award (Individual), and the 2023 Shanghai Natural Science Award (First Class) as the second contributor. His research focuses on photonic crystals, light-field manipulations, and advanced optical measurement techniques. He has authored or co-authored over 80 papers as first or corresponding author in prestigious journals such as *Nature, Nature Photonics, Nature Communications, Physical Review Letters, PNAS, Advanced Materials, Light: Science & Applications, Science Bulletin, ACS Nano*, and *Nano Letters* and holds nine authorized invention patents. In undergraduate education, he has taught courses including College Physics, Optics, and Classical Electrodynamics.